The dissertation committee for Ravishankar Ajjanagadde Shivarama
Certifies that this is the approved version of the following dissertation:

Hamilton's equations with Euler parameters for hybrid particle-finite element simulation of hypervelocity impact

Committee:

Eric P. Fahrenthold, Supervisor

Anthony Bedford

Richard H. Crawford

Raul G. Longoria

Alfred E. Traver

Hamilton's equations with Euler parameters for hybrid particle-finite element simulation of hypervelocity impact

by

Ravishankar Ajjanagadde Shivarama, B.E, M.Sc (Engg)

Dissertation

Presented to the Faculty of the Graduate School of

The University of Texas at Austin

in Partial Fulfillment

of the Requirements

for the Degree of

DOCTOR OF PHILOSOPHY

The University of Texas at Austin

August 2002

ProQuest Information and Learning Company
300 North Zeeb Road
PO Box 1346
Ann Arbor, MI 48106-1346

To my parents

Acknowledgments

At the outset I would like to thank my advisor, Dr. Eric P. Fahrenthold. I consider myself fortunate to work with him. He has been very encouraging throughout this work. Thank you. I would like to thank Dr. Raul Longoria, firstly for serving on my committee and secondly for providing me an opportunity to be a teaching assistant for ME 244L. I had the privilege of being a teaching assistant for six semesters including Fall 1997, Fall 1998, Spring 1999, Fall 1999 and Spring 2000 and Spring 2002. I have truly enjoyed it. I would also like to thank Dr. Anthony Bedford, Dr. Richard Crawford and Dr. Alfred Traver for serving as my advisory committee members.

My parents, my brother and sister have always stood by me and its beyond words to quantify their love and support. Thanks to the almighty God for he has always provided me with the inner strength to overcome in what appeared to be an insurmountable task. I would like to thank my old buddy, my name sake friend Ravishankar Mahadevappa who has painstakingly listened to all my frustrations and constant cribbing. I also thank my Korean friends Kwan-Woong Gwak, Young-Hoon Han, Donghyun Kim and Young-Keun Park for providing me good company. Thanks to Horacio and Marc Compere for all the interesting discussions and to Cengiz Vural, the computer geek for being there to answer my silly questions. I would also like to thank all my current and former roommates too many to list here, for making me feel at home away from home.

Finally, I would like to thank NASA Johnson Space Center (NAG 9-1244), National Science Foundation (CMS 9912475), the Texas Advanced Technology Program (project number 003658-0709-1999) for the research support and NASA Ames Research Center and Texas Advanced Computing Center for their computer time.

Ravishankar Ajjanagadde Shivarama

The University of Texas at Austin
August 2002

Hamilton's equations with Euler parameters for hybrid particle-finite element simulation of hypervelocity impact

Publication No. ____________________

Ravishankar Ajjanagadde Shivarama, Ph.D.
The University of Texas at Austin, 2002

Supervisor: Eric P. Fahrenthold

Hypervelocity impact studies (impact velocities > 1 km/sec) encompass a wide range of applications including development of anti-terrorist defense and orbital debris shield for the International Space Station (ISS). The focus of this work is on the development of a hybrid particle-finite element method for orbital debris shield simulations. The problem is characterized by finite strain kinematics, strong energy domain coupling, contact-impact, shock wave propagation and history dependent material damage effects. A novel hybrid particle finite element method based on Hamilton's equations is presented. The model discretizes the continuum of interest simultaneously (but not redundantly) into particles and finite elements. The particles are ellipsoidal in shape and can translate and rotate in three dimensional space. Rotation is described using Euler parameters. Volumetric and contact impact effects are modeled using particles, while strength is modeled using conventional Lagrangian finite elements. The model is general enough to accommodate a wide range of material models and equations of state.

Contents

List of Tables

List of Figures

Chapter 1

Introduction

1.1 Introduction

Impact phenomena is common to many situations in engineering, like in collision of vehicles intentionally or unintentionally, impact of a printer head against paper as in dot matrix printers, the impact of a dropped weight on a work piece as in forging operation, impact of a bullet against a target or impact of a meteorite on a satellite. Although these are joined together under the broad umbrella of impact dynamics, it is not difficult to see that the impact of a meteorite on a space craft for example is not the same as the impact of a printer head against the paper, the primary distinguishing factor between the two being the velocity of impact. Materials behave differently at different velocities of impact. The effects of inertia, wave propagation and phase transformation become increasingly important as the impact velocity increases.

There is no general agreement on what constitutes a hypervelocity impact, although majority of the researchers in this area would consider impact velocities in the range of 5-15km/sec as hypervelocity impact. Studies in hypervelocity impact encompass a multitude of applications including the study of meteorite impacts on earth, development of anti-terrorist defence and orbital debris shielding of space structures, the last one being the focus of this dissertation.

The advancement in computational science over the last several decades has established simulation based approach as a powerful tool for analysis along with analytical and experimental techniques. Hypervelocity impact studies have not been immune to this development. In addition, the following factors have provided added encouragement to look at simulation based approach as a viable tool of analysis:

- The solid materials involved in hypervelocity impact undergo elastic plastic deformation in a multi-energy framework. Finite strain kinematics, large temperature and stress gradients in the materials almost completely rule out the use of only analytical techniques as a modeling tool.
- The limitations of existing light gas guns (LGG) to shoot projectiles at kinetic energies in the entire range of interest has provided ample motivation for shield design studies based on simulation.
- Simulation based approach can provide low cost and faster turn around time.

1.2 The problem

The dawn of space age has seen several countries launch space structures into orbit. However the life of these structures are finite and once found non-functional they are abandoned. These objects disintegrate over time into smaller mass fragments, collectively addressed today by the term "orbital debris". This chunk of matter travel at extremely high velocities, posing a serious risk to orbiting space structures such as the International Space Station (ISS) and astronauts on them. The gravity of this problem has been studied in detail. The reader is referred to [56] [38] [63] and the references there in.

1.3 Solution

F.L. Whipple [73], first mooted the idea of placing a thin sacrificial sheet of metal ahead of the wall of an orbiting space structure. This geometrical arrangement, excites the incoming debris to higher thermal energy states, causing a partial/complete vaporization of the debris, resulting in less damage to the wall of the space structure. A single bumper shield is also referred to as a "Whipple shield" for obvious reasons in the literature. The concept was extended to multi-shock shields [13] where a series of thin bumpers convert the kinetic energy of the in-coming debris into thermal energy sufficient enough to cause melting and vaporization for a large range of velocities. This results in low weight and better protection of space structures. A typical debris shield configuration is shown in figure (1.1).

1.4 Sequence of events

An orbital debris impact can be visualized as a three phase event. In the first phase the debris impacts onto a shield resulting in one or more of the following, depending on the materials and other parameters involved in impact.

- Perforation of the shield
- Fragmentation of the debris
- Complete or partial vaporization of the debris

In the second phase, the solid-liquid cloud of debris expands radially before it impacts the second shield or the wall plate as the case may be, which forms the third

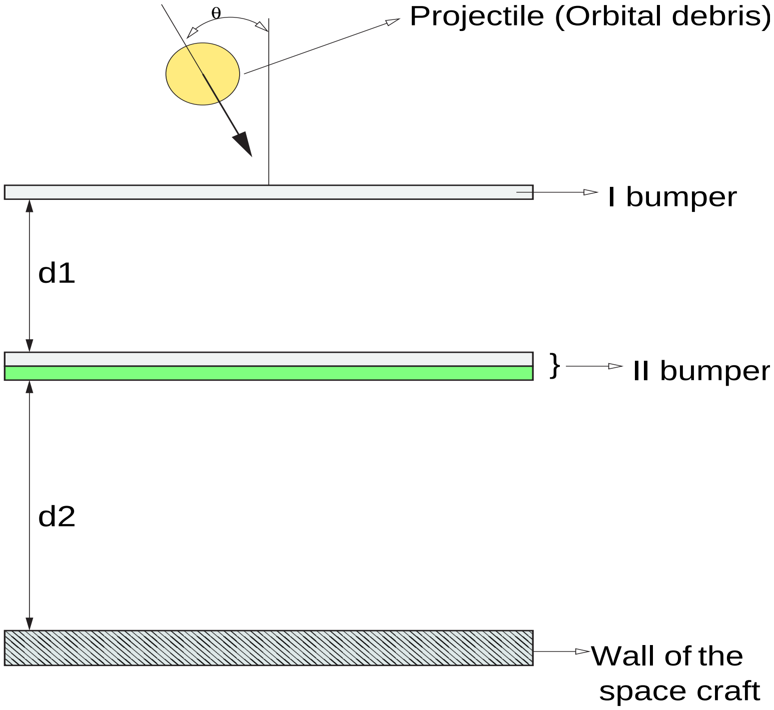

Figure 1.1: Typical orbital debris shield configuration

phase of this whole process. The numerical simulation of this multi-energy event requires high fidelity techniques which can handle all the three phases with ease.

1.5 Ballistic limit curves

The performance of a shield is mainly characterized by the extent of protection it offers against “damage” to the wall of the space craft. In orbital debris shield application, the term “damage” implies perforation or a detached spall of the rear wall. The sheer number of shield and impact parameters involved in quantifying the ability of the shield to defeat an incoming projectile/debris has forced researchers to take recourse to empirical techniques [11]. These empirical equations, developed based on a number of experiments, define the ballistic limit for a shield. Figure (1.2) shows ballistic limit curves for a Whipple shield, for different impact angles (in degrees) plotted using the ballistic limit equations developed by Eric Christiansen [11].

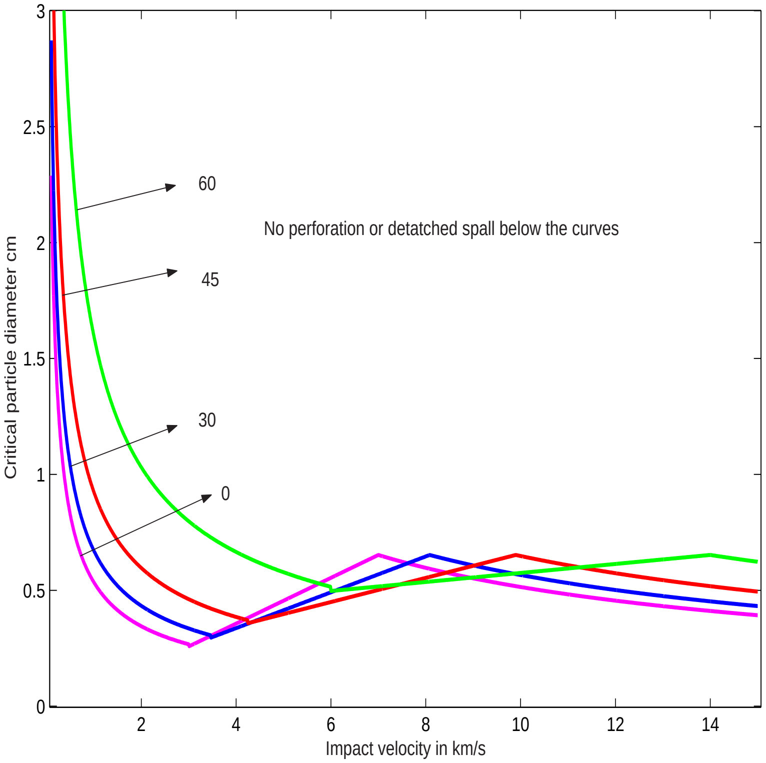

Figure 1.2: Ballistic limit curves for a Whipple shield configuration, areal density $= 1.25g/cm^2$, 0.127cm Al 6061-T6 bumper, 10.2 cm spacing, 0.32 cm Al 2219-T87 rear wall (labels in degrees)

The ballistic limit of a shield depends on a number of parameters including but not limited to material properties, shield geometry, impact velocities, impact obliquity and projectile shape. This has tremendously complicated the use of only experimental based techniques in orbital debris shield design studies. Numerical based techniques offer a low cost and faster turn around time for such problems. In the following section, a brief discussion about the various numerical modeling techniques available in the literature and their strengths and weaknesses to model hypervelocity impact of orbital debris on space structures is presented.

1.6 Literature Review

1.6.1 Mesh based techniques

Simulation studies in hypervelocity impact have traditionally relied on mesh based techniques like the Lagrangian finite difference [74], Lagrangian finite element [76] and the Eulerian finite element methods [76]. Finite difference based methods approximate the governing partial differential equations by finite difference equations. In contrast, finite element based methods take recourse to discretizing the domain under study by a set of sub-domains. The field variable is then approximated piece wise by a suitable choice of an interpolating polynomial. The coefficients of the polynomial represent the nodal values which are treated as unknowns. Over the last several years finite element procedures have matured and today it has reached a stage where it is probably the most widely used technique in computational mechanics. The details of this method can be found in any standard finite element texts [5] [34] [4].

In general, Lagrangian mesh based methods are efficient in modeling structural response of materials. However large mesh distortion and complexity in modeling contact-impact hinders the use of this method alone in modeling hypervelocity impact. Eulerian mesh based techniques avoid the mesh distortion problem faced by Lagrangian codes, but material diffusion across material interfaces and the inability to track true material time history, severely restricts the use of this technique [39]. The aforementioned draw backs of mesh based techniques has spurred research in alternative modeling techniques.

For a more comprehensive discussion on mesh based techniques for modeling hypervelocity impact phenomena, the reader is referred to the works of David Benson [7] or Charles Anderson [39].

1.6.2 Particle methods

Particle in cell methods

Particle in cell (PIC) [28] and its variants FLIP [8] [9] and material-point method [2] use moving particles to carry mass, momentum and thermal energy and a space fixed grid to compute non-advective terms in the equations of motion. Though simple and robust the method involves transfer of information back and forth between the fixed grid and the particles resulting in diffusion.

SPH methods

The smooth particle hydrodynamics (SPH) method [47] makes use of an interpolating function instead of an Eulerian type grid, as in PIC. Continuum laws including continuity equation, balance of momentum, conservation of energy are used in discrete form. Shocks are modeled by incorporating artificial viscosity and heat conduction into the model. Although the method is elegant in principle, a large number of deficiencies of this method have been a subject of concern amongst researchers. Some of the problems associated with SPH are

(i) Tensile instability

(ii) Poor accuracy

(iii) Complications in implementation of boundary conditions

In order to overcome these problems several “fixes” have been and are still being proposed [31] [61] [58] [14] [60] [72] [71] [49] [48] [36] [37].

1.6.3 Element free Galerkin and other meshless methods

Element free Galerkin methods [6], Reproducing kernel particle methods [45] and Multi-scale methods [44], specifically address the issue of consistency in approximating a function. Although significant progress has been made, the efficacy of these methods to solve significantly complicated problems (like orbital debris impact) have not been demonstrated.

1.6.4 Coupled methods

Particle based methods are typically used where strength effects are negligible. However, coupling particle methods with standard finite element methods, results in the ability to model structural response retaining all the advantages of using particle methods. G.R. Johnson [35] and S.W. Attaway *et al.* [1] have separately tried to couple SPH with finite element using a contact algorithm. A drawback of this method is that one needs to have an apriori knowledge of the region of impact in the target where the projectile strikes.

1.7 Motivation and scope of research

The pitfalls of the afore mentioned modeling methodologies to provide high fidelity simulation of hypervelocity impact of orbital debris on space structures has provided ample motivation for the development of alternate techniques.

In the present work a general hybrid particle finite element model to simulate hypervelocity impact of orbital debris on space structures is developed. The model development relies on energy principles. The continuum is discretized simultaneously into particles and finite elements. The center of mass of the particles serve as nodes of the finite element. Although the particles and elements are used simultaneously, they are not used redundantly. Particles are used to model kinetic energy effects and contact impact while Lagrangian finite elements are used to model strength effects. In the present formulation, particles are in general ellipsoidal in shape. This choice of shape enables modeling of structural members (such as shields) with significant aspect ratio with a relatively fewer particles resulting in significant savings in memory requirements. Shapiro *et al.* [64] and Owen *et al.* [57] have used ellipsoidal kernels in their development of adaptive smooth particle hydrodynamics (ASPH). A similar attempt using spheroidal kernels was proposed by Fulbright *et al.* [22]. These formulations in addition to carrying over the problems of SPH have added a significant share of their own. This is evident from the authors observation that ASPH fails to satisfy fundamental principles such as balance of angular momentum. In addition the use of Euler angles can only aggravate the problem due to the inherent singularities associated with this parameterization of rotation. By contrast model development here is devoid of these problems since it relies on energy principles and uses a four parameter, non-singular representation of rotation based on Euler parameters.

1.8 Dissertation Organization

The rest of the dissertation is organized as follows. In chapter (2) singularity free equations to model rotational dynamics of a rigid body are developed. Euler parameters are used as coordinates of orientation. Although the use of Euler parameters enables a better kinematic description, the presence of an algebraic constraint increases the complexity of modeling the dynamics. Lagrange multipliers are commonly used to handle this problem. Alternatively, the constraint can be differentiated twice and tied together with the dynamics at the acceleration level, an approach commonly found in differential algebraic equations (DAEs) literature.

In chapter (2) we develop Hamilton's equations of rigid body rotational dynamics devoid of any explicit lagrange multiplier. This reduces the solution procedure from solving DAEs to solving a system of first order nonlinear differential equations. Once the initial conditions are specified, these equations can be integrated using a standard numerical integration routine. Numerical examples are solved to test the efficacy of this solution procedure.

In chapter (3), a hybrid particle finite element model to simulate hypervelocity impact is developed. The classical weighted residual approach is abandoned in favor of a system dynamics approach. The energy of the system defines the Hamiltonian from which Hamilton's equations are derived. The introduction of an entropy variable provides the necessary frame work to couple mechanical and thermal energy domains. Hamilton's equations are a set of first order ordinary differential equations which can be integrated using a standard integration routine. The simulations are compared with available experimental results, based on which conclusions are drawn.

Chapter (4) presents advanced simulation results on projectile shape effects and the performance of different shielding geometries and materials. The simulation results are compared with experimental results.

Finally a summary of the present work and scope for future work are presented in chapter (5).

Chapter 2

Hamiltonian formulation of three dimensional rigid body dynamics using Euler parameters

2.1 Introduction

There are many sets of parameters to represent the rotation of a rigid body with respect to a reference coordinate system in three dimensional space [65]. Amongst them, Euler angles are most extensively studied in the literature. They are easy to visualize and are a non-redundant representation of rotation. However, they are plagued with singularities [3] [40]. Although there are other three parameter representations, such as Laning-Bortz-Stuelpnagel parameters [54], and Rodriguez parameters [65], they are all inherently singular. In fact, it appears that no three parameter representation of rotation is singularity free.

2.2 Preliminaries

The singularity issue associated with Euler angles is well known. However a brief discussion is provided here to introduce notation that will be used in this dissertation. The reader is referred to classical texts by Goldstein [24] or Greenwood [25] for a comprehensive discussion.

Let $\mathbf{x}, \mathbf{y}, \mathbf{z}$ represent a set of orthogonal unit vectors of a co-ordinate system (also called frame) $\{\mathbf{A}\}$ and $\mathbf{x}^{'}, \mathbf{y}^{'}, \mathbf{z}^{'}$ represent a set of orthogonal unit vectors of another co-ordinate system $\{\mathbf{A}^{'}\}$. Let $\mathbf{O}$ and $\mathbf{O}^{'}$ represent the origins of the two co-ordinate systems respectively.

Suppose the points $\mathbf{O}$ and $\mathbf{O}^{'}$ are fixed and co-incident in space so that there is no relative translation between the two frames, the rotation of frame $\{\mathbf{A}^{'}\}$ with respect to frame $\{\mathbf{A}\}$ can be represented by means of three successive rotations about non-parallel space fixed or body fixed axes. The three angles ϕ, θ and ψ which are rotations about three non-parallel body fixed axes are known as Euler angles. Depending on the axes of rotation, there are twelve possible different sequences of Euler angles [3]. For the purpose of illustration a 3-1-3 transformation is chosen. In this transformation, the frame $\{\mathbf{A}\}$ is rotated counterclockwise about the $\mathbf{z}$ axis by an angle ϕ. The resulting co-ordinate system $(\mathbf{x}^{'''}, \mathbf{y}^{'''}, \mathbf{z}^{'''})$ labeled $\{\mathbf{A}^{'''}\}$ is rotated counterclockwise about $\mathbf{x}^{'''}$ by an angle θ to obtain $(\mathbf{x}^{''}, \mathbf{y}^{''}, \mathbf{z}^{''})$ labeled $\{\mathbf{A}^{''}\}$. The frame $\{\mathbf{A}^{''}\}$ is then rotated counterclockwise about $\mathbf{z}^{''}$ to obtain frame $\{\mathbf{A}^{'}\}$. The transformation $\mathbf{R}$ that relates frame $\{\mathbf{A}\}$ with frame $\{\mathbf{A}^{'}\}$ can be written as a product of the three rotation matrices.

$$\begin{aligned}\mathbf{R} &= \begin{bmatrix} \cos(\phi) & -\sin(\phi) & 0 \\ \sin(\phi) & \cos(\phi) & 0 \\ 0 & 0 & 1 \end{bmatrix} \times \begin{bmatrix} 1 & 0 & 0 \\ 0 & \cos(\theta) & -\sin(\theta) \\ 0 & \sin(\theta) & \cos(\theta) \end{bmatrix} \times \\ & \begin{bmatrix} \cos(\psi) & -\sin(\psi) & 0 \\ \sin(\psi) & \cos(\psi) & 0 \\ 0 & 0 & 1 \end{bmatrix} \end{aligned} \tag{2.1}$$

Representing cos( ) as $C(\ )$ and sin( ) as $S(\ )$, and multiplying the matrices, equation(2.1) can be simplified to

$$\mathbf{R} = \begin{bmatrix} C(\phi)C(\psi) - S(\phi)C(\theta)S(\psi) & -C(\phi)S(\psi) - S(\phi)C(\theta)C(\psi) & S(\phi)S(\theta) \\ S(\phi)C(\psi) + C(\phi)C(\theta)S(\psi) & -S(\phi)S(\psi) + C(\phi)C(\theta)C(\psi) & -C(\phi)S(\theta) \\ S(\theta)S(\psi) & S(\theta)C(\psi) & C(\theta) \end{bmatrix} \tag{2.2}$$

$\mathbf{R}$ is a proper orthogonal matrix, i.e it has the following properties

- $\mathbf{R}^T = \mathbf{R}^{-1}$
- det($\mathbf{R}$)=+1

A vector ‘ $\mathbf{a}^{'}$ ’ represented in frame $\{\mathbf{A}^{'}\}$ can be represented in frame $\{\mathbf{A}\}$ by the transformation

$$\mathbf{a} = \mathbf{R}\,\mathbf{a}^{'} \tag{2.3}$$

The angular velocity of frame $\{\mathbf{A}^{'}\}$ with respect to frame $\{\mathbf{A}\}$ represented in the frame $\{\mathbf{A}^{'}\}$ can be obtained from the chain rule

$$\begin{aligned}\boldsymbol{\omega}_{\mathbf{A}}^{\mathbf{A}'} &= \boldsymbol{\omega}_{\mathbf{A}}^{\mathbf{A}'''} + \boldsymbol{\omega}_{\mathbf{A}'''}^{\mathbf{A}''} + \boldsymbol{\omega}_{\mathbf{A}''}^{\mathbf{A}'} \quad \text{or} \\ &= \dot{\phi}\mathbf{z} + \dot{\theta}\mathbf{x}''' + \dot{\psi}\mathbf{z}'' \end{aligned} \tag{2.4}$$

The vectors $\mathbf{z}, \mathbf{x}'''$ and $\mathbf{z}''$ can be expressed in frame $\{\mathbf{A}'\}$ by the following orthogonal relations

$$\mathbf{z} = S(\psi)S(\theta)\mathbf{x}' + C(\psi)S(\theta)\mathbf{y}' + C(\theta)\mathbf{z}' \tag{2.5}$$

$$\mathbf{x}''' = C(\psi)\mathbf{x}' - S(\psi)\mathbf{y}' \tag{2.6}$$

$$\mathbf{z}'' = \mathbf{z}' \tag{2.7}$$

Substituting equations (2.5), (2.6), (2.7) into equation (2.4), the following relation can be obtained for the angular velocity components in the body fixed frame

$$\begin{bmatrix} \omega_{x'} \\ \omega_{y'} \\ \omega_{z'} \end{bmatrix} = \begin{bmatrix} \sin(\theta)\sin(\psi) & \cos(\psi) & 0 \\ \sin(\theta)\cos(\psi) & -\sin(\psi) & 0 \\ \cos(\theta) & 0 & 1 \end{bmatrix} \begin{bmatrix} \dot{\phi} \\ \dot{\theta} \\ \dot{\psi} \end{bmatrix} \tag{2.8}$$

The matrix in equation (2.8) can be inverted to express the Euler angle rates in terms of the angular velocity.

$$\begin{bmatrix} \dot{\phi} \\ \dot{\theta} \\ \dot{\psi} \end{bmatrix} = \frac{1}{\sin(\theta)} \begin{bmatrix} \sin(\psi) & \cos(\psi) & 0 \\ \cos(\psi)\sin(\theta) & -\sin(\psi)\sin(\theta) & 0 \\ -\sin(\psi)\cos(\theta) & -\cos(\psi)\cos(\theta) & \sin(\theta) \end{bmatrix} \begin{bmatrix} \omega_{x'} \\ \omega_{y'} \\ \omega_{z'} \end{bmatrix} \tag{2.9}$$

The integration of the above equations results in numerical problems if $\sin(\theta)$ is close to zero or when $\theta = n\pi, n = 0, \pm 1, \pm 2 \ldots$. This can be circumvented by switching to a different Euler angle representation. However, this approach does not get rid of the inherent singularity, instead it merely shifts it away from the configuration of interest.

2.3 Euler parameters

There are a number of redundant representations of rotation including the Euler parameters, Cayley-Klien parameters, Hopf parameters, quaternion, direction cosines and others [54]. Amongst them Euler parameters seems to be most favorable [67] for the following reasons.

- They are easily related to the rotation matrix
- They are well behaved
- They are computationally efficient.

The motivation for a four parameter representation comes from the Euler's theorem which can be stated as follows [25]

> “ The most general displacement of a rigid body is equivalent to a translation of some point in the body plus a rotation about an axis through that point.”

A set of four quantities e_0, e_1, e_2, e_3 defined as follows:

$$e_0 = \cos(\tfrac{\phi}{2}),\ e_i = c_i \sin(\tfrac{\phi}{2}),\ i = 1, 2, 3$$

are called Euler parameters. $c_i, = \cos(\theta_i)\ i = 1, 2, 3$ are the direction cosines of the axis and ϕ is the rotation about the axis. Since any non-redundant representation of rotation must have only three independent parameters, the Euler parameters must

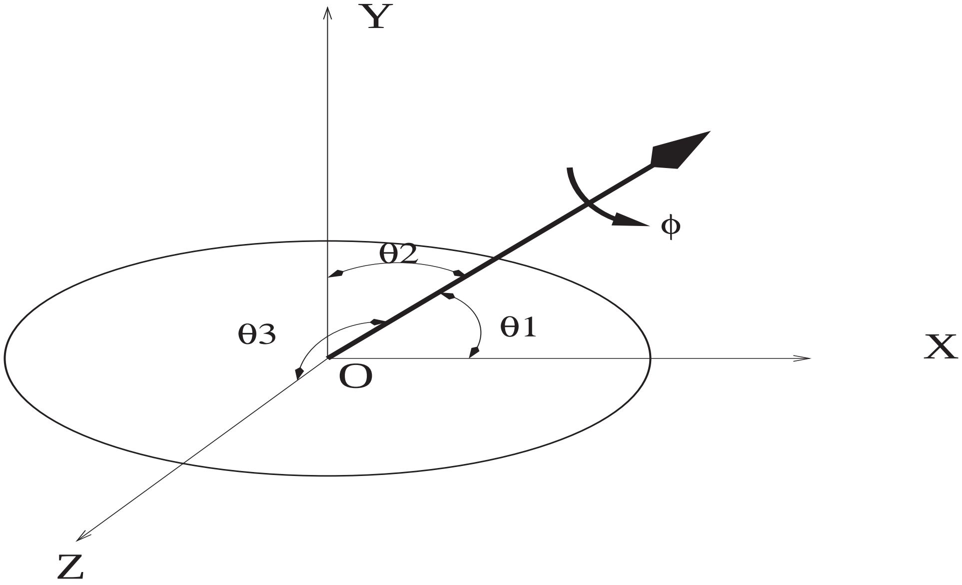

Figure 2.1: Euler parameter representation

satisfy a (holonomic) constraint

$$\sum_{i=0}^{3} {e_i}^2 = 1. \tag{2.10}$$

Although the kinematics turns out to be simple, the presence of an algebraic constraint (equation(2.10)) complicates the representation of rotational dynamics of a rigid body. Lagrange multipliers are most commonly used to handle algebraic constraints leading to set of differential algebraic equations (DAE) [3]. The solution of such equations requires sophisticated DAE solvers and forms a whole area of research in itself. In the works of Nikravesh and his co-workers [50] [52] [51], Lagrangian formulations for constrained multi-body mechanical systems are developed. The formulation makes uses of a Lagrange multiplier (obtained in a closed form) to enforce the Euler parameter constraint. However the formulation does not include any potential function in the Lagrangian. Similar results have been shown by other researchers using a different approach [70]. Morton [40] derives the Hamilton's equations of rotational rigid body dynamics by extending the momenta space by one. In other words, the equations of rotational dynamics are formulated using four generalized momenta and four Euler parameters. This makes the algebra easier as one has to deal with only square matrices. However it involves the introduction of an arbitrary positive definite parameter into the formulation. Chang and Chou [10] present a Lagrangian based formulation of rigid body rotational dynamics. The formulation is devoid of any Lagrange multiplier to impose the Euler parameter constraint.

In the following sections, an elegant Hamiltonian based formulation of rigid body dynamics using Euler parameters is presented. By a suitable manipulation of terms and using the chain rule of calculus a system of first order differential equations governing the unconstrained dynamics of a rigid body is derived. This system of first order nonlinear differential equations can be numerically integrated using a standard integration routine. Unlike Morton [40] this formulation uses three angular momenta and four euler parameters as state variables. The present formulation does not carry the constraint as an auxiliary differential equation, as has been described by some authors [62].

Symplectic integrators [66] provide robustness, strict energy conservation and structure preserving properties, for Hamiltonian (non-dissipative) systems. Symplectic integrators has been a subject of active interest in recent times. The present work however does not focus on this subject.

The rest of the chapter is organized as follows. First, the kinematics of rigid body motion are established. In the subsequent sections, the equations of unconstrained rigid body dynamics are developed. Three example problems are solved to show the efficacy of the solution procedure. The first problem is a simple harmonic motion of a rotating disk. The second problem is a torque free motion of an unconstrained three dimensional rigid body. The third problem is a classic problem of the motion of a spinning top in a gravitational field. Finally conclusions are drawn based on the results.

2.4 Rigid body kinematics

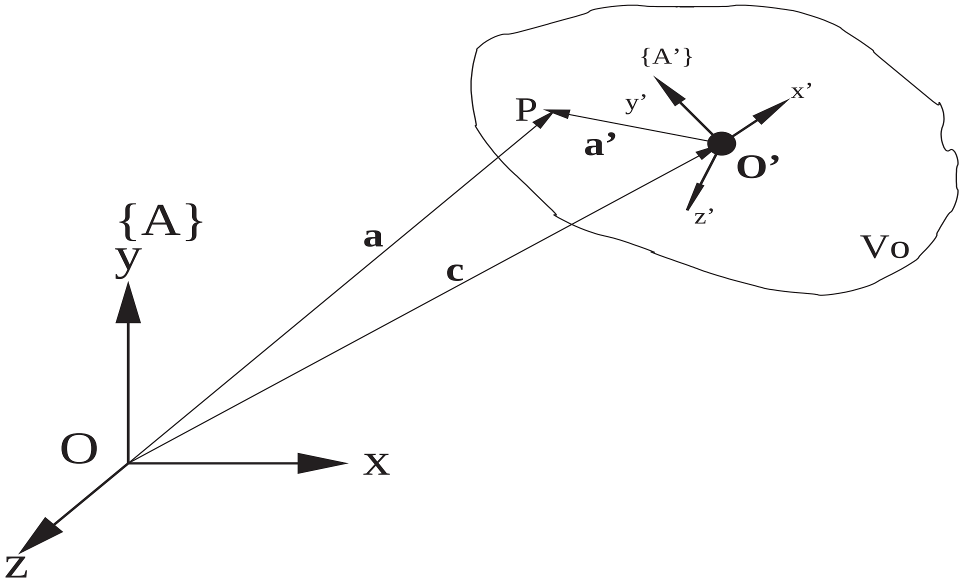

Let $\mathbf{O}^{'}$ represent the center of mass of a rigid body $\mathbb{B}$ which occupies a constant volume V_0 in the body fixed frame $\{\mathbf{A'}\}$. Let $\{\mathbf{A}\}$ represent the global frame with origin at $\mathbf{O}$. Let $\mathbf{c}$ be the vector locating the center of mass of the rigid body. $\mathbf{R}$ is the rotation matrix that represents the orientation of the rigid body with respect to a global frame $\{\mathbf{A}\}$ respectively. The location of a material point P located at $\mathbf{a}^{'}$ in the frame $\{\mathbf{A}^{'}\}$ can then be expressed in the global frame $\{\mathbf{A}\}$ by the relation

$$\mathbf{a}(t) \quad = \quad \mathbf{R}(t)\, \mathbf{a}^{'} + \mathbf{c}(t) \tag{2.11}$$

where $\mathbf{R}(t)$ is a 3×3 rotation matrix which represents the rotation of the rigid body (frame $\{\mathbf{A}^{'}\}$) with respect to the global frame. With the understanding that the rotation is a function of time, unless otherwise mentioned, the explicit indication of time dependence shall be abandoned in favor of a more compact notation $\mathbf{R}$. The vector $\mathbf{c}(t)$ locates the center of mass position of the rigid body in the global frame $\{\mathbf{A}\}$. The rotation matrix is expressed in terms of four Euler parameters. Specifically, $\mathbf{R}(e_0, e_1, e_2, e_3)$ can be decomposed as a product two rectangular matrices [53]

$$\mathbf{R} \quad = \quad \mathbf{E}\,\mathbf{G}^T \qquad \text{where} \tag{2.12}$$

$$\mathbf{E} \quad = \quad \begin{bmatrix} -e_1 & e_0 & -e_3 & e_2 \\ -e_2 & e_3 & e_0 & -e_1 \\ -e_3 & -e_2 & e_1 & e_0 \end{bmatrix} \qquad \text{and} \tag{2.13}$$

$$\mathbf{G} \quad = \quad \begin{bmatrix} -e_1 & e_0 & e_3 & -e_2 \\ -e_2 & -e_3 & e_0 & e_1 \\ -e_3 & e_2 & -e_1 & e_0 \end{bmatrix} \tag{2.14}$$

Let the angular velocity of the rigid body expressed in the frame $\{\mathbf{A}^{'}\}$ be $\boldsymbol{\omega}^{'} = \left[\omega_{x'}, \omega_{y'}, \omega_{z'}\right]^T$. Let $\mathbf{e} = [e_0, e_1, e_2, e_3]^T$ represent a 4×1 vector of Euler parameters. The angular velocity is related to the Euler parameters by the following identity [53]:

$$\boldsymbol{\omega}^{'} = 2\,\mathbf{G}\,\dot{\mathbf{e}} = -2\,\dot{\mathbf{G}}\mathbf{e} \tag{2.15}$$

2.5 Equations of motion

2.5.1 Kinetic energy

The kinetic co-energy T^* can in general be expressed as

$$T^* = \frac{1}{2}\int_V \rho\, \dot{\mathbf{a}}' \cdot \dot{\mathbf{a}}'\, dV \tag{2.16}$$

Substituting equation (2.11) into (2.16), the kinetic energy can be divided into three contributions.

$$T^* = T_1^* + T_2^* + T_3^* \tag{2.17}$$

where

$$T_1^* = \frac{1}{2}\int_{V_0} \dot{\mathbf{c}}^T \dot{\mathbf{c}} \rho dV \tag{2.18}$$

$$T_2^* = \int_{V_0} \dot{\mathbf{c}}^T \mathbf{R}\mathbf{a}' \rho dV \tag{2.19}$$

$$T_3^* = \frac{1}{2}\int_{V_0} \left(\dot{\mathbf{R}}\mathbf{a}'\right)^T \left(\dot{\mathbf{R}}\mathbf{a}'\right) \rho dV \tag{2.20}$$

Equation (2.18) represents the translational kinetic energy and can be simplified as

$$T_1^* = \frac{1}{2} m\, \dot{\mathbf{c}}^T \dot{\mathbf{c}} \tag{2.21}$$

where ‘ m ’ is the total mass of the rigid body defined as

$$m = \int_{V_0} \rho dV \tag{2.22}$$

T_2^* represents the kinetic energy due to coupling between translation and rotational motions. From the definition of the center of mass, the body fixed coordinates of the rigid body can be computed as

$$\mathbf{a}_{cg}^{'} = \frac{1}{m}\int_{V_0} \mathbf{a}^{'}\rho\, dV \tag{2.23}$$

The coupling kinetic energy can then be expressed in terms of the center of mass coordinates as

$$T_2^* = m\,\dot{\mathbf{c}}^T\,\dot{\mathbf{R}}\,\mathbf{a}_{cg}^{'} \tag{2.24}$$

Note that

$$\dot{\mathbf{R}} = \mathbf{R}\tilde{\boldsymbol{\omega}}^{'} \tag{2.25}$$

where $\tilde{\boldsymbol{\omega}}^{'}$ is 3x3 skew symmetric form of the three component vector $\boldsymbol{\omega}^{'}$. Substituting equation (2.25) into equation (2.24),

$$T_2^* = m\,\dot{\mathbf{c}}^T\,\mathbf{R}\,\tilde{\boldsymbol{\omega}}^{'}\,\mathbf{a}_{cg}^{'} \tag{2.26}$$

If the center of mass of the rigid body is chosen as a reference point (i.e the origin of the body fixed frame coincides with the center of mass of the rigid body) then the coupling energy T_2^* vanishes.

$$T_2^* = 0 \tag{2.27}$$

T_3^* represents the rotational kinetic energy of the rigid body about point $O^{'}$. Substituting equation (2.25) into equation (2.20), the expression for the rotational kinetic energy can be written as

$$\begin{aligned} T_3^* &= \frac{1}{2}\int_{V_0} \rho \mathbf{a}^{'T}\left(\mathbf{R}\tilde{\boldsymbol{\omega}}^{'}\right)^T\left(\mathbf{R}\tilde{\boldsymbol{\omega}}^{'}\right)\mathbf{a}^{'} dV && (2.28) \\ &= \frac{1}{2}\int_{V_0} \rho \left(\tilde{\boldsymbol{\omega}}^{'}\mathbf{a}^{'}\right)^T\left(\tilde{\boldsymbol{\omega}}^{'}\mathbf{a}^{'}\right) dV && (2.29) \\ &= \frac{1}{2}\int_{V_0} \rho \left(-\boldsymbol{\omega}^{'}\tilde{\mathbf{a}}^{'}\right)^T\left(-\boldsymbol{\omega}^{'}\tilde{\mathbf{a}}^{'}\right) dV && (2.30) \\ &= \frac{1}{2}\boldsymbol{\omega}^{'T}\left(\int_{V_0} \rho \tilde{\mathbf{a}}^{'T}\tilde{\mathbf{a}}^{'} dV\right)\boldsymbol{\omega}^{'} && (2.31) \\ &= \frac{1}{2}\boldsymbol{\omega}^{'T}\mathbf{J}^{'}\boldsymbol{\omega}^{'} && (2.32) \end{aligned}$$

where $\tilde{\mathbf{a}}^{'}$ is the skew symmetric matrix of the three component vector $\mathbf{a}^{'}$. The symmetric matrix $\mathbf{J}^{'}$ is the inertia tensor of the rigid body expressed in the body fixed frame and is defined as

$$\mathbf{J}^{'} = \int_{V_0} \rho \tilde{\mathbf{a}}^{'} \otimes \tilde{\mathbf{a}}^{'} dV \qquad (2.33)$$

or

$$\mathbf{J}^{'} = \begin{bmatrix} J_{x'x'} & J_{x'y'} & J_{x'z'} \\ J_{y'x'} & J_{y'y'} & J_{y'z'} \\ J_{z'x'} & J_{z'y'} & J_{z'z'} \end{bmatrix} \qquad (2.34)$$

Substituting equation (2.15) into equation (2.32), the kinetic co-energy can be expressed as

$$T_3^* \;=\; 2\,\dot{\mathbf{e}}^T\,\mathbf{G}^T\,\mathbf{J}\,\mathbf{G}\,\dot{\mathbf{e}} \tag{2.35}$$

Using the identity

$$\mathbf{G}\,\dot{\mathbf{e}} = -\dot{\mathbf{G}}\,\mathbf{e} \tag{2.36}$$

equation (2.35) can be rewritten as

$$T_3^* \;=\; 2\,\mathbf{e}^T\,\dot{\mathbf{G}}^T\,\mathbf{J}\,\dot{\mathbf{G}}\,\mathbf{e} \tag{2.37}$$

Let the four component angular momenta $\mathbf{h}_e$ be defined as

$$\mathbf{h_e} \;=\; \frac{\partial T_3^*}{\partial \dot{\mathbf{e}}} \tag{2.38}$$

$$\;=\; 4\,\mathbf{G}^T\,\mathbf{J}\,\mathbf{G}\,\dot{\mathbf{e}} \tag{2.39}$$

Let $\mathbf{h}^{'}$ be the three component angular momenta defined in the standard form

$$\mathbf{h}^{'} = \mathbf{J}\,\boldsymbol{\omega}^{'} \tag{2.40}$$

Substituting equation (2.40) into equation (2.39)

$$\mathbf{h_e} \;=\; 2\,\mathbf{G}^T\,\mathbf{h}^{'} \tag{2.41}$$

Multiplying both sides of the above equation by $\mathbf{G}$ and noting that $\mathbf{G}^T\mathbf{G} = \mathbf{I}$

(identity matrix), the inverse relation can be written as

$$\mathbf{h}^{'} = \frac{1}{2}\mathbf{G}\,\mathbf{h_e} \tag{2.42}$$

Legendre transformation of equation (2.17), then yields kinetic energy in terms of the center of mass momenta $\mathbf{p}$ and the distributed momenta $\mathbf{h}^{'}$

$$T = \left[\mathbf{p}\cdot\dot{\mathbf{c}} + \mathbf{h}^{'}\cdot\boldsymbol{\omega}^{'}\right] - T^{*} \tag{2.43}$$

$$= \frac{1}{2}\left[m^{-1}\mathbf{p}^{T}\mathbf{p} + \mathbf{h}^{'T}\mathbf{J}^{'-T}\mathbf{h}^{'}\right] \tag{2.44}$$

Substituting equation (2.42) into equation (2.44), equation (2.44) can be rewritten as

$$= \frac{1}{2}m^{-1}\mathbf{p}^{T}\mathbf{p} + \frac{1}{8}\mathbf{h_e}^{T}\,\mathbf{G}^{T}\mathbf{J}^{'-T}\,\mathbf{G}\mathbf{h_e} \tag{2.45}$$

2.5.2 Potential energy

The potential energy is a function of the position and orientation of the rigid body and can be written in functional form as

$$V = V(\mathbf{c}, e_0, e_1, e_2, e_3) \tag{2.46}$$

2.5.3 Non-conservative forces

Any generalized force that cannot be derived from a potential function appears explicitly on the right hand side in the equations of motion. Forces due to friction, time varying forcing functions, and forces arising due to nonholonomic constraints are some examples of non-conservative forces.

2.5.4 Hamilton's equations

The Hamiltonian of the system is the sum of kinetic and potential energies.

$$\Pi = T \ + \ V \quad = \quad \Pi(\mathbf{p}, \mathbf{h}_{\mathbf{e}}^{'}, \mathbf{c}, \mathbf{e}) \tag{2.47}$$

The Hamilton's equations in canonical form are

$$\dot{\mathbf{p}} \quad = \quad -\frac{\partial \Pi}{\partial \mathbf{c}} + \mathbf{Q}_{nc}^{p} \tag{2.48}$$

$$\dot{\mathbf{c}} \quad = \quad \frac{\partial \Pi}{\partial \mathbf{p}} \tag{2.49}$$

$$\dot{\mathbf{h}}_{\mathbf{e}} \quad = \quad -\frac{\partial \Pi}{\partial \mathbf{e}} + \mathbf{Q}_{nc} \tag{2.50}$$

$$\dot{\mathbf{e}} \quad = \quad \frac{\partial \Pi}{\partial \mathbf{h}_{\mathbf{e}}} \tag{2.51}$$

Next, we introduce a Lagrange multiplier λ to satisfy the following equality constraint,

$$\dot{\mathbf{e}}^{T}\mathbf{e} \quad = \quad 0 \tag{2.52}$$

The term $\frac{\partial \Pi}{\partial \mathbf{e}}$ on the right hand side of equation (2.50) can be simplified as follows

$$\frac{\partial \Pi}{\partial \mathbf{e}} \quad = \quad \frac{\partial T}{\partial \mathbf{e}} + \frac{\partial V}{\partial \mathbf{e}} \tag{2.53}$$

$$\quad = \quad -4\,\dot{\mathbf{G}}^{T}\,\mathbf{J}\,\dot{\mathbf{G}}\mathbf{e} + \frac{\partial V}{\partial \mathbf{e}} \tag{2.54}$$

$$= -2\,\dot{\mathbf{G}}^T\,\mathbf{J}\left(-\boldsymbol{\omega}^{'}\right)+\frac{\partial V}{\partial \mathbf{e}} \tag{2.55}$$

$$= 2\,\dot{\mathbf{G}}^T\,\mathbf{h}^{'}+\frac{\partial V}{\partial \mathbf{e}} \tag{2.56}$$

Differentiating equation (2.42) with respect to time on both sides one obtains

$$\dot{\mathbf{h}}^{'} = \frac{1}{2}\left\{\dot{\mathbf{G}}\mathbf{h}_{\mathbf{e}}+\mathbf{G}\dot{\mathbf{h}}_{\mathbf{e}}\right\} \tag{2.57}$$

$$= \frac{1}{2}\left\{4\,\dot{\mathbf{G}}\,\mathbf{G}^T\,\mathbf{J}\,\mathbf{G}\,\dot{\mathbf{e}}+\mathbf{G}\dot{\mathbf{h}}_{\mathbf{e}}\right\} \tag{2.58}$$

$$= \frac{1}{2}\left\{2\,\dot{\mathbf{G}}\,\mathbf{G}^T\,\mathbf{h}^{'}+\mathbf{G}\dot{\mathbf{h}}_{\mathbf{e}}\right\} \tag{2.59}$$

Substituting equation (2.50) into equation (2.59), equation (2.59) can be rewritten as

$$\dot{\mathbf{h}}^{'} = \frac{1}{2}\left[2\,\dot{\mathbf{G}}\,\mathbf{G}^T\,\mathbf{h}^{'}+\mathbf{G}\left\{-\frac{\partial \Pi}{\partial \mathbf{e}}+\lambda\mathbf{e}+\mathbf{Q}_{ext}\right\}\right] \tag{2.60}$$

where

$$\mathbf{Q}_{ext} = \mathbf{Q}_{nc}-\lambda\,\mathbf{e} \tag{2.61}$$

Substituting equation (2.56) into equation (2.60) results in

$$\dot{\mathbf{h}}^{'} = \frac{1}{2}\left[2\,\dot{\mathbf{G}}\,\mathbf{G}^T\,\mathbf{h}^{'}+\mathbf{G}\left\{-2\,\dot{\mathbf{G}}^T\,\mathbf{h}^{'}-\frac{\partial V}{\partial \mathbf{e}}+\lambda\mathbf{e}+\mathbf{Q}_{ext}\right\}\right] \tag{2.62}$$

Using the identities

(i)

$$\mathbf{G}\ \mathbf{e} = 0 \tag{2.63}$$

(ii)

$$\mathbf{\Omega}^{'} = 2\mathbf{G}\dot{\mathbf{G}}^T = -2\dot{\mathbf{G}}\mathbf{G}^T \tag{2.64}$$

where $\mathbf{\Omega}^{'}$ is the skew symmetric matrix

$$\mathbf{\Omega}^{'} = \begin{bmatrix} 0 & -\omega_{z'} & \omega_{y'} \\ \omega_{z'} & 0 & -\omega_{x'} \\ -\omega_{y'} & \omega_{x'} & 0 \end{bmatrix} \tag{2.65}$$

equation (2.62) can be simplified as

$$\dot{\mathbf{h}}^{'} = -\mathbf{\Omega}^{'}\mathbf{h}^{'} - \frac{1}{2}\mathbf{G}\frac{\partial V}{\partial \mathbf{e}} + \frac{1}{2}\mathbf{G}\mathbf{Q}_{ext} \tag{2.66}$$

Simplification of equation (2.51) results in

$$\dot{\mathbf{e}} = \frac{1}{2}\ \mathbf{G}^T\boldsymbol{\omega}^{'} \tag{2.67}$$

Summarizing, the Hamilton's equations of motion can be written as

$$\dot{\mathbf{p}} = -\mathbf{g} + \mathbf{Q}_{nc}^{p} \tag{2.68}$$

$$\dot{\mathbf{c}} = m^{-1}\mathbf{p} \tag{2.69}$$

$$\dot{\mathbf{h}}' = -\boldsymbol{\Omega}'\mathbf{h}' - \frac{1}{2}\mathbf{G}\frac{\partial V}{\partial \mathbf{e}} + \frac{1}{2}\mathbf{G}\mathbf{Q}_{ext} \tag{2.70}$$

$$\dot{\mathbf{e}} = \frac{1}{2}\,\mathbf{G}^T\boldsymbol{\omega}' \tag{2.71}$$

2.6 Thermo-mechanical coupling

Most literature on analytical dynamics includes an extensive discussion of Hamilton's principle and Lagrange's and Hamilton's equations for general three dimensional motion of rigid bodies. However the model development typically ignores any thermo-mechanical coupling. The Hamilton's equations derived in the previous section can be extended to include thermal effects.

For a thermo-mechanical system, the appropriate stored energy potential is the internal energy U. The stored energy function is in general a function of the mass density ρ and entropy of density the system s. The Hamiltonian for a thermo-mechanical system is

$$\Pi = T \;+\; U = \Pi(\mathbf{p}, \mathbf{h}', \mathbf{c}, \rho, s) \tag{2.72}$$

Entropy evolution equations of the form

$$\dot{S} = \dot{S}^{irr} \tag{2.73}$$

can be introduced, where $\dot{S}^{irr}$ is the rate of irreversible entropy production, calculated from the energy dissipation rate ($\dot{W}$)

$$\dot{S}^{irr} = \left(\frac{1}{\Theta}\right)\dot{W} \tag{2.74}$$

where Θ is the temperature of the rigid body.

For viscous damping effects, the energy dissipation rate is given by

$$\dot{W} = \mathbf{f}^p \cdot \dot{\mathbf{c}} + \boldsymbol{\tau}^{h'} \cdot \boldsymbol{\omega}' \tag{2.75}$$

where $\mathbf{f}^p$ and $\boldsymbol{\tau}^{h'}$ define the viscous force due to translation and rotation respectively.

2.6.1 Hamilton's equations

The canonical form of Hamilton's equations can be written as

$$\dot{\mathbf{p}} = -\frac{\partial \Pi}{\partial \mathbf{c}} + \mathbf{Q}^p_{nc} \tag{2.76}$$

$$\dot{\mathbf{c}} = \frac{\partial \Pi}{\partial \mathbf{p}} \tag{2.77}$$

$$\dot{\mathbf{h}}_{\mathbf{e}} = -\frac{\partial \Pi}{\partial \mathbf{e}} + \mathbf{Q}_{nc} \tag{2.78}$$

$$\dot{\mathbf{e}} = \frac{\partial \Pi}{\partial \mathbf{h}_{\mathbf{e}}} \tag{2.79}$$

$$0 = -\frac{\partial \Pi}{\partial S} + Q^s \tag{2.80}$$

Note that equations (2.76-2.79) are the same as equations (2.48-2.51). Let γ be the Lagrange multiplier associated with equation (2.73), then

$$Q^s = \gamma \tag{2.81}$$

$$\mathbf{Q}^p_{nc} = -\left(\frac{\gamma}{\Theta}\right) \mathbf{f}^p + \mathbf{f}^c \tag{2.82}$$

$$\mathbf{Q}_{nc} = -\left(\frac{\gamma}{\Theta}\right) \boldsymbol{\tau}^{h'} + \lambda\, \mathbf{e} + \boldsymbol{\tau}^c \tag{2.83}$$

In the above equations, $\mathbf{f}^c$ and $\boldsymbol{\tau}^c$ arise from the mechanical constraints. Equation (2.80) requires that $\Theta = Q^s$. In other words, the Lagrange multiplier corresponding to equation (2.73) is the thermodynamic temperature. Finally Hamilton's equations for a thermo-mechanical system can be written as

$$\dot{\mathbf{p}} = -\mathbf{g} + \mathbf{f}^p + \mathbf{f}^c \tag{2.84}$$

$$\dot{\mathbf{c}} = m^{-1}\mathbf{p} \tag{2.85}$$

$$\dot{\mathbf{h}}' = -\frac{1}{2}\,\mathbf{G}\,\boldsymbol{\tau} - \boldsymbol{\Omega}'\,\mathbf{h}' + \frac{1}{2}\,\mathbf{G}\left\{\boldsymbol{\tau}^{h'} + \boldsymbol{\tau}^c\right\} \tag{2.86}$$

$$\dot{\mathbf{e}} = \frac{1}{2}\,\mathbf{G}^T\boldsymbol{\omega}' \tag{2.87}$$

$$\dot{S} = \dot{S}^{irr} \tag{2.88}$$

2.7 Numerical examples

The preceding results are used to solve the following example problems.

2.7.1 Single degree of freedom system

Consider a rigid circular disk of radius ‘ r ’ rotating about a fixed point ‘ O ’. Let x', y' and z' form a right handed coordinate system in the body fixed frame $\{\mathbf{A}'\}$ with its origin at ‘ O ’. A linear spring is connected between point ‘ P ’ on the disk and ground, as shown in the figure (2.2). The coordinates of the point ‘ P ’ in the body fixed frame and global frame are (x', y', z') and (x, y, z) respectively. The

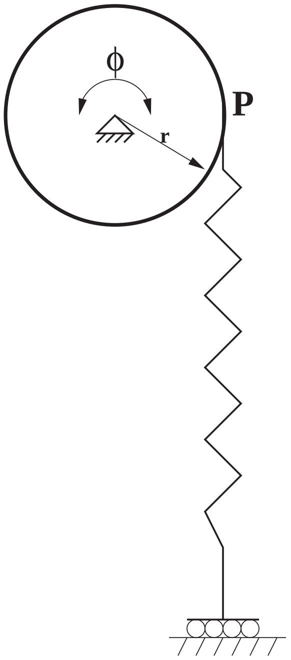

Figure 2.2: Circular disk with a spring

orientation of the disk with respect to the global frame $\{\mathbf{A}\}$ is given by

$$\begin{bmatrix} x & y & z \end{bmatrix}^T = \mathbf{R}\begin{bmatrix} x' & y' & z' \end{bmatrix}^T \tag{2.89}$$

where $\mathbf{R}$ is the rotation matrix. Although the use of Euler parameters seems to be unnecessary for this problem, their use serves to verify the formulation.

2.7.2 Equations of motion

The coordinates of the point ‘ P ’ in the global frame are related to the coordinates in the body fixed frame by the relation

$$\begin{bmatrix} x_p & y_p & z_p \end{bmatrix}^T = \mathbf{R}\begin{bmatrix} x_p' & y_p' & z_p' \end{bmatrix}^T \tag{2.90}$$

The elements of $\mathbf{R}$ can be written in terms of

- Euler parameters

$$\mathbf{R} = \begin{bmatrix} 2(e_0^2+e_1^2)-1.0 & 2(e_1e_2-e_0e_3) & 2(e_1e_3+e_0e_2) \\ 2(e_1e_2+e_0e_3) & 2(e_0^2+e_2^2)-1.0 & 2(e_2e_3-e_0e_1) \\ 2(e_1e_3-e_0e_2) & 2(e_2e_3+e_0e_1) & 2(e_0^2+e_3^2)-1.0 \end{bmatrix} \quad (2.91)$$

- Euler angles

$$\mathbf{R} = \begin{bmatrix} \cos\phi & -\sin\phi & 0 \\ \sin\phi & \cos\phi & 0 \\ 0 & 0 & 1 \end{bmatrix} \quad (2.92)$$

Initially the two frames $\mathbf{A}$ and $\mathbf{A}^{'}$ are coincident. Hence $[x_{pinitial}, y_{pinitial}, z_{pinitial}] = (r, 0, 0)$.

The kinetic co-energy and the potential energy of the system can be written as

$$T^* = \frac{1}{2}\boldsymbol{\omega}^{'T}\mathbf{J}^{'}\boldsymbol{\omega}^{'} \quad (2.93)$$

$$V = \frac{1}{2}k\left\{(y - y_{pinitial})^2\right\} \quad (2.94)$$

Note that the potential energy is a function of the euler parameters.

The expressions for the energy given by equations (2.93) and (2.94) are used in deriving the Hamilton's equations of motion, as described in the previous section.

The equations of motion can also be derived in terms of the Euler angle ϕ,

$$J_{z'z'}\ddot{\phi} + \frac{k}{2}r\sin(2\phi) = 0 \quad (2.95)$$

Its difficult to find a closed form solution of equation (2.95) for a general ϕ. However it is possible to numerically integrate equation (2.95) accurately using a standard integration routine. Specifically a fourth order Runge Kutta with a fixed time step of 0.001 sec is used here. The solution thus obtained is compared with the numerical solution of Hamilton's equations (2.70) and (2.71).

Parameter	
Mass moment of inertia of the disk($kg - m^2$)	$J_{x'x'} = J_{y'y'} = 1.0, J_{z'z'} = 2.0$
Radius of the disk(m)	r=1
Stiffness of the spring(N/m)	k=10
Initial displacement	$\phi_0 = 30^o$

Table 2.1: Simulation parameters

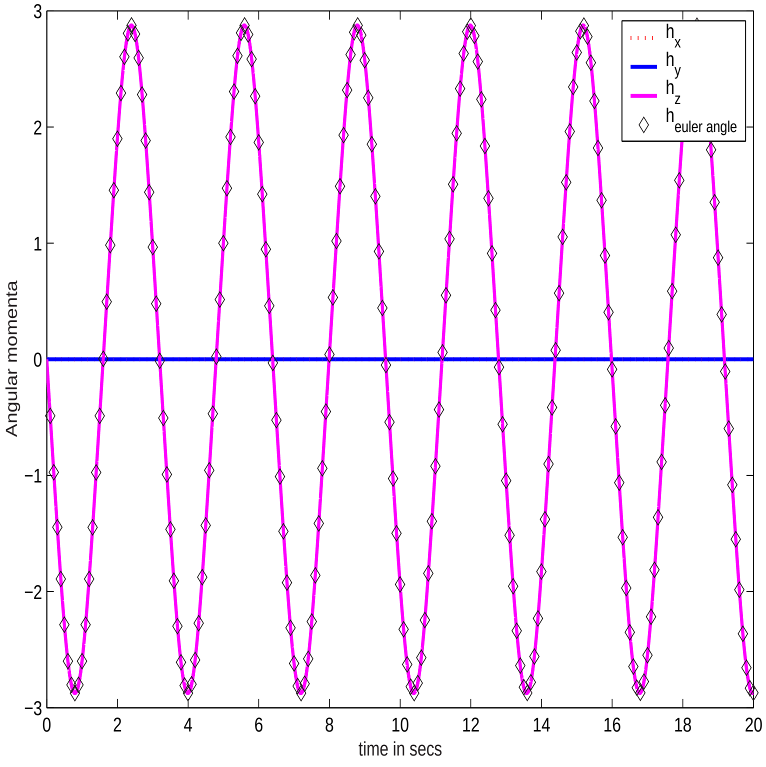

Figure 2.3: Angular momenta versus time

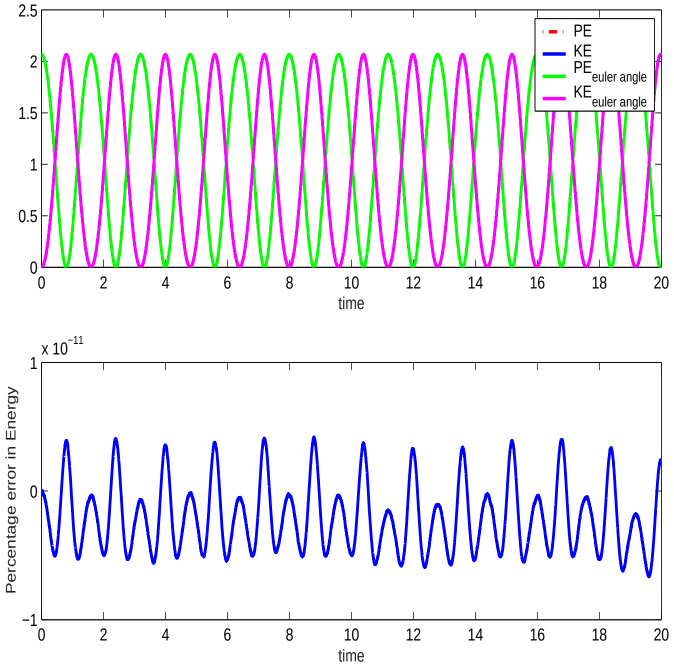

Figure 2.4: Total energy and percentage error in energy versus time

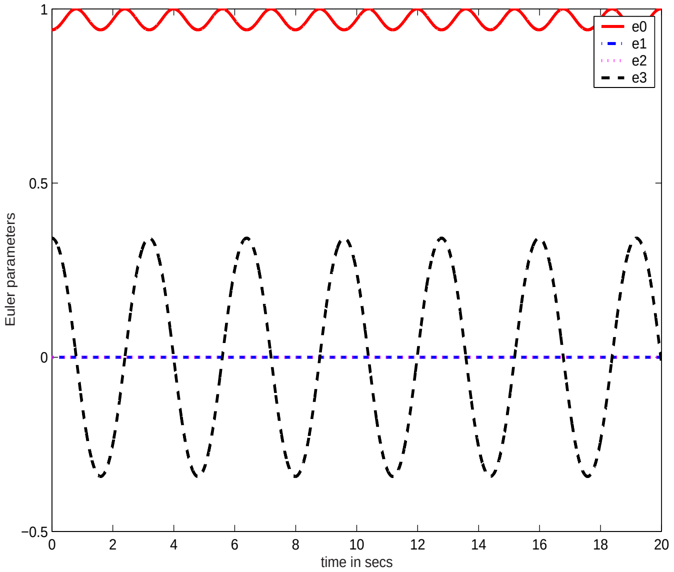

Figure 2.5: Euler parameters versus time

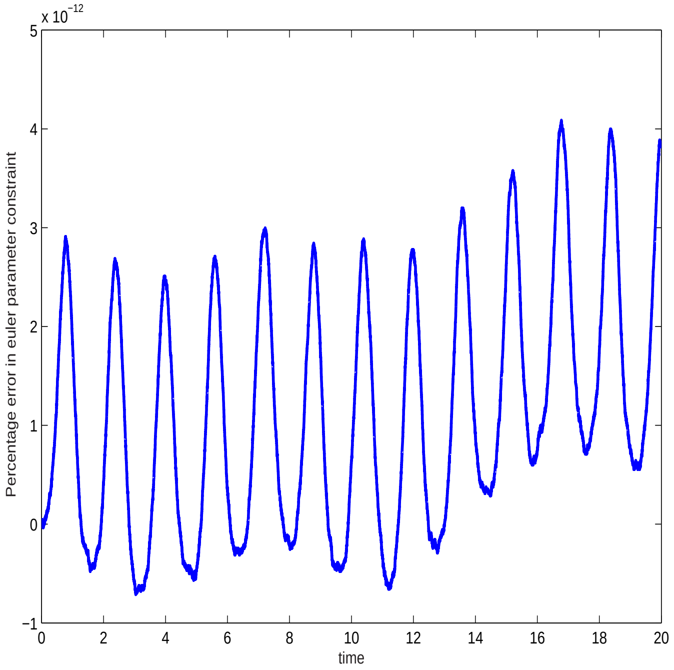

Figure 2.6: Percentage error in euler parameter constraint time

Simulation results shown in figures (2.3) and (2.4) show good agreement between the numerical solution of equation (2.95) and the numerical solution of Hamilton's equations using Euler parameters developed in this chapter.

2.7.3 Torque free motion of a rigid body

The specific problem selected here is the one analyzed by Morton [40]. The equations of rotational motion of a torque free rigid body are simulated using the Hamiltonian equations derived earlier. The model is conservative. The simulation parameters are shown in table (2.2).

It is well known that the analytical solution for the torque free motion of rigid body can be expressed in terms of Jacobian elliptic functions [69] [40].

Given the initial angular velocity (at time t=0) of the system, the angular

Parameters	
Mass moment of inertia	$(J_{x'x'}, J_{y'y'}, J_{z'z'}) = (400, 307.808385, 200)\ kg - m^2$
Initial conditions	Euler parameters $\mathbf{e} = (1, 0, 0, 0)$ $\mathbf{h}^{'} = (346.4101616, 0, -200)\ kg - m^2 rad/s$

Table 2.2: Simulation parameters

momenta at any time $t > 0$ can be shown to be [69]

$$\omega_{x'}(t) = \omega_{mx'} \mathcal{D}n(\mathcal{T}, k) \tag{2.96}$$

$$\omega_{y'}(t) = \omega_{my'} \mathcal{S}n(\mathcal{T}, k) \tag{2.97}$$

$$\omega_{z'}(t) = -\omega_{mz'} \mathcal{C}n(\mathcal{T}, k) \tag{2.98}$$

where the terms used in the above equations are defined as

- $$\omega_{mx'} = \sqrt{\frac{h'^2 - 2\,T J_{z'z'}}{J_{x'x'}(J_{x'x'} - J_{z'z'})}} \tag{2.99}$$

  $$\omega_{my'} = \sqrt{\frac{h'^2 - 2\,T J_{z'z'}}{J_{y'y'}(J_{y'y'} - J_{z'z'})}} \tag{2.100}$$

  $$\omega_{mz'} = \sqrt{\frac{2\,T J_{x'x'} - h'^2}{J_{z'z'}(J_{x'x'} - J_{z'z'})}} \tag{2.101}$$

- $h^{'} = ||\mathbf{h}^{'}|| = ||\mathbf{J}^{'}\boldsymbol{\omega}^{'}||$ represents the constant angular momentum. $||\ ||$ is the standard Euclidean norm

- $T = {\boldsymbol{\omega}'}^T \mathbf{J}' \boldsymbol{\omega}'$ is the constant kinetic energy of the rigid body

- Let Γ and Γ' be defined as

$$\Gamma = \sqrt{\frac{\left({h'}^2 - 2\,T\,J_{z'z'}\right)\left(J_{x'x'} - J_{y'y'}\right)}{J_{x'x'}J_{y'y'}J_{z'z'}}} \tag{2.102}$$

$$\Gamma' = \sqrt{\frac{\left(2\,T\,J_{x'x'} - {h'}^2\right)\left(J_{y'y'} - J_{z'z'}\right)}{J_{x'x'}J_{y'y'}J_{z'z'}}} \tag{2.103}$$

The elliptic modulus ‘ k ’ in equations (2.96) through (2.98) is defined as

$$k = \frac{\Gamma'}{\Gamma} \tag{2.104}$$

- $\mathcal{T}$ is defined as

$$\mathcal{T} = \Gamma\, t \tag{2.105}$$

- $\mathcal{S}n$, $\mathcal{C}n$ and $\mathcal{D}n$ are Jacobian elliptic functions. Note that

$$\mathcal{S}n^2(\mathcal{T},k) + \mathcal{C}n^2(\mathcal{T},k) = 1 \tag{2.106}$$

$$\mathcal{D}n^2(\mathcal{T},k) + k^2\mathcal{S}n^2(\mathcal{T},k) = 1 \tag{2.107}$$

For the parameters defined in the table (2.2), the amplitudes of the angular momenta and the elliptic modulus expressed in equations (2.96 - 2.98) can be computed to be

- $\left[h_{mx'}, h_{my'}, h_{mz'}\right] = [346.4102, 365.447, 200]$ kg-m^2 rad/s

- $k = 0.882948$

The period parameter $K(k)$ can be computed as

$$K(k) = \int_0^{\frac{\pi}{2}} \frac{1}{\sqrt{\left(1 - k^2 \sin^2\theta\right)}}\, d\theta \tag{2.108}$$

$$= 2.213195 \tag{2.109}$$

The period of $\mathcal{S}n(\mathcal{T}, k)$ and $\mathcal{C}n(\mathcal{T}, k)$ is

$$\left(\frac{4\,K}{\Gamma}\right) = 18.6786\, sec \tag{2.110}$$

and that of $\mathcal{D}n(\mathcal{T}, k)$ is

$$\left(\frac{2\,K}{\Gamma}\right) = 9.3393\, sec. \tag{2.111}$$

Also the minimum value of $h_{x'}$ can be computed to be

$$min \left\{h_x^{'}\right\} = h_{mx'} \left(1 - k^2\right)^{\frac{1}{2}} \tag{2.112}$$

$$= 162.6296\, \text{kg}\, m^2 \text{ rad/s} \tag{2.113}$$

The torque-free motion of a rigid body is calculated numerically using a fourth order Runge Kutta integrator with a fixed time step of 0.0625 sec. Table (2.3) shows a comparison between numerical and exact values. It can be seen that the simulation results are in good agreement with the derived analytical results.

	exact	numerical
$h_{mx'}$	$346.4102 \quad kg - m^2 rad/s$	$346.38 \quad kg - m^2 rad/s$
$h_{my'}$	$365.447 \quad kg - m^2 rad/s$	$365.44 \quad kg - m^2 rad/s$
$h_{mz'}$	$200.0 \quad kg - m^2 rad/s$	$199.975 \quad kg - m^2 rad/s$
Period of $h_{x'}$	9.3393 sec	9.35 sec
Period of $h_{y'}$	18.6786 sec	18.68 sec
Period of $h_{z'}$	18.6786 sec	18.68 sec
Minimum value of h_x'	162.6296 kg m^2 rad/s	162.6342 kg m^2 rad/s

Table 2.3: Comparison between experimental and simulation results

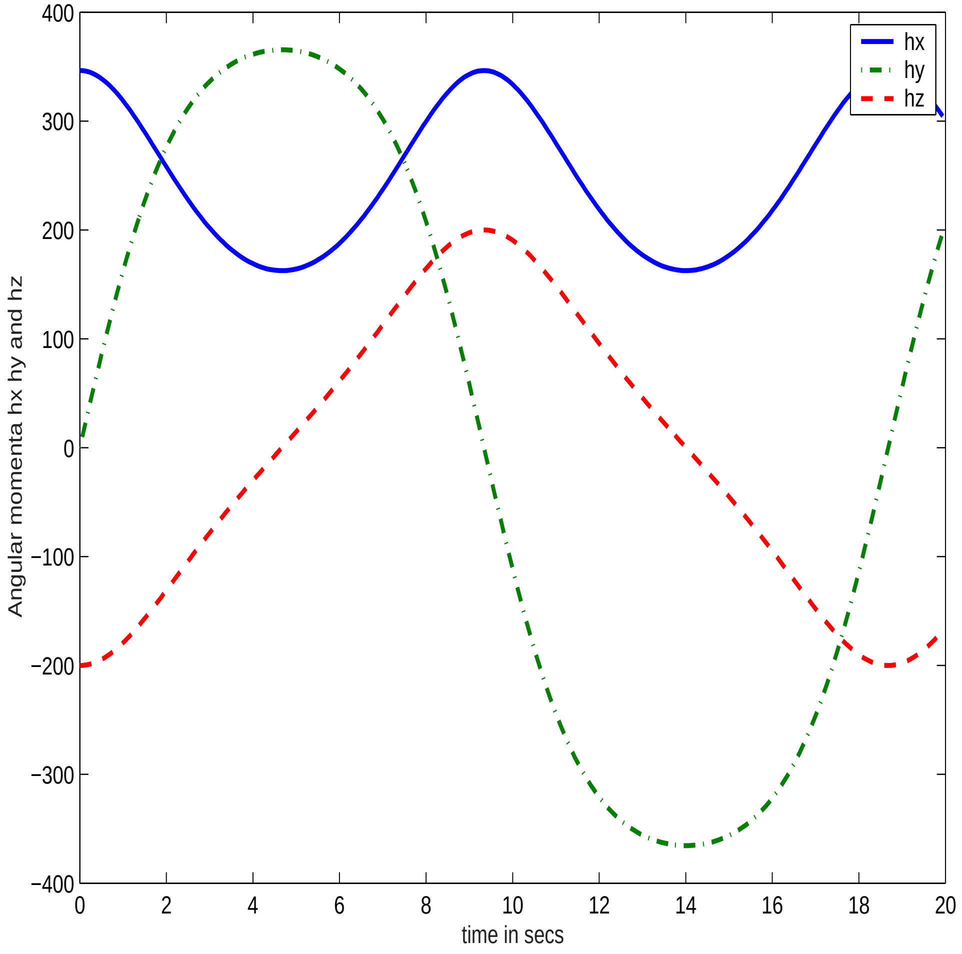

Figure 2.7: Angular momenta versus time

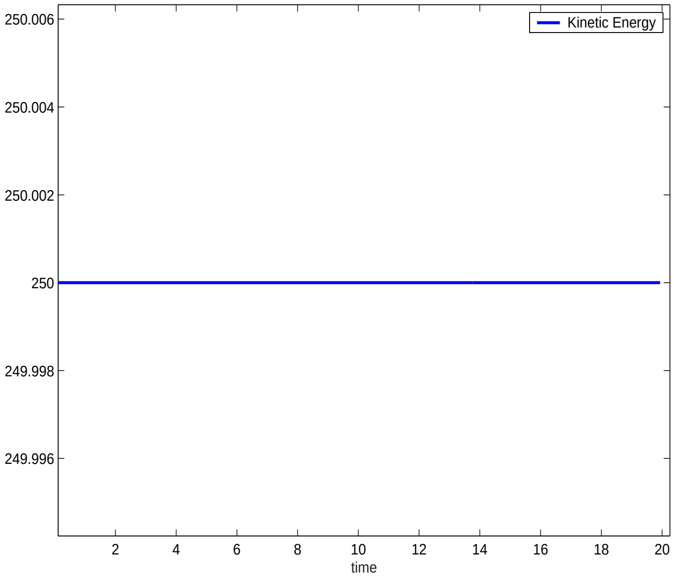

Figure 2.8: Total energy versus time

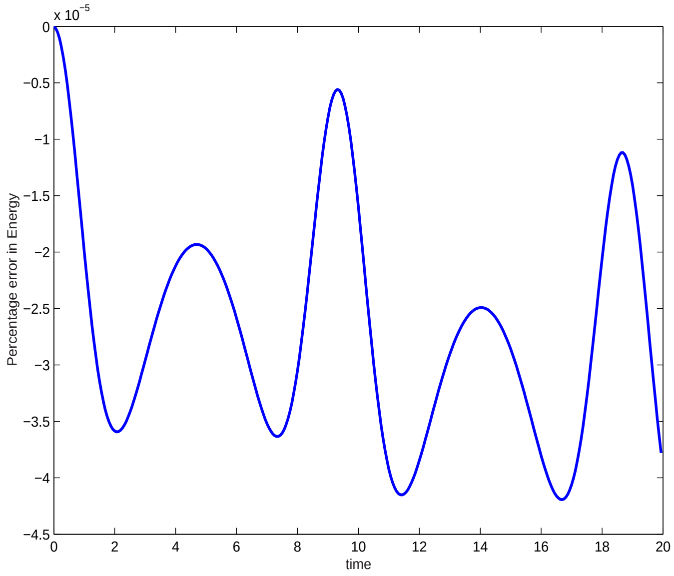

Figure 2.9: Percentage error in total energy versus time

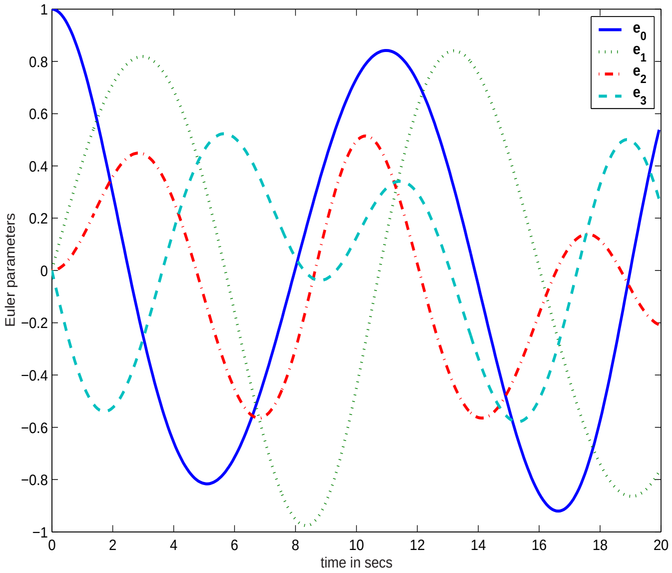

Figure 2.10: Euler parameters versus time

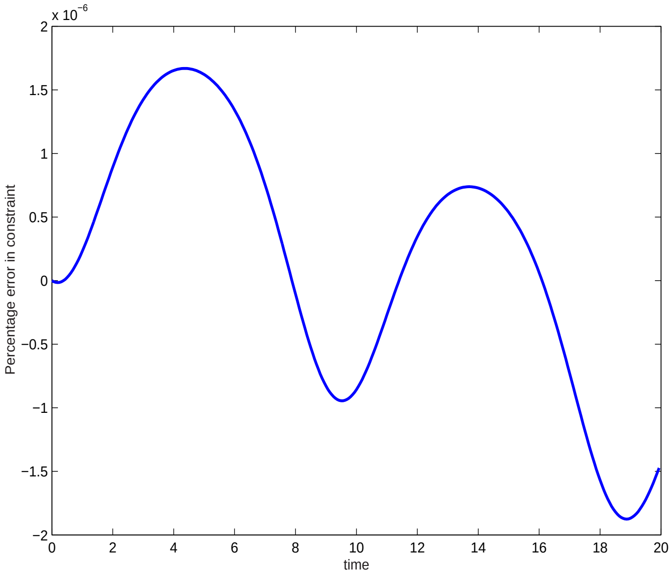

Figure 2.11: Percentage error in euler parameter constraint versus time

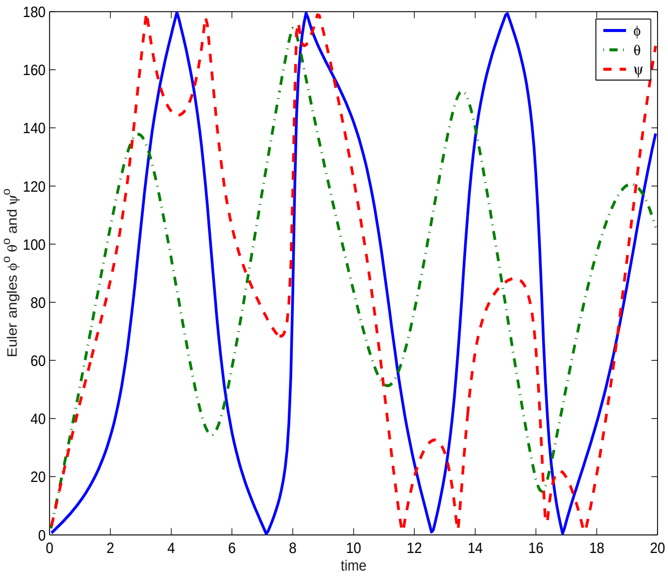

Figure 2.12: Euler angles versus time

2.7.4 Motion of a spinning top in a gravitational field

In this example numerical simulation of the motion of a symmetrical top spinning in a uniform gravitational field is performed using the formulation derived earlier in this chapter. Specifically, this problem is presented as a numerical example by Simo and Wong [66].

This is a classical problem, a description of which can be found in many standard advanced dynamics texts [25] [24] [23] [3]. Consider a symmetrical top of total weight ‘ W ’ rotating about its apex ‘ O ’ on a horizontal plane. Let $\boldsymbol{a}$ represent the global frame and $\boldsymbol{a}^{'}$ be a body fixed frame with its origin located at the center of mass G of the top as shown in figure (2.13).

The angular velocity of the top represented in the frame of the body is $\boldsymbol{\omega}^{'}$. Let ‘ l ’ be the distance to the center of mass from ‘ O ’ along axis $\boldsymbol{z}^{'}$. The distributed mass moment of inertia of the top about the center of mass is $\boldsymbol{J}^{'}$. The apex does

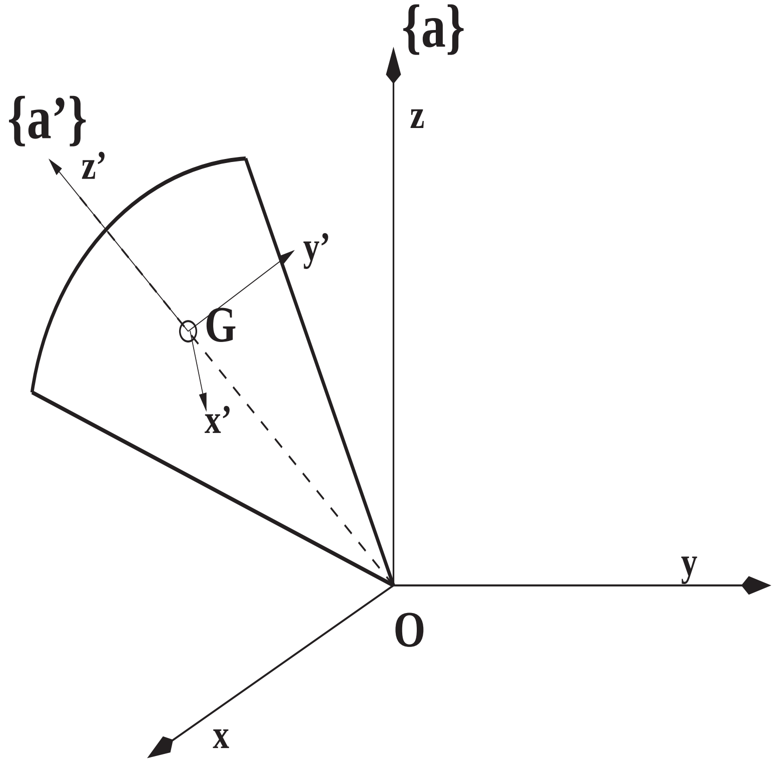

Figure 2.13: Spinning top

not translate and is in continuous contact with the horizontal plane. The kinetic and potential energies of the system can be written as

$$T = \frac{1}{2}\boldsymbol{\omega}'^{T}\boldsymbol{J}'\,\boldsymbol{\omega}' \tag{2.114}$$

$$V = W\,Z_g \tag{2.115}$$

In the equation (2.115) ‘ W ’ is the weight of the top and Z_g is the Z coordinate of the point ‘ g ’ in the global frame. The body fixed frame is related to the global frame by a rotation matrix. Specifically,

$$\boldsymbol{a} = \boldsymbol{R}\boldsymbol{a}' \tag{2.116}$$

Hamilton's equations for this system take the form of a set of first order differential equations (2.70) and (2.71). These equations are integrated in time using a fourth order Runge-Kutta integration scheme with a fixed time step of 10^{-3} seconds. For a top with kinetic energy $\gg$ potential energy, an approximate relation for the angular frequency of nutation and precession are [24].

Parameters	
Weight of the top	$W = 20$ kg m/s^2
Mass moment of inertia	$J_{x'x'} = 5,\ J_{y'y'} = 5,\ J_{z'z'} = 1\ \ kg - m^2$
Initial euler parameters	$e_0 = \cos(0.15),\ e_1 = \sin(0.15),\ e_3 = 0,\ e_4 = 0$
Initial angular momenta	$h_1 = 0,\ h_2 = 0,\ h_3 = 50\, kg - m^2 rad/s$

Table 2.4: Simulation parameters and initial conditions

$$\omega_n = \frac{J_{z'z'}}{J_{x'x'}}\,\omega_z' \tag{2.117}$$

$$\omega_p = \frac{W\,l}{J_{z'z'}\omega_z'} \tag{2.118}$$

Table (2.5) shows a comparison of analytical and numerical values of nutation and precession frequencies.

	analytical	simulation
Nutation frequency	10 rad/sec	9.24 rad/sec
Precession frequency	0.40 rad/sec	0.4136 rad/sec

Table 2.5: Comparison between analytical and simulation results

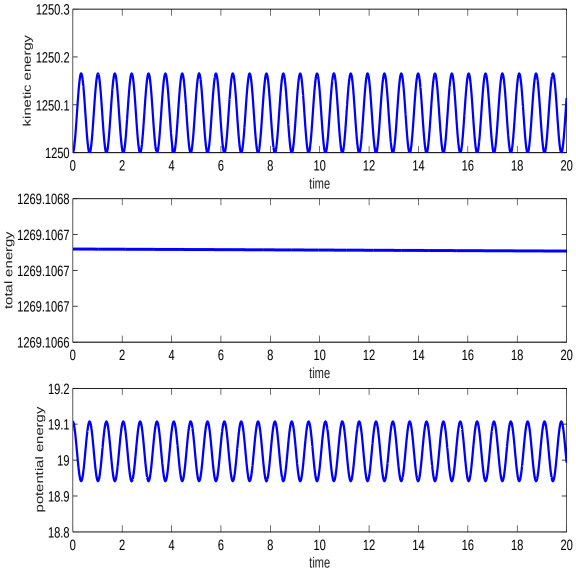

Figure 2.14: Energy versus time

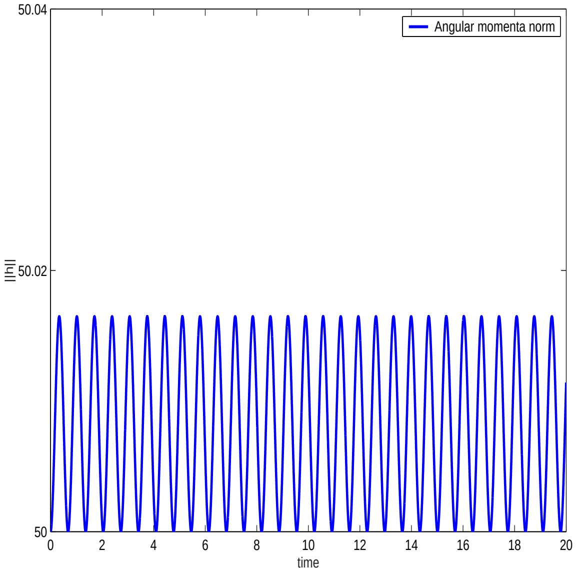

Figure 2.15: Norm of the angular momenta versus time

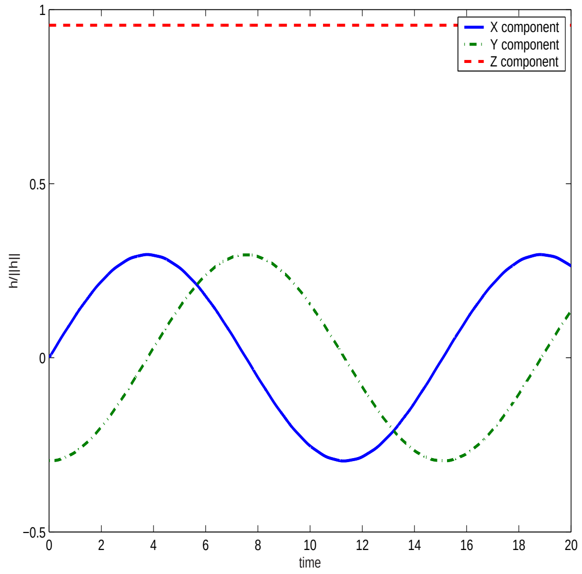

Figure 2.16: Spatial components of the angular momentum

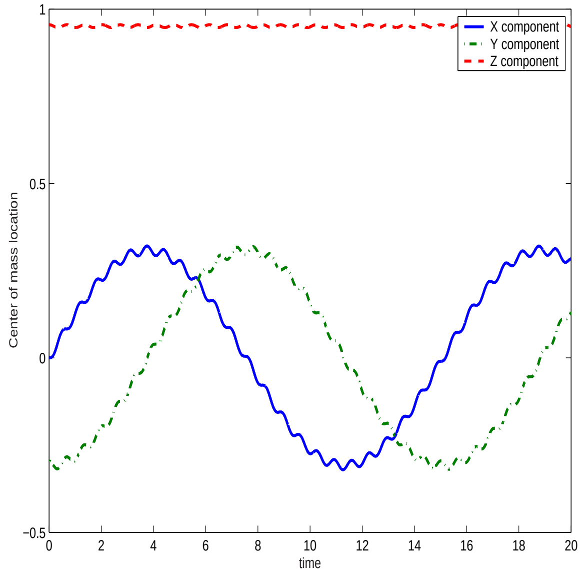

Figure 2.17: Center of mass location

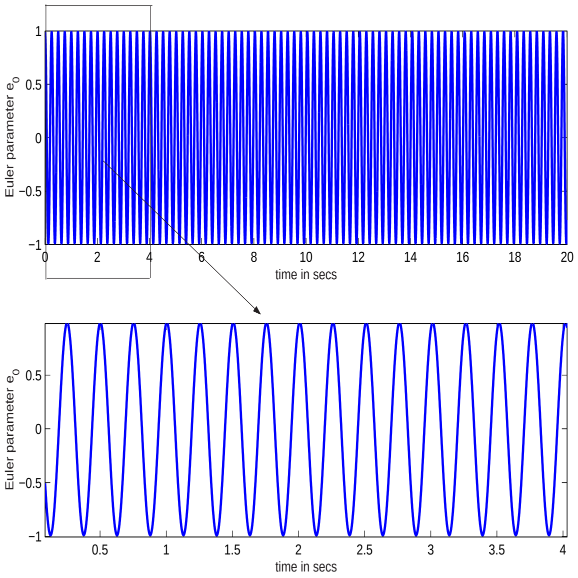

Figure 2.18: Euler parameter e_0 versus time

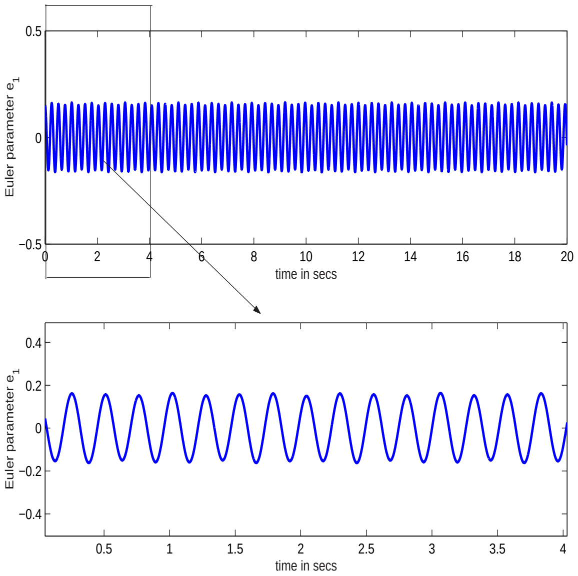

Figure 2.19: Euler parameter e_1 versus time

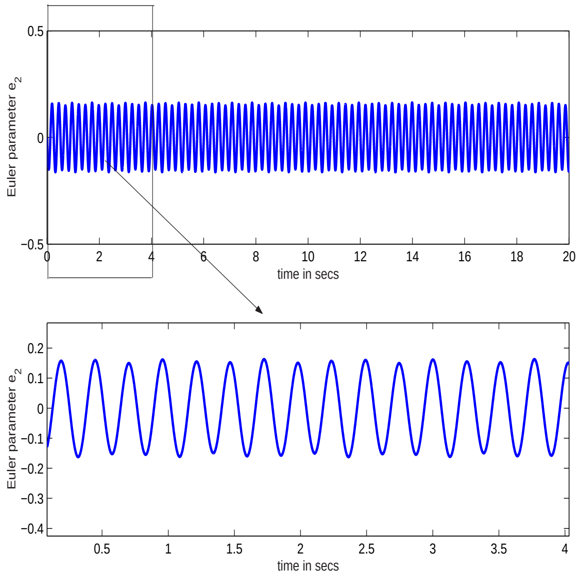

Figure 2.20: Euler parameter e_2 versus time

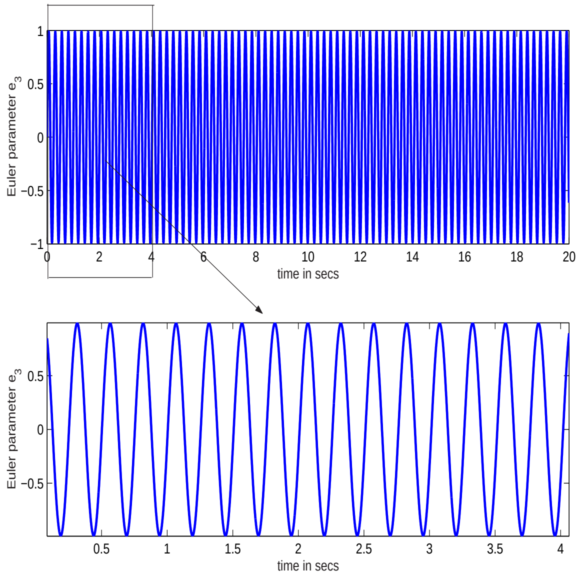

Figure 2.21: Euler parameter e_3 versus time

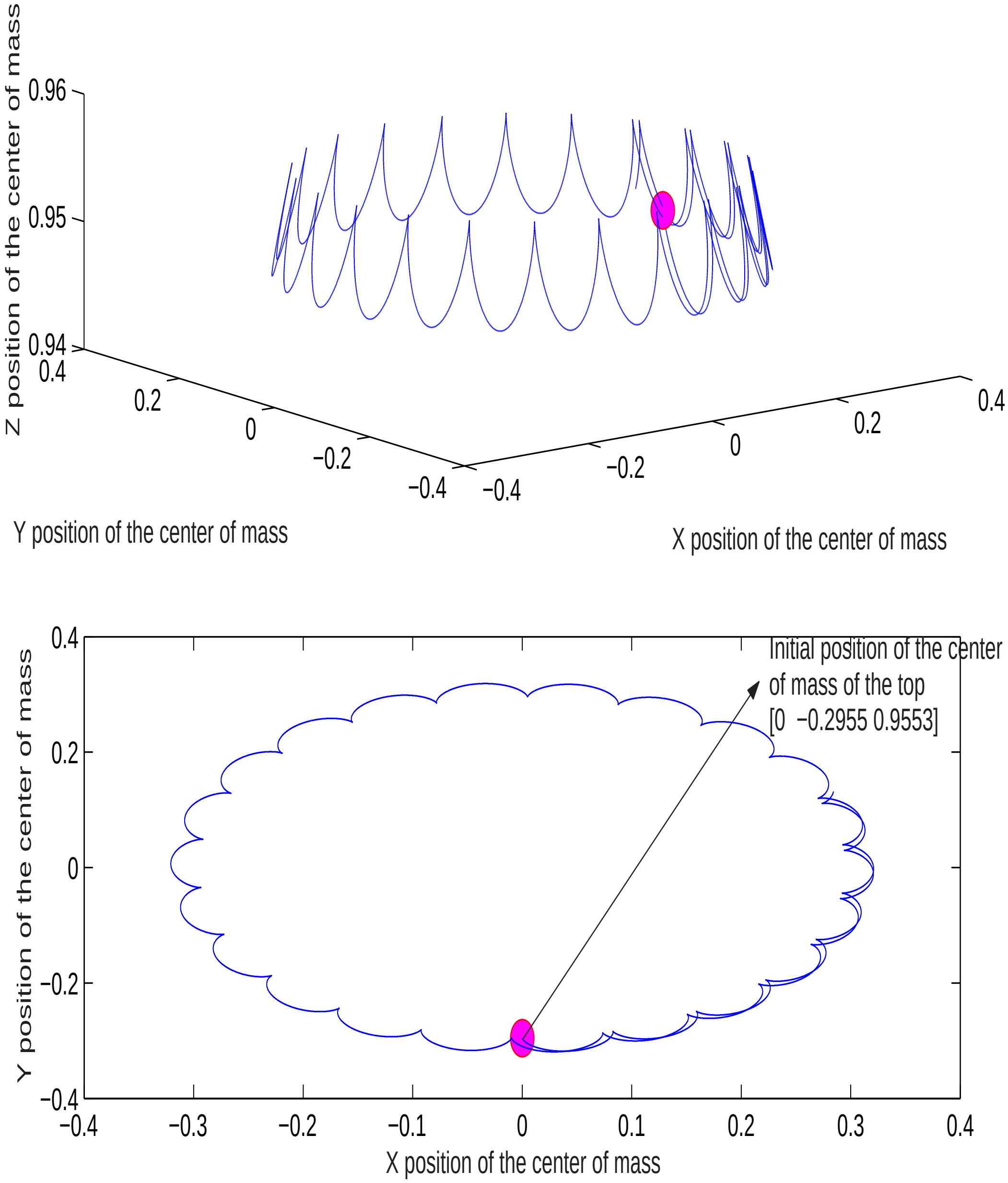

Figure 2.22: Motion of the center of mass of the top

2.8 Conclusions

In this chapter, a robust Hamiltonian formulation to model rigid body dynamics is developed. The present formulation makes use of Euler parameters to parameterize rotation, eliminating singularity problems associated with many three parameter representations of rotation. Unlike previous work [40], [52], [51] the dynamic equations of rotational motion are devoid of any explicit Lagrange multiplier used to enforce the Euler parameter constraint. This results in a set of first order nonlinear ordinary differential equations which can be integrated using a standard integration routine. The results from the numerical simulations show good agreement with analytical results.

Chapter 3

A general hybrid particle-finite element modeling methodology for hypervelocity impact

3.1 Introduction

The drawbacks of a pure particle or a pure mesh based method to model hypervelocity impact have been described in chapter (1). In this chapter a hybrid model, which combines the strengths of both particle and standard Lagrangian finite elements to model hypervelocity impact of orbital debris on space structures is developed.

Most particle methods including smooth particle hydrodynamics(SPH) and the particle in cell method (PIC) treat particles as moving interpolation points. Fahrenthold and Koo [17] proposed an alternative particle model based on Hamilton's equations. The continuum is discretized into physical particles which translate, deform and interact with each other thermo-mechanically. Fahrenthold and

Horban [20] extended this work by coupling the aforementioned particle model with Lagrangian finite elements. This provided the ability to model strength effects while retaining all the advantages of a particle based model. Further the model was enhanced to capture plasticity and continuum damage and fragmentation behavior commonly seen in hypervelocity impact. A thermodynamically consistent continuum damage and fragmentation model [15] was developed for this purpose. The formulation was implemented in a three dimensional computer code. A disadvantage of the above formulation is the use of a penalty method to model contact-impact. Recognizing this fact Fahrenthold and Koo [18] developed a hybrid particle finite element model, using a kernel function for density interpolation. An explicit distinction is made between nearest and non-nearest neighbors. This distinction is reflected in the use of two different kernels to compute density. The continuum is discretized into particles and elements simultaneously with all the mass lumped into particles. This results in an inconsistent mass matrix [46]. Fahrenthold and Horban [19] extended the above formulation by incorporating plasticity, continuum damage and a fragmentation model.

3.2 Overview of the modeling methodology

The current work generalizes the hybrid particle-finite element work of Fahrenthold and Horban [19]. The continuum is discretized simultaneously but not redundantly into particles and finite elements. Particles are used to model inertia effects and thermo-mechanical volumetric response. Elements are used to model inter-particle tensile forces and elastic-plastic shear. Thus particles and elements are used to model different physical effects in the same continuum. The particles can translate and rotate in three dimensional space and interact with each other thermo-mechanically. The three dimensional rotational motion of the particles are described in terms of the Euler parameters. The use of ellipsoidal particles gives the modeling methodology a unique feature, modeling geometries with a high aspect ratio. In addition, this offers a possibility of reducing computer resource requirements in some hypervelocity simulations. A kernel function is used for density interpolation, eliminating the need to explicitly impose any mass conservation properties on the kernel. The chosen kernel function is singular and satisfies exact Lagrangian kinematics. Unlike previous work [20] the density kernel is a function of the particle separation distance and the rotational parameters. Rotational dynamics developed in chapter (2) are used to model three dimensional rotational dynamics of the particles. The large deformation finite element kinematics used by Fahrenthold and Horban [20] are extended to include hexahedra with arbitrary aspect ratios.

The model uses the plasticity formulation developed by Fahrenthold and Horban [15]. Damage to the continuum is modeled with the introduction of two scalar damage variables. Standard to many hydrocodes, the model introduces artificial viscosity and artificial heat flux to model shocks and to damp the translational mode of the particles.

The model development presented here adopts an energy based approach. The classical approach of using a weighted residual scheme is abandoned in favor of a system dynamics method. Hamiltonian mechanics forms the basis for model development. The Hamiltonian for the thermo-mechanical system can be obtained from the kinetic and internal energy expressions for the system. The Hamiltonian of the system is a function of the generalized coordinates and the generalized momenta, commonly referred to as states. Simple differentiation operations of the Hamiltonian function, with respect to the state variables, yield the governing equations for the dynamics of the system. The rate equations for the internal state variables result in a set of nonholonomic constraints. Lagrange multipliers (determined in closed form) are used to embed these constraints, resulting in a set of first order differential equations. Once a set of initial conditions are specified, these equations can be integrated numerically using a standard integration scheme.

The rest of the chapter is organized as follows. First the particle and element kinematics are established, following which the interpolation function for density is developed. Expressions for kinetic and internal energy are developed subsequently. The kinetic and internal energy define the Hamiltonian for the thermo-mechanical system. Conservative forces are obtained by differentiating the Hamiltonian with respect to the generalized displacements. A plasticity model is developed which introduces the plastic deformation as a state variable. Damage variables are introduced to model loss of strength of the continuum. Artificial viscosity and artificial heat flux expressions are developed to model shocks. The coupling of mechanical and thermal domains is achieved with the introduction of entropy as a state variable. Using the aforementioned development the state equations are derived, which are a set of first order nonlinear ordinary differential equations. Other computational issues such as neighbor finding and time step calculations are discussed. Initial validation of the model is performed by simulating a one dimensional wall shock problem. Comparison of numerical and exact solutions are presented. The validated model is used to solve more complex impact problems. A discussion of results from these simulations concludes the chapter.

3.3 Kinematics

3.3.1 Particle kinematics

The system being modeled here is discretized into a set of ‘ n ’ non-deforming ellipsoidal particles, each with a fixed mass $m^{(i)}$, $(i = 1, 2, 3, \ldots, n)$ and a distributed mass moment of inertia expressed in the body fixed frame of $\mathbf{J}'^{(i)}$. The particles translate and rotate in three dimensional space and interact with each other thermo-mechanically. The translational velocity of the center of mass of a particle is $\dot{\mathbf{c}}^{(i)}$ and the angular velocity of a particle represented in the frame of the particle is $\boldsymbol{\omega}'^{(i)}$. The total particle entropy is $S^{(i)}$.

Particles are used to model contact-impact and volumetric effects while Lagrangian finite elements are used to model tension, elastic shear forces and plasticity effects. Elements are formed by connecting the nodal coordinates of the particles. Though particles and elements are used simultaneously, they are used to model different physical effects in the same continuum.

3.3.2 Element kinematics

The center of mass coordinates of the particles serve as nodes of the finite elements. In three dimensional simulations, the particles are packed according to a body centered cubic packing scheme. The eight corner nodes define hexahedra. The body centered node is associated with six sets of four particles (representing the faces of the hexahedra) to form sub-elements. The Jacobians of the sub-elements are used to determine inter-particle tensile forces, while shear forces are calculated using the hexahedra. The deviatoric strain tensor $\bar{\mathbf{E}}^{(j)}$ of an element 'j' is defined as

$$\begin{aligned} \bar{\mathbf{E}}^{(j)} &= \frac{1}{2}\left\{\bar{\mathbf{C}}^{(j)} - \mathbf{I}\right\} \qquad \text{where} && (3.1)\\ \bar{\mathbf{C}}^{(j)} &= {J^{(j)}}^{-\frac{2}{3}}\mathbf{C}^{(j)} \qquad \text{and} && (3.2)\\ J^{(j)} &= \left\{\det\left(\mathbf{C}^{(j)}\right)\right\}^{\frac{1}{2}} && (3.3) \end{aligned}$$

‘ $J^{(j)}$ ’ is the Jacobian of the hexahedron, ‘ $\mathbf{C}^{(j)}$ ’ is the right Cauchy-Green strain tensor and ‘ $\mathbf{I}$ ’ is the second order identity tensor.

Although the current model uses body centered packing scheme, the modeling framework is general enough to allow alternate packing schemes and finite element interpolation functions.

3.3.3 Density Interpolation

The mass density of a particle is obtained by using a density interpolation of the form

$$\rho^{(i)} = {\rho_0}^{(i)} + \hat{\rho}^{(i)} \tag{3.4}$$

where ‘ ${\rho_0}^{(i)}$ ’ is the constant reference density of the particle and ‘ $\hat{\rho}^{(i)}$ ’ is the density contribution from all other particles

$$\hat{\rho}^{(i)} = \sum_{\substack{j=1 \\ j\neq i}}^{n} {\rho_0}^{(j)} W^{(i,j)} \tag{3.5}$$

with ‘ n ’ the total number of particles in the system.

Kernel function

The kernel function $W^{(i,j)}$ in equation (3.5) is chosen to be a positive semi-definite function such that it models the exact Lagrangian kinematics of the particles under uniform compression. This interpolation scheme for the density ensures that the density of an isolated particle cannot drop below its reference density ‘ ρ_0 ’.

$$W^{(i,j)} = \left\{ \left(\frac{1}{\zeta(i,j)} \right)^3 - 1 \right\} H \left[\alpha \left(\frac{\rho_0^{(i)}}{\rho^{(i)}} \right)^{\frac{1}{3}} - \zeta(i,j) \right] \tag{3.6}$$

where $H[x-\delta]$ represents the standard heaviside function defined as

$$\begin{aligned} H[x-\delta] &= 1 \qquad \text{if } x \geq \delta \text{ and} \\ &= 0 \qquad \text{otherwise} \end{aligned} \tag{3.7}$$

' α ' is a scalar constant which depends on the dimension of the problem and the packing scheme chosen. For three dimensional problems with body centered cubic packing, $\alpha = \frac{1}{2}\left(1+\frac{2\sqrt{3}}{3}\right)$. Note that the kernel function defined by equation (3.6) is implicit, in that the argument of the heaviside function in equation (3.6) depends on the density ratio. This dependence mimics the true physical behavior in the sense that a particle which is highly compressed due to its immediate neighbors is partially screened from interacting with other particles. $\zeta(i,j)$ in equation (3.6) is defined as follows.

Let the effective interaction distances along the three principal axes be defined as

$$h_{eff1} = 2\,\beta^{(j)}\,h_1^{(j)} \tag{3.8}$$

$$h_{eff2} = 2\,\beta^{(j)}\,h_2^{(j)} \tag{3.9}$$

$$h_{eff3} = 2\,\beta^{(j)}\,h_3^{(j)} \tag{3.10}$$

where $h_1^{(j)}$, $h_2^{(j)}$ and $h_3^{(j)}$ are the semi-axes lengths of the ellipsoid centered at $\mathbf{c}^{(j)}$. $\beta^{(j)}$ is a constant packing factor. Let $\mathbf{A}^{(j)}$ be a 3×3 diagonal matrix defined as

$$\mathbf{A}^{(j)} = \begin{bmatrix} h_{eff1}^2 & 0 & 0 \\ 0 & h_{eff2}^2 & 0 \\ 0 & 0 & h_{eff3}^2 \end{bmatrix}^{-1} \tag{3.11}$$

Let $\mathbf{R}^{(j)}$ be the rotation matrix that transforms global components of a vector into components in the frame of the particle 'j'. As discussed in chapter (2), the elements of the rotation matrix $\mathbf{R}^{(j)}$ can be represented in terms of the Euler parameters of the j^{th} particle.

$$\mathbf{R}^{(j)} = \begin{bmatrix} {e_0^{(j)}}^2 + {e_1^{(j)}}^2 - {e_2^{(j)}}^2 - {e_3^{(j)}}^2 & 2(e_1^{(j)} e_2^{(j)} + e_0^{(j)} e_3^{(j)}) & 2(e_1^{(j)} e_3^{(j)} - e_0^{(j)} e_2^{(j)}) \\ 2(e_1^{(j)} e_2^{(j)} - e_0^{(j)} e_3^{(j)}) & {e_0^{(j)}}^2 - {e_1^{(j)}}^2 + {e_2^{(j)}}^2 - {e_3^{(j)}}^2 & 2(e_2^{(j)} e_3^{(j)} + e_0^{(j)} e_1^{(j)}) \\ 2(e_1^{(j)} e_3^{(j)} + e_0^{(j)} e_2^{(j)}) & 2(e_2^{(j)} e_3^{(j)} - e_0^{(j)} e_1^{(j)}) & {e_0^{(j)}}^2 - {e_1^{(j)}}^2 - {e_2^{(j)}}^2 + {e_3^{(j)}}^2 \end{bmatrix} \tag{3.12}$$

$\zeta(i,j)$ is can then be defined by the following equation

$$\zeta^{(i,j)} = \left\{ \left(\mathbf{c}^{(i)} - \mathbf{c}^{(j)} \right)^T {\mathbf{R}^{(j)}}^T \mathbf{A}^{(j)} \mathbf{R}^{(j)} \left(\mathbf{c}^{(i)} - \mathbf{c}^{(j)} \right) \right\}^{\frac{1}{2}} \tag{3.13}$$

Unlike density kernels used in smooth particle hydrodynamics [47], the density interpolation function described here is non-dimensional and has compact support. Fahrenthold and Koo [18] and Fahrenthold and Horban [20] distinguish between the density contributions from nearest and non-nearest neighbors by using two different non-dimensional kernels. A singular kernel was used for density contributions from nearest neighbors. The form of this kernel function was chosen such that it modeled exact Lagrangian kinematics under uniform compression of the particles. A second density kernel was used for density contributions from non-nearest neighbors. In chapter (4) advanced simulation and validation results based on these kernels is presented.

In the present formulation no explicit distinction is made between nearest and non-nearest neighbors. One singular non-dimensional kernel with adaptive support given by equation (3.6) is used for all the particles.

3.4 Kinetic Energy

The kinetic co-energy T^* of the system is given by

$$T^* = \sum_{i=1}^{n} T^{*(i)} \tag{3.14}$$

where

$$T^{*(i)} = \frac{1}{2} m^{(i)} \dot{\mathbf{c}}^{(i)T} \dot{\mathbf{c}}^{(i)} + \frac{1}{2} \boldsymbol{\omega}'^{(i)T} \mathbf{J}'^{(i)} \boldsymbol{\omega}'^{(i)} \tag{3.15}$$

The linear and angular momenta can be defined as

$$\mathbf{p}^{(i)} = \frac{\partial T^*}{\partial \mathbf{c}^{(i)}} = m^{(i)} \dot{\mathbf{c}}^{(i)} \tag{3.16}$$

$$\mathbf{h}'^{(i)} = \frac{\partial T^*}{\partial \boldsymbol{\omega}'^{(i)}} = \mathbf{J}'^{(i)} \boldsymbol{\omega}'^{(i)} \tag{3.17}$$

A standard Legendre transformation of equation (3.14) results in an expression for kinetic energy which depends on the center of mass momenta $\mathbf{p}^{(i)}$ and the distributed momenta $\mathbf{h}'^{(i)}$

$$T = \left\{ \sum_{i=1}^{n} \left[\mathbf{p}^{(i)} \cdot \dot{\mathbf{c}}^{(i)} + \mathbf{h}'^{(i)} \cdot \boldsymbol{\omega}'^{(i)} \right] \right\} - T^* \qquad \text{or} \tag{3.18}$$

$$T = \frac{1}{2} \sum_{i=1}^{n} \left[\mathbf{p}^{(i)T} m^{(i)-1} \mathbf{p}^{(i)} + \mathbf{h}'^{(i)T} \mathbf{J}'^{(i)-T} \mathbf{h}'^{(i)} \right] \tag{3.19}$$

Using equation (2.45), equation (3.19) can be rewritten as

$$T = \sum_{i=1}^{n} \left[\frac{1}{2} \, \mathbf{p}^{(i)^T} m^{(i)^{-1}} \mathbf{p}^{(i)} + \frac{1}{8} \, \mathbf{h_e}^{(i)T} \, \mathbf{G}^{(i)T} \, \mathbf{J}^{(i)'^{-T}} \, \mathbf{G}^{(i)} \, \mathbf{h_e}^{(i)} \right] \tag{3.20}$$

3.5 Internal Energy

The appropriate stored potential function for the thermo-mechanical system considered here is the internal energy. The internal energy depends in general on the kinematics and the chosen equation of state.

$$U = \int_V \rho \, \mathbf{u} \left(\rho, s, \mathbf{c}, d, D, \mathbf{E}^e \right) \, dV \tag{3.21}$$

where ‘ ρ ’ and ‘ s ’ are the density and the entropy per unit mass previously defined, computed at the center of mass ‘ $\mathbf{c}$ ’ of the particle. The scalars ‘ D ’ and ‘ d ’ represent volumetric and deviatoric damage variables. The exact evaluation of the integral in equation (3.21) is in general not possible. In a later part of this section, a discrete form of the equation (3.21) is developed.

The internal energy can be decomposed into two primary parts.

$$U = U_{\text{particles}} + U_{\text{elements}} \tag{3.22}$$

The energy stored in the particles depends on the chosen equation of state and can be written in functional form as

$$U_{\text{particles}} = \sum_{i=1}^{n} m^{(i)} u^{(i)} \left(\rho^{(i)}, s^{(i)} \right) \tag{3.23}$$

where ‘ u ’ is the internal energy per unit mass and ‘ s ’ is the entropy per unit mass. The present formulation is general enough to incorporate various equations of state.

U_{elements} can be written as

$$\begin{aligned} U_{\text{elements}} &= \left\{ \sum_{j=1}^{ne} \sum_{k=1}^{ns} \frac{1}{2} \left(1 - D^{(j)}\right) V_0^{(j,k)} \kappa^{(j)} \left(J^{(j,k)} - 1\right)^2 \right\} H\left[J^{(j,k)} - 1\right] \\ &+ \left\{ \sum_{j=1}^{ne} \left(1 - d^{(j)}\right) V_0^{(j)} \mu^{(j)} \mathbf{E}^{e(j)} : \mathbf{E}^{e(j)} \right\} \end{aligned} \tag{3.24}$$

where 'ne' is the number of elements, 'ns' is the number of sub-elements per element, '$\kappa^{(j)}$' is the element bulk modulus, '$J^{(j)}$' and '$J^{(j,k)}$' are the element and sub-element Jacobians and '$V_0^{(j)}$' and '$V_0^{(j,k)}$' are the reference volumes of the element and the subelements. Also '$\mu^{(j)}$' is the element shear modulus and ':' is a double contraction operator. The elements are used to model inter-particle tensile and elastic shear forces. Although the present model assumes a linear elastic response, the modelling frame work is general enough to accommodate more complex non-linear elastic material behavior.

'$D^{(j)}$' and '$d^{(j)}$' are normal and deviatoric scalar damage variables respectively, associated with element 'j'. The damage variables vary from zero to one, with zero representing an intact element and one representing a complete failure of the element. The evolution equations for damage will be discussed in section (3.8).

The element Jacobian and the elastic strain tensor are a function of the nodal coordinates of the finite element. The nodal coordinates are the center of mass coordinates of the particles. Hence

$$J^{(j,k)} = J^{(j,k)}(\mathbf{c}^{(i)}) \tag{3.25}$$

$$\mathbf{E}^{e(j)} = \mathbf{E}^{e(j)}(\mathbf{c}^{(i)}, \mathbf{E}^{p(j)}) \tag{3.26}$$

3.6 Conservative forces

The conservative forces $\mathbf{g}^{(i)}$ and $\boldsymbol{\tau}^{(i)}$ are obtained by differentiating the stored energy with respect to the generalized displacements. Figure (3.1) shows the force interaction between ellipsoidal particles.

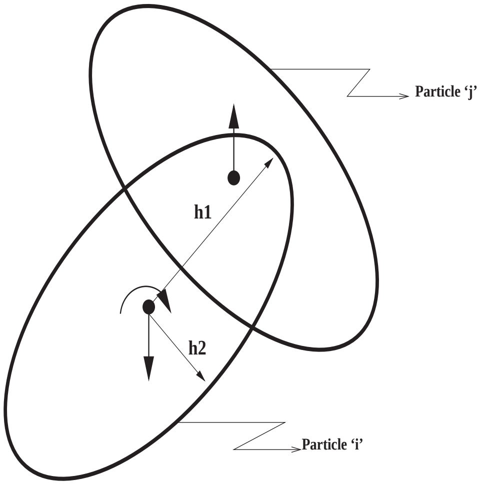

Figure 3.1: Generalized forces between particles

$$\mathbf{g}^{(i)} = \frac{\partial U}{\partial \mathbf{c}^{(i)}} \tag{3.27}$$

$$\boldsymbol{\tau}^{(i)} = \frac{\partial U}{\partial \mathbf{e}^{(i)}} \tag{3.28}$$

which can be computed as

$$\begin{aligned}\mathbf{g}^{(i)} \quad = \quad & \underbrace{\sum_{\substack{j=1\\ j\neq i}}^{n} \left[\frac{{\rho_0}^{(i)} m^{(j)} P^{(j)}}{{\rho^{(j)}}^2} + \frac{{\rho_0}^{(j)} m^{(i)} P^{(i)}}{{\rho^{(i)}}^2} \right] \frac{\partial W^{(i,j)}}{\partial \mathbf{c}^{(i)}}}_{particles} \\ & \underbrace{+ \sum_{j=1}^{ne} \kappa^{(j)} {V_0}^{(j)} \left(J^{(j)} - 1 \right) H \left[J^{(j)} - 1 \right] \frac{\partial J^{(j)}}{\partial \mathbf{c}^{(i)}}}_{elements}\end{aligned}$$

$$\underbrace{+\sum_{j=1}^{ne} 2\mu^{(j)} {V_0}^{(j)} \mathbf{E}^{(j)} : \frac{\partial \mathbf{E}^{(j)}}{\partial \mathbf{c}^{(i)}}}_{elements} \tag{3.29}$$

$$\boldsymbol{\tau}^{(i)} = \sum_{\substack{j=1 \\ j\neq i}}^{n} \left[\frac{{\rho_0}^{(i)} m^{(j)} P^{(j)}}{{\rho^{(j)}}^2} \right] \frac{\partial W^{(j,i)}}{\partial \mathbf{e}^{(i)}} \tag{3.30}$$

The first term in equation (3.29) is the contribution by all other ' $n-1$ ' particles on particle ' i '. The thermodynamic pressure ' P ' and temperature ' Θ ' depend on the chosen equation of state and are defined as

$$P^{(i)} = {\rho^{(i)}}^2 \frac{\partial u^{(i)}}{\partial \rho^{(i)}} \tag{3.31}$$

$$\Theta^{(i)} = \frac{\partial u^{(i)}}{\partial s^{(i)}} \tag{3.32}$$

The second and last terms in equation (3.29) are contributions from the elements. Equation (3.30) represents a 4 × 1 generalized torque vector.

3.7 Plasticity model

The present formulation uses the plasticity model developed by Fahrenthold and Horban [15]. Plastic deformation is assumed to take place at constant volume. The model assumes an additive decomposition of elastic and plastic deviatoric strains.

$$\bar{\mathbf{E}}^{(j)} = \mathbf{E}^{e(j)} + \mathbf{E}^{p(j)} \tag{3.33}$$

The right Cauchy-Green plastic deformation tensor $\mathbf{C}^p$ is related to the plastic strain tensor $\mathbf{E}^p$ by the expression

$$\mathbf{C}^{p(j)} = \mathbf{I} + 2\ \mathbf{E}^{p(j)} \tag{3.34}$$

or

$$\dot{\mathbf{E}}^{p(j)} = \frac{1}{2}\dot{\boldsymbol{C}}^{p(j)} \tag{3.35}$$

The assumption of isochoric plastic deformation and the fact that “plastic dissipation” has to be a positive semi-definite quantity (which follows from second law of thermodynamics) imposes the constraints

For the isochoric constraint

$$\mathbf{det}\left(\mathbf{C}^{p(j)}\right) = 1 \tag{3.36}$$

or

$$\mathbf{det}\left(\mathbf{C}^{p(j)}\right)\left\{\left(\mathbf{C}^{p(j)}\right)^{-1} : \dot{\mathbf{C}}^{p(j)}\right\} = 0 \tag{3.37}$$

Substituting equation (3.35) into the above equation yields,

$$\left(\mathbf{C}^{p(j)}\right)^{-1} : \dot{\mathbf{E}}^{p(j)} = 0 \tag{3.38}$$

For positive dissipation

$$-\frac{\partial U}{\partial \mathbf{E}^{p(j)}} : \mathbf{E}^{p(j)} \geq 0 \tag{3.39}$$

The partial derivative in equation (3.39) defines the energy conjugate to the plastic strain $\mathbf{E}^{p(j)}$, a second order stress tensor $\mathbf{S}^{(j)}$.

$$\mathbf{S}^{(j)} = -\frac{1}{{V_0}^{(j)}} \frac{\partial U}{\partial \mathbf{E}^{p(j)}} \tag{3.40}$$

$$= 2\mu^{(j)}(1 - d^{(j)}) \left[\bar{\mathbf{E}}^{(j)} - \mathbf{E}^{p(j)} \right] \tag{3.41}$$

3.7.1 Flow rule

The plasticity model used here is based on an incremental plastic strain formulation and makes use of a non-associative flow rule.

$$\Delta \mathbf{E}^{p(j)} = \Delta \lambda^{(j)} \mathbf{W}^{(j)} \tag{3.42}$$

The stress term $\mathbf{W}^{(j)}$ in equation (3.42) is so chosen that the flow law satisfies the isochoric constraint represented by equation (3.36)

$$\mathbf{W}^{(j)} = \mathbf{C}^{p(j)}\mathbf{S}^{(j)} + \mathbf{S}^{(j)}\mathbf{C}^{p(j)} - \frac{1}{3}\, tr \left[\mathbf{C}^{p(j)}\mathbf{S}^{(j)} + \mathbf{S}^{(j)}\mathbf{C}^{p(j)} \right] \mathbf{I} \tag{3.43}$$

$\mathbf{S}^{(j)}$ is the second order stress tensor defined previously in equation (3.40) and $\mathbf{C}^{p(j)}$ is the right Cauchy-Green deformation tensor defined by equation (3.34). ‘ *tr* ’ denotes the trace operator. $\Delta\lambda$ is a scalar which will be defined later.

Let $\tau^{(j)}$ be a scalar measure of the effective stress defined as

$$\tau^{(j)} = \left[\frac{1}{2} \left(\mathbf{S}^{(j)} : \mathbf{S}^{(j)} \right) \right]^{\frac{1}{2}} \tag{3.44}$$

The yield stress $Y^{(j)}$ is in general a function of the initial yield stress, thermal softening, and kinematic hardening and can be expressed as

$$Y^{(j)} = (1 - d^{(j)}) \left\{ Y_0^{(j)} (1 + \beta_0^{(j)} \epsilon^{p(j)})^{n(j)} \right\} \left\{ 1 - \beta_2^{(j)} \Theta^{H(j)} \right\} \tag{3.45}$$

In the equation (3.45), $Y_0^{(j)}$ is the initial yield stress, $\epsilon^{p(j)}$ is the effective plastic strain computed by integrating

$$\dot{\epsilon}^{p(j)} = \left[\frac{1}{2} \left(\dot{\mathbf{E}}^{p(j)} : \dot{\mathbf{E}}^{p(j)} \right) \right]^{\frac{1}{2}} \tag{3.46}$$

$\beta_0^{(j)}$ is the (constant) hardening modulus and $n(j)$ is the (constant) hardening exponent. The temperature $\Theta^{H(j)}$ is defined by the relation

$$\Theta^{H(j)} = \frac{\left(\Theta_{max}^{(j)} - \Theta_0^{(j)} \right)}{\left(\Theta_m^{(j)} - \Theta_0^{(j)} \right)} \tag{3.47}$$

where

$\Theta_0^{(j)}$ = Reference temperature,
$\Theta_m^{(j)}$ = Melt temperature and
$\Theta_{max}^{(j)}$ = Maximum temperature

$\Delta\lambda^{(j)}$ in equation 3.42 is a positive scalar quantity defined by

$$\Delta\lambda^{(j)} = \frac{(\tau^{(j)} - Y^{(j)})\, H(\tau^{(j)} - Y^{(j)})}{(1 - d^{(j)})\, 2\, \mu_o^{(j)}} \tag{3.48}$$

3.8 Damage evolution

Damage mechanics and classical fracture mechanics provide the necessary tools to model the loss of strength of materials and other non-continuum effects, like fracture and fragmentation. However the complexity of using fracture mechanics concepts like the J-integral or the crack opening displacement in a finite strain plasticity setting has favored the use of damage mechanics [42].

Central to the theory of damage mechanics is the concept of a "damage variable". The use of damage variables provides a mechanism to progressively degrade material properties. The damage variable can be a scalar or an appropriate higher order tensor.

In this formulation, two scalar damage variables ' D ' and ' d ' are used to model the loss of strength of the material, in tension and shear respectively. The damage values are initially set to zero, which represents an intact material. The modeling methodology is general enough to incorporate both rate dependent (e.g Grady-Kipp) and rate independent damage evolution schemes. The present work uses a rate independent damage evolution model given by

$$\begin{aligned} \Delta D^{(j)} &= \Lambda\, max\{H[\sigma^{(j)} - \sigma^{sp(j)}], H[\epsilon^{p(j)} - \epsilon^{f(j)}], \\ &\quad H[P^{(j)} - P^{c(j)}], H[\tau^{(j)} - Y^{(j)}]\} \qquad (3.49) \\ \Delta d^{(j)} &= \Lambda\, max\{H[\sigma^{(j)} - \sigma^{sp(j)}], H[\epsilon^{p(j)} - \epsilon^{f(j)}], \\ &\quad H[P^{(j)} - P^{c(j)}], H[\tau^{(j)} - Y^{(j)}]\} \qquad (3.50) \end{aligned}$$

Λ is a constant chosen to be 0.1. This means that damage variables are evolved over ten time steps, after the element has failed due to any of the following

- The tensile pressure $P^{(j)}$ drops below a specified value $P^{c(j)}$
- Effective shear stress $\tau^{(j)}$ exceeds a predefined value $Y^{(j)}$
- The maximum eigenvalue of the deviatoric stress $\sigma^{(j)}$exceeds a specified value $\sigma^{sp(j)}$

- The accumulated plastic strain $\epsilon^{p(j)}$has reached a specified value $\epsilon^{f(j)}$

When the damage value reaches 1.0 the element has lost strength and Λ is reset to zero.

Unlike some finite element based codes, the energy released due to damage evolution goes into irreversible entropy production. This provides a means to rigorously conserve energy.

3.9 Artificial viscosity

Consistent with the general practice in shock physics, the present modeling methodology introduces artificial viscosity to

- Model shocks
- Damp the translational mode of the particles

The viscous damping force due to the relative particle velocity is

$$\mathbf{f}^{(i)} = \sum_{j=1}^{n} \gamma^{(i,j)} \left(\dot{\mathbf{c}}^{(i)} - \dot{\mathbf{c}}^{(j)}\right) \left\{ H \left[-\left(\dot{\mathbf{c}}^{(i)} - \dot{\mathbf{c}}^{(j)}\right) \cdot \left(\mathbf{c}^{(i)} - \mathbf{c}^{(j)}\right) \right] \right\} \tag{3.51}$$

where the damping coefficient $\gamma^{(i,j)}$ is given by

$$\begin{aligned} \gamma^{(i,j)} &= \frac{1}{2} c_o \left(\rho^{(i)} {c_s}^{(i)} A^{(i)} + \rho^{(j)} {c_s}^{(j)} A^{(j)} \right) \times \\ & [1.0 - \zeta(i,j)] \left\{ H \left[1.0 - \zeta(i,j) \right] \right\} \end{aligned} \tag{3.52}$$

' c_o ' is a dimensionless numerical damping coefficient, $c_s^{(i)}$ is the local speed of the sound in the material and $A^{(i)}$ is the cross-sectional area of the particle. The heaviside functions in equation (3.51) and (3.52) ensure that viscous force acts only on particles which are moving towards each other.

3.10 Artificial heat flux

Most hydrocodes use a conduction model to allow heat (generated due to viscous effects) to diffuse through the material. Consistent with this practice, the present formulation makes use of an entropy based heat conduction model of the form

$$\dot{S}^{con(i)} = \frac{1}{\Theta^{(i)}} \sum_{j=1}^{n} \Upsilon^{(i,j)} \left(\Theta^{(i)} - \Theta^{(j)} \right) \tag{3.53}$$

where the heat conduction coefficient $\Upsilon^{(i,j)}$ is defined as

$$\begin{aligned} \Upsilon^{(i,j)} &= \frac{1}{2} k_0 \left\{ \rho^{(i)} {c_s}^{(i)} {c_v}^{(i)} A^{(i)} + \rho^{(j)} {c_s}^{(j)} {c_v}^{(j)} A^{(j)} \right\} \times \\ & \quad [1.0 - \zeta(i,j)] \left\{ H \left[1.0 - \zeta(i,j) \right] \right\} \end{aligned}$$

‘ k_0 ’ is the constant coefficient of heat conduction of the material and ‘ c_v ’ is the specific heat capacity. The heaviside function ensures that conduction occurs only between contacting particles.

3.11 Entropy as a state

The use of an entropy variable couples the mechanical and thermal energy domains. Since entropy is introduced here as a state it is essential to specify an evolution equation that determines the entropy of the system at any instant in time. A general entropy evolution equation for particle ‘ i ’ is written in the form

$$\dot{S}^{(i)} = \dot{S}^{irr(i)} - \dot{S}^{con(i)} \tag{3.54}$$

where $\dot{S}^{irr(i)}$ is the irreversible entropy evolution due to energy dissipation and $\dot{S}^{con(i)}$ is the entropy evolution due to heat conduction. The irreversible entropy evolution rate is given by the expression

$$\dot{S}^{irr(i)} \quad = \quad \frac{1}{\Theta^{(i)}} \; \dot{\nu}^{(i)} \tag{3.55}$$

The dissipative power $\nu^{(i)}$ in equation (3.55) can be decomposed into contributions from three main sources

$$\dot{\nu}^{(i)} \quad = \quad \dot{\nu}^{(i)}_{viscous} + \dot{\nu}^{(i)}_{plastic} + \dot{\nu}^{(i)}_{damage} \tag{3.56}$$

The viscous power $\dot{\nu}^{(i)}_{viscous}$ in equation (3.56) is due to energy dissipation via artificial viscosity, described in section (3.9), and can be expressed as

$$\dot{\nu}^{(i)}_{viscous} \quad = \quad \mathbf{f}^{(i)} \cdot \dot{\mathbf{c}}^{(i)} \tag{3.57}$$

The power dissipated in damage evolution $\dot{\nu}^{(i)}_{damage}$ is given by

$$\dot{\nu}^{(i)}_{damage} \quad = \quad \sum_{j=1}^{n_e^{(i)}} \frac{1}{n_p} \left\{ \Gamma^{d(k^{(i,j)})} \dot{d}^{(k^{(i,j)})} + \Gamma^{D(k^{(i,j)})} \dot{D}^{(k^{(i,j)})} \right\} \tag{3.58}$$

where ‘ n_p ’ is the number of particles per element, ‘ $n_e^{(i)}$ ’ is the number of elements associated with particle ‘ i ’ and $k^{(i,j)}$ is the element associated with the i^{th} particle. $\Gamma^{D(j)}$ and $\Gamma^{d(j)}$ are the rate at which energy is released during damage evolution, given by

$$\Gamma^{D(j)} \quad = \quad -\frac{\partial U}{\partial D^{(j)}} \tag{3.59}$$

$$\Gamma^{d(j)} = -\frac{\partial U}{\partial d^{(j)}} \tag{3.60}$$

The power dissipated in plastic flow is given by

$$\dot{\nu}^{(i)}_{plastic} = \sum_{j=1}^{n_e^{(i)}} \frac{1}{n_p} \{\mathbf{S}^{(k^{(i,j)})} : \dot{\mathbf{E}}^{p(k^{(i,j)})}\}\, V_0^{(j)} \tag{3.61}$$

$\mathbf{S}^{(k^{(i,j)})}$ is the second Kirchoff-Piola deviatoric stress tensor defined by equation (3.40).

3.12 State equations

In the earlier sections, expressions for the internal energy and kinetic energy were developed. The Hamiltonian for the thermo-mechanical system is defined as the sum of the kinetic and internal energies.

$$\Pi = T + U = \Pi\left(\mathbf{p}^{(i)}, \mathbf{c}^{(i)}, \mathbf{h_e}^{(i)}, \mathbf{e}^{(i)}, S^{(i)}, d^{(j)}, D^{(j)}, \mathbf{E}^{p(j)}\right) \tag{3.62}$$

Hamilton's canonical equations can then be written as

$$\dot{\mathbf{p}}^{(i)} = -\frac{\partial \Pi}{\partial \mathbf{c}^{(i)}} + \mathbf{q}^{\mathbf{c}^{(i)}} \tag{3.63}$$

$$\dot{\mathbf{c}}^{(i)} = \frac{\partial \Pi}{\partial \mathbf{p}^{(i)}} \tag{3.64}$$

$$\dot{\mathbf{h_e}}^{(i)} = -\frac{\partial \Pi}{\partial \mathbf{e}^{(i)}} + \mathbf{q}^{\mathbf{e}^{(i)}} \tag{3.65}$$

$$\dot{\mathbf{e}}^{(i)} = \frac{\partial \Pi}{\partial \mathbf{h_e}^{(i)}} \tag{3.66}$$

$$0 = -\frac{\partial \Pi}{\partial S^{(i)}} + q^{S^{(i)}} \tag{3.67}$$

$$0 = -\frac{\partial \Pi}{\partial D^{(j)}} + q^{D^{(j)}} \tag{3.68}$$

$$0 = -\frac{\partial \Pi}{\partial d^{(j)}} + q^{d^{(j)}} \tag{3.69}$$

$$0 = -\frac{\partial \Pi}{\partial \mathbf{E}^{p(j)}} + \mathbf{q}^{p^{(j)}} \tag{3.70}$$

Equations (3.63) and (3.64) represent the translational state equations, (3.65) through (3.66) represent the rotational motion of the particles, (3.67) represents entropy evolution, (3.68) and (3.69) represent damage evolution and (3.70) represents the equation for the evolution of plastic strain.

$\mathbf{q}^{\mathbf{c}^{(i)}}$, $q^{S^{(i)}}$, $q^{D^{(j)}}$, $q^{d^{(j)}}$, $\mathbf{q}^{p^{(j)}}$ are the generalized nonconservative forces which are determined by the nonholonomic constraints (3.57), (3.58) and (3.61). The above equations are supplemented by the evolution equations for $S^{(i)}$, $d^{(j)}$, $D^{(j)}$ and $\mathbf{E}^{p^{(j)}}$. Lagrange multipliers are introduced to apply the nonholonomic constraints (3.54). Specifically,

$$\mathbf{q}^{\mathbf{c}^{(i)}} = -\left(\frac{\gamma^{S^{(i)}}}{\Theta^{S^{(i)}}}\right)\mathbf{f}^{(i)} \tag{3.71}$$

$$q^{S^{(i)}} = \gamma^{S^{(i)}} \tag{3.72}$$

$$q^{D^{(j)}} = \gamma^{D^{(j)}} - \Gamma^{D^{(j)}} \frac{1}{n_p} \sum_{i=1}^{n_p} \left(\frac{\gamma^{S^{(k(j,i))}}}{\Theta^{k(j,i)}}\right) \tag{3.73}$$

$$q^{d(j)} = \gamma^{d(j)} - \Gamma^{d(j)} \frac{1}{n_p} \sum_{i=1}^{n_p} \left(\frac{\gamma^{S(k(j,i))}}{\Theta^{k(j,i)}} \right) \tag{3.74}$$

$$\mathbf{q}^{p(j)} = \mathbf{G}^{p(j)} - V_0{}^{(j)} \mathbf{S}^{(j)} \sum_{i=1}^{n_p} \left(\frac{\gamma^{S(k(j,i))}}{\Theta^{k(j,i)}} \right) \tag{3.75}$$

Equation (3.67) forces the Lagrangian multiplier $\mathbf{q}^{S(i)}$ to be equal to the temperature $\Theta^{(i)}$. This results in a simplification of equations (3.71) through (3.75).

Equations (3.65) and (3.66) model the rotational dynamics of the particles. Simplification of these equations follow from the results in section (2.5.4) of chapter (2).

The aforementioned simplifications result in the final form Hamilton's equations

$$\dot{\mathbf{p}}^{(i)} = -\mathbf{g}^{(i)} - \mathbf{f}^{(i)} \tag{3.76}$$

$$\dot{\mathbf{c}}^{(i)} = \frac{1}{m^{(i)}} \mathbf{p}^{(i)} \tag{3.77}$$

$$\dot{\mathbf{h}}'^{(i)} = -\boldsymbol{\Omega}'^{(i)} \mathbf{h}'^{(i)} - \frac{1}{2} \mathbf{G}^{(i)} \boldsymbol{\tau}^{(i)} \tag{3.78}$$

$$\dot{\mathbf{e}}^{(i)} = \frac{1}{2} \mathbf{G}^{(i)T} \boldsymbol{\omega}'^{(i)} \tag{3.79}$$

$$\dot{S}^{(i)} = \dot{S}^{irr(i)} - \dot{S}^{con(i)} \tag{3.80}$$

$$D^{(j)} = D\left(\rho^{(i)}, s^{(i)}, \mathbf{c}^{(i)}, D^{(j)}, d^{(j)}, \mathbf{E}^{p(j)}\right) \tag{3.81}$$

$$d^{(j)} = d\left(\rho^{(i)}, s^{(i)}, \mathbf{c}^{(i)}, D^{(j)}, d^{(j)}, \mathbf{E}^{p(j)}\right) \tag{3.82}$$

$$\mathbf{E}^{p(j)} = \lambda^{(j)}\left\{\frac{1}{2}\mathbf{W}^{(j)T} : \mathbf{W}^{(j)}\right\}^{-\frac{1}{2}}\mathbf{W}^{(j)} \tag{3.83}$$

3.13 Computational Issues

3.13.1 Integration routine

Hamilton's equations are a set of first order differential equations, which can be integrated using a standard integration routine. In the present work an explicit, variable time step, second order Runge-Kutta routine is used. The time step is computed from the system characteristic frequencies. Specifically

$$\Delta t = \left(\frac{1}{c_4}\right)\frac{1}{\sqrt{\mathrm{w}_{max}}} \qquad \text{where} \tag{3.84}$$

$$\mathrm{w}_{max} = \max\left\{\mathrm{w}_k^{(i)},\ k = 1, 2, \ldots, 5 \text{ and } i = 1, 2, 3, \ldots, np\right\} \tag{3.85}$$

c_4, is a dimensionless constant, $\mathrm{w}_k^{(i)}$ are the squared frequencies given by

$$\mathrm{w}_k^{(i)} = |\dot{p}_k^{net}|/(m^{(i)}h_{min}); \quad k = 1, 2, 3 \tag{3.86}$$

$$\mathrm{w}_4^{(i)} = {\mathbf{p}^{(i)}}^2/(m^{(i)}h_{min}) \tag{3.87}$$

$$\mathrm{w}_5^{(i)} = |\dot{S}^{net}|/{(m^{(i)}c_v^{(i)})}^2 \tag{3.88}$$

$\dot{p}_k^{net}$ is the net rate of change of linear momenta and is given by the right hand side of equation (3.76), and $\dot{S}^{net}$ is the net rate of change of entropy evolution given by equation (3.80). h_{min} is the minimum of the semi-major lengths of the ellipsoidal particles, given by

$$h_{min} \quad = \quad min \left\{ h_1^{(i)}, h_2^{(i)}, h_3^{(i)}, \quad i = 1, 2, 3, \ldots, n \right\} \tag{3.89}$$

3.13.2 Neighbor search

Equations (3.5), (3.29), (3.30), (3.51) and (3.53) involve summations over ‘ $(n-1)$ ’ particles and in general require an $O(n^2)$ computational effort. However, an efficient nearest neighbor finding algorithm provides a significant saving in computational cost. The current formulation uses linked lists [33] to reduce the number of particles which contribute to the summation. Alternative techniques based on tree search methods can also be used.

3.13.3 Parallel Implementation

Three dimensional simulation of hypervelocity impact phenomena requires large amounts of memory and CPU time. With the emergence of massively parallel computers, there has been a significant change in the way in which hypervelocity impact computations are performed. The model developed here is implemented in parallel using OpenMP compiler directives. A more detailed discussion is provided in section (4.4) of chapter (4)

3.14 Examples

3.14.1 Initial validation

One dimensional wall shock problem

Initial validation of the model is done by solving a one dimensional wall shock problem [55] using an ideal gas equation of state with density shift. The expressions for the internal energy $u^{(i)}$, pressure $P^{(i)}$ and temperature $\Theta^{(i)}$ of particle ' i ' are

$$\begin{aligned}
u^{(i)} &= c_v \left(\Theta^{(i)} - \Theta_0\right) && (3.90)\\
P^{(i)} &= (\gamma - 1) c_v \Theta^{(i)} \left(\rho^{(i)} - \rho_0\right) && (3.91)\\
\Theta^{(i)} &= \Theta_0 \exp\left[\frac{\left(s^{(i)} - s_0\right)}{c_v}\right]\left[\frac{\rho^{(i)}}{\rho_0}\right]^{(\gamma-1)} \exp\left[(\gamma - 1)\left(\frac{\rho_0}{\rho^{(i)}} - 1\right)\right] && (3.92)
\end{aligned}$$

where c_v is the specific heat at constant volume, γ is the ratio of specific heats, s_0 is the reference entropy, ρ_0 is the reference density, and Θ_0 is the reference temperature.

This problem can be treated as a benchmark problem to test codes in shock physics. In this problem, response of a stream of particles (ideal gas) to shock compression is studied. The shock is generated by impact of the particles with a rigid wall, located at $x = 1.25\,cm$. The system consists of ' 201 ' particles uniformly distributed over the region $0 < x < 2.5\,cm$. The number of finite elements is ' 200 '. The initial conditions for the simulation i.e at ' $t = 0$ ' are,

$$\begin{aligned}
\rho^{(i)} &= 1.0\,g/cm^3 && (3.93)\\
s^{(i)} &= 1.0\,Mb - cm^3/(g - {}^oK) && (3.94)
\end{aligned}$$

$$\dot{c}^{(i)} = \begin{cases} +1.0\,cm/\mu s & \text{for } x < 0 \\ -1.0\,cm/\mu s & \text{for } x > 0 \end{cases} \qquad (3.95)$$

Since this example problem is one dimensional, there is no rotation of the particles. Equations (3.76) through (3.83) are integrated using a second order Runge-Kutta algorithm. The simulation parameters are given in table (3.1).

The exact post-shock solution [12] for this problem can be obtained by application

Simulation parameters	
Ratio of specific heats(γ)	$\frac{5}{3}$
Reference density(ρ_0)	$1.0\, g/cm^3$
Reference temperature(Θ_0)	$1.0\, ^oK$
Reference entropy(s_0)	$0.0\, Mb - cm^3/\,(g - {}^oK)$
Specific heat(c_v)	$1.0\, Mb - cm^3/\,(g - {}^oK)$
Viscosity coefficient(c_0)	2.0
Conduction coefficient(k_0)	0.0

Table 3.1: Wall shock problem: simulation parameters

of the Rankine Hugoniot equations.

$$\rho = 2.618\, g/cm^3 \tag{3.96}$$

$$s = 0.176\, Mb - cm^3/(g - {}^oK) \tag{3.97}$$

$$P = 1.618\, Mb \tag{3.98}$$

$$\Theta = 1.5^o\, K \tag{3.99}$$

Figures (3.2) through (3.6) show a good agreement between numerical (represented by solid line) and exact (represented by the dotted line) solutions for density, velocity, pressure, temperature and entropy at 0.4 microseconds.

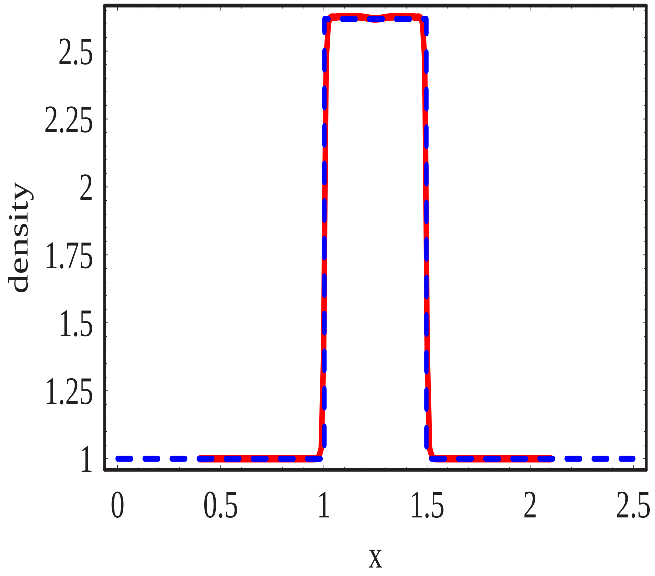

Figure 3.2: Exact and numerical density distribution at $t = 0.4\mu s$

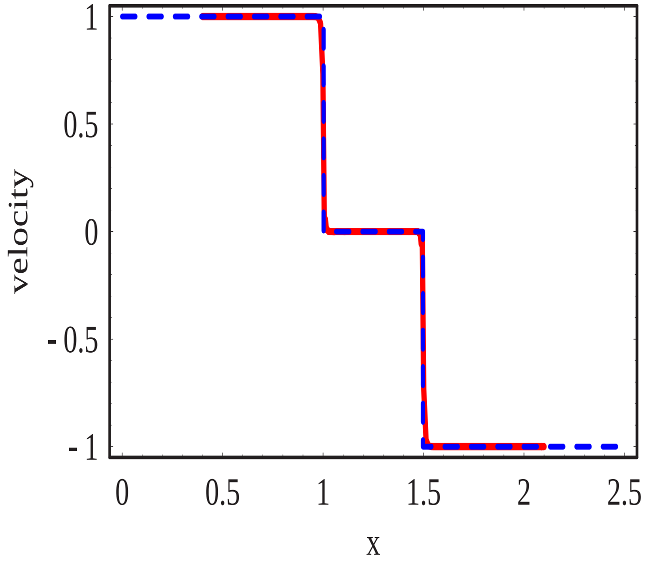

Figure 3.3: Exact and numerical velocity distribution at $t = 0.4\mu s$

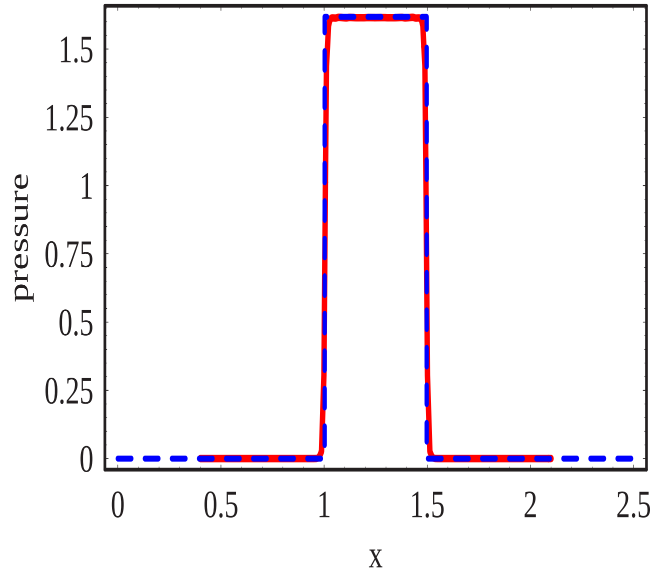

Figure 3.4: Exact and numerical pressure distribution at $t = 0.4\mu s$

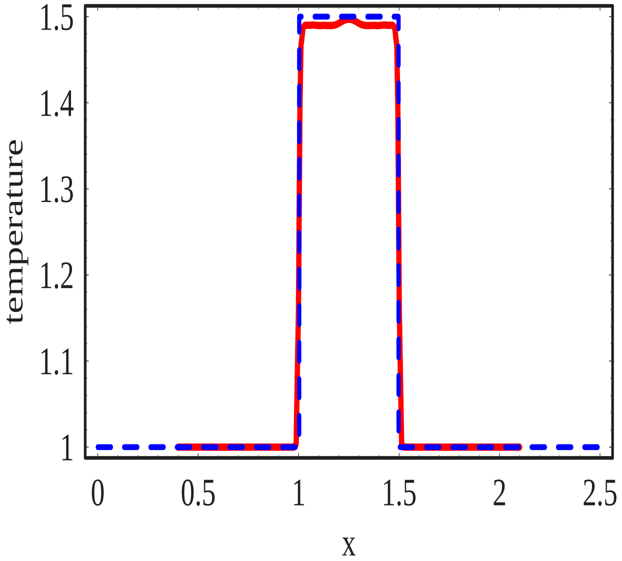

Figure 3.5: Exact and numerical temperature distribution at $t = 0.4\mu s$

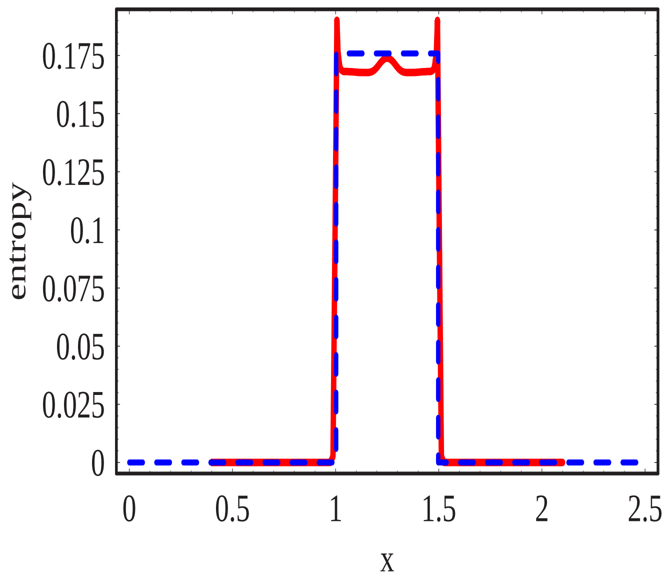

Figure 3.6: Exact and numerical entropy distribution at $t = 0.4\mu s$

3.14.2 Simulation with spherical particles

The model developed earlier in this chapter was numerically implemented in the three dimensional parallel code EXOS. In this section, numerical simulations of problems involving thermo-mechanics, elastic-plastic effects and significant damage to the continuum are presented. The simulation results presented here involve spherical particles, which are a special case of the more general model developed earlier. Because of the inherent symmetry involved with spherical particles, there is no rotational motion of the particles. Three simulation examples are presented, with velocities ranging from 1 km/s to 11 km/s.

1. **EXOS simulation: Depleted Uranium(DU) 0.75% Ti long rod impact on a steel plate**

   The first example is a depleted Uranium, 0.75% Titanium long rod impacting a steel plate. Table (3.2) shows the simulation parameters. Figures (3.7) and

Simulation parameters	
Projectile diameter (DU 0.75% Ti)	0.767 cm
Projectile length (L/D= 10 cylinder)	7.67 cm
Projectile velocity	1.21 km/s
Plate velocity	0.217 km/s
Impact obliquity	73.5 degrees
Plate thickness(steel)	0.64 cm
Equation of state type	Mie-Gruneisen
Number of particles	1,565,190
Number of elements	554,657
Simulation time	100 microseconds
Wall clock time (16 cpus, SGI Onyx)	58.6 hours

Table 3.2: Depleted Uranium(DU) 0.75% Ti long rod impact on a steel plate

(3.8) show the initial configuration of the projectile and target, as particle and element plots respectively. The simulation was run for 100μsecs. Figures (3.9) and (3.10) show the particle and element plots at the end of the simulation. Figures (3.11) and (3.12) show a closeup of the projectile and the target at the end of simulation, with color on plastic strain. The experimental results [30] report a residual rod length of 5.55 cm and a residual velocity of 1.069 km/s. The simulation results show a residual rod length of 5.56 cm and a residual velocity 1.069 km/s. The simulation results are in good agreement with the experimental results.

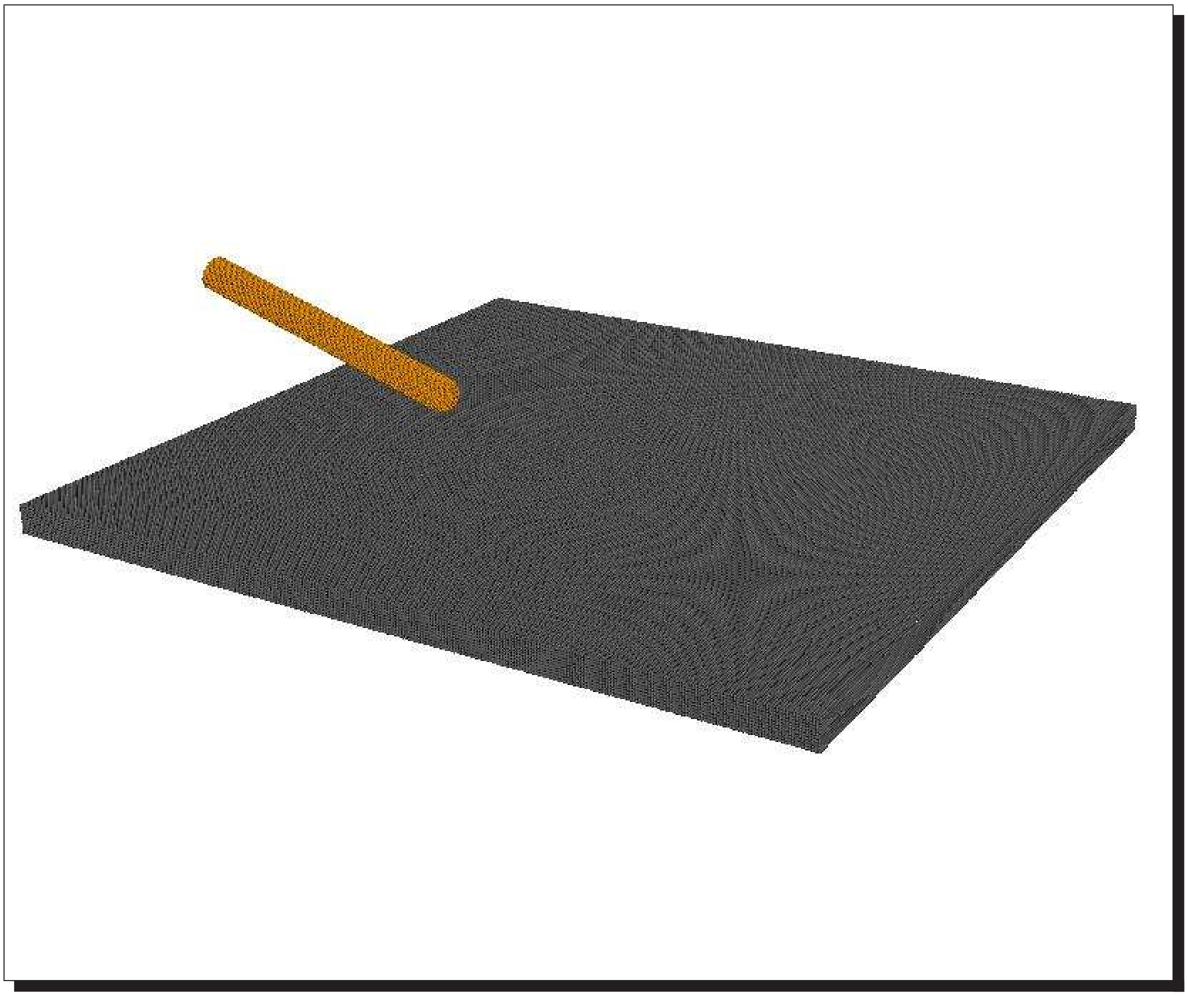

Figure 3.7: DU 0.75% Ti long rod impact on steel plate: initial configuration, particle plot

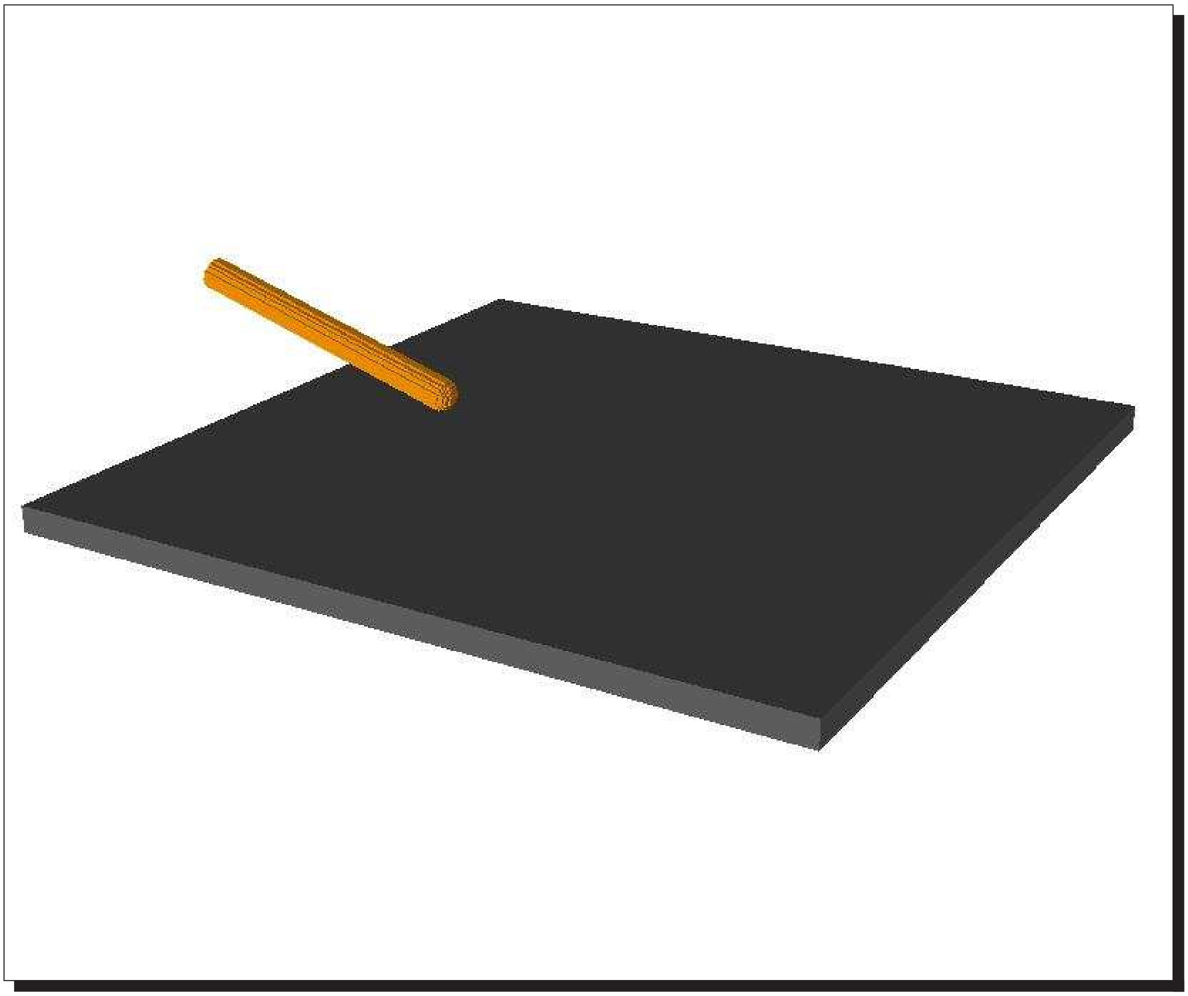

Figure 3.8: DU 0.75% Ti long rod impact on steel plate: initial configuration, element plot

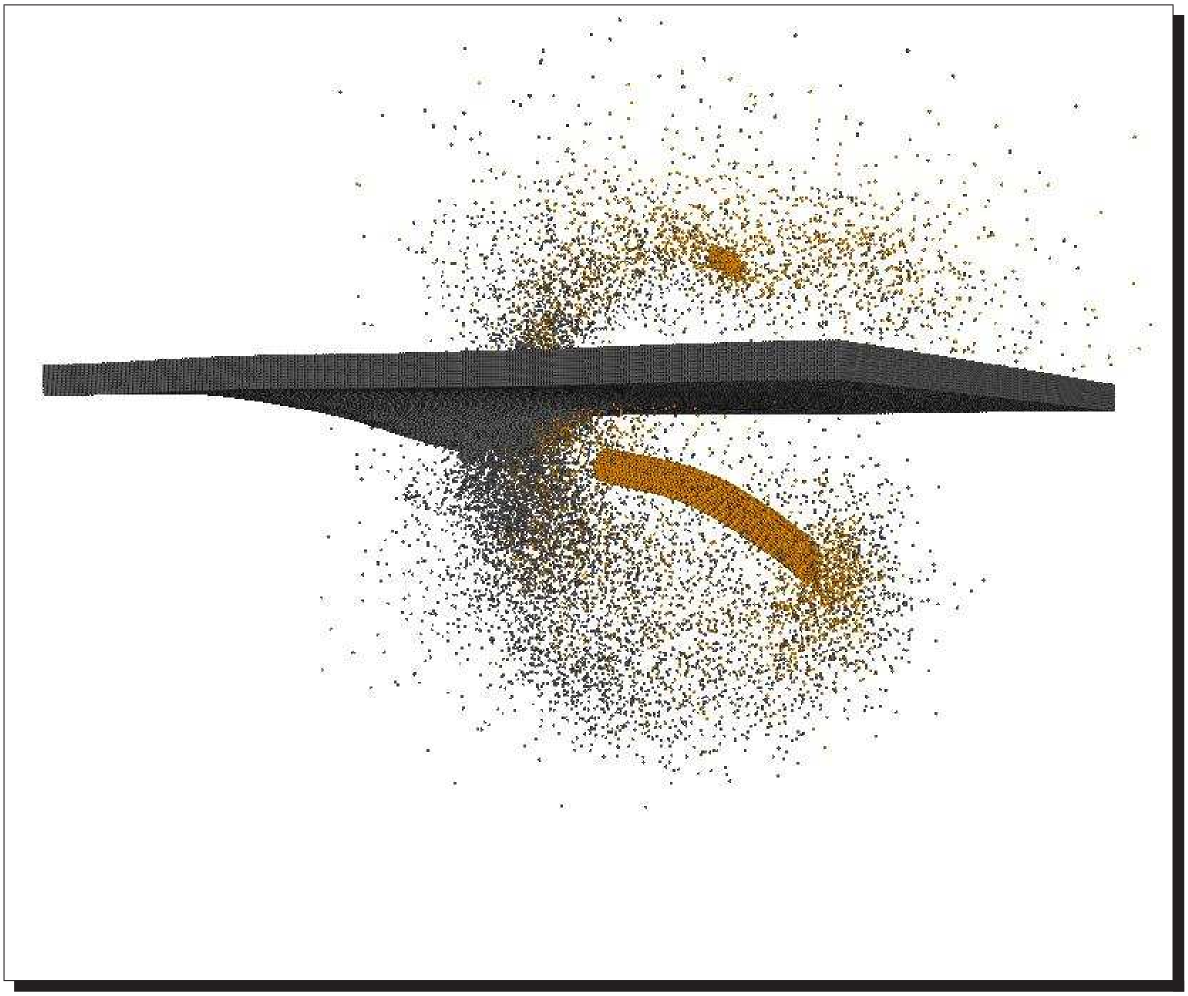

Figure 3.9: DU 0.75% Ti long rod impact on steel plate: final configuration, particle plot

Figure 3.10: DU 0.75% Ti long rod impact on steel plate: final configuration, element plot

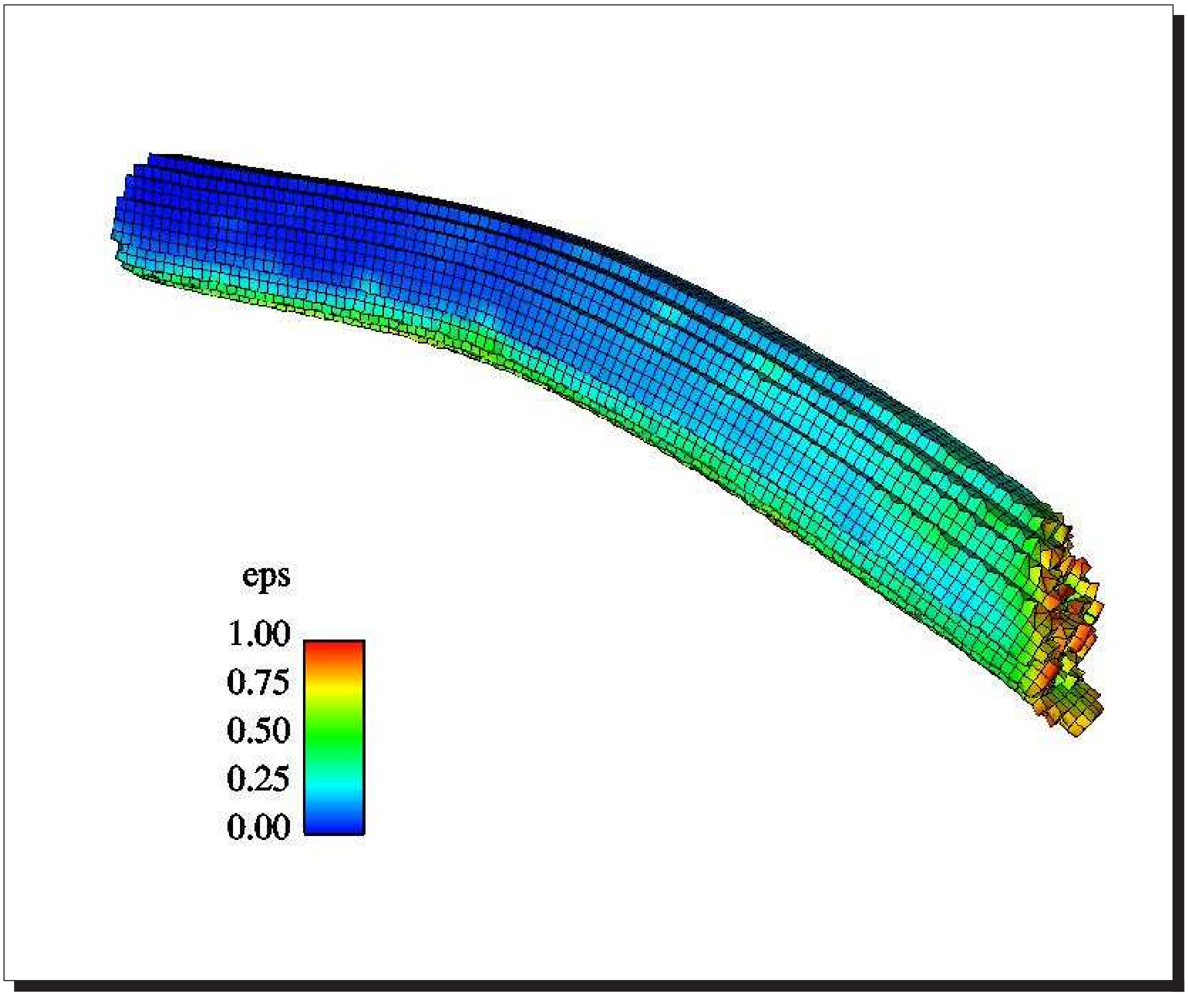

Figure 3.11: DU 0.75% Ti long rod impact on steel plate: projectile at the end of the simulation

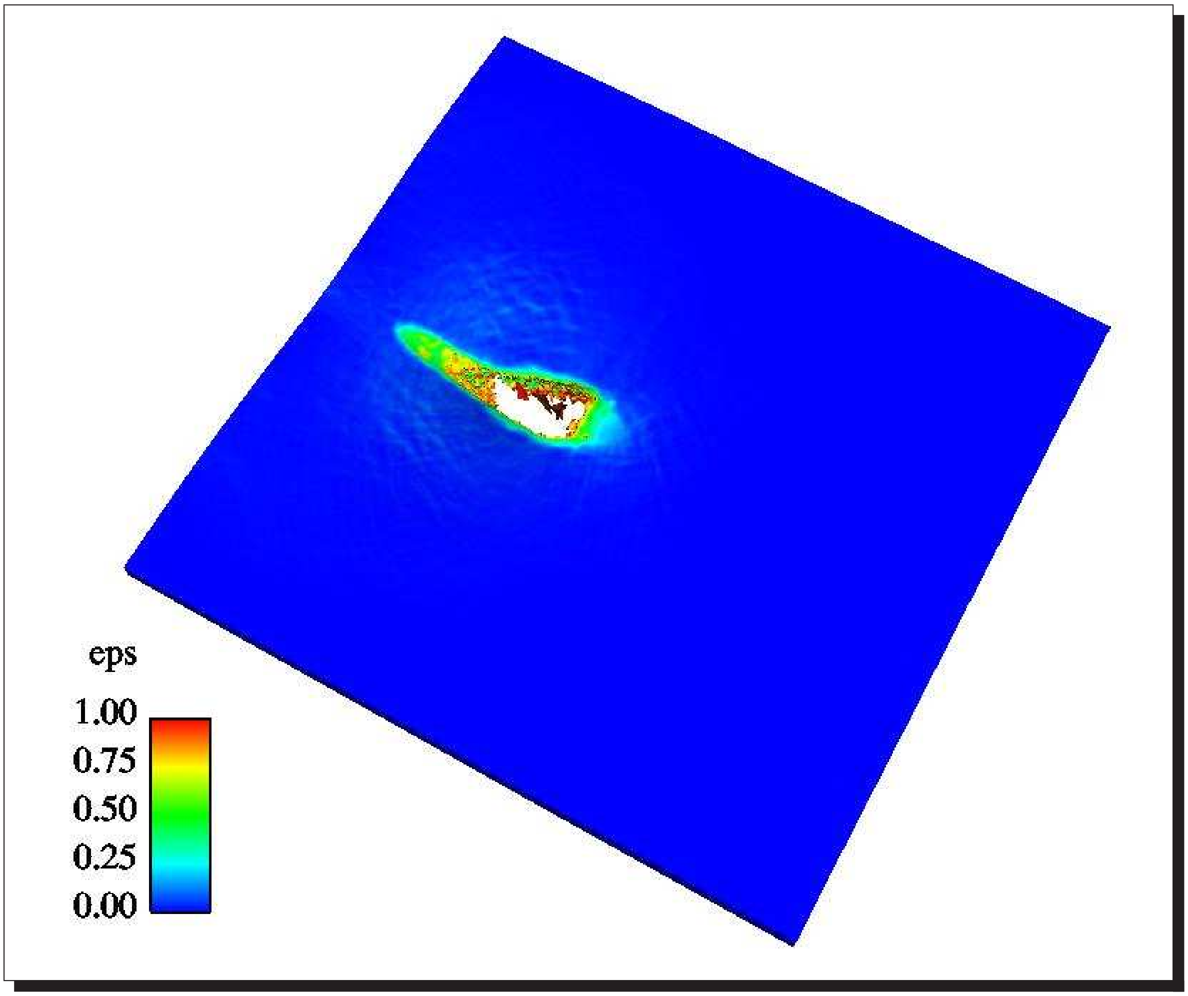

Figure 3.12: DU 0.75% Ti long rod impact on steel plate: target at the end of the simulation

2. **EXOS simulation: Multi-plate shield impact, ESA benchmark case #4**

   In this example, simulation of the oblique impact of a projectile on an aluminum double bumper system is performed. Simulation studies attempted using SPH based codes have resulted in a poor match up with the experimental results [21]. The simulation parameters are shown in table (3.3). Figure (3.13) shows an element plot of the initial configuration. The model employed four elements across each shield plate, eight elements across the diameter of the cylindrical projectile and eight elements across the wall plate. The wall plate dimensions are approximately 30×30 cm. Figures (3.14), (3.15) and (3.16) show element plots at the end of 67 μsecs, 94 μsecs and 133 μsecs. Consistent with the experiment results, the simulation showed no wall plate perforation. The simulation was carried further, to end at 150 μsecs. Figures (3.17) and (3.18) show the element and particle plots at 150μsecs. The simulation showed

Simulation parameters	
Projectile diameter (aluminum cylinder)	0.5062 cm
Projectile length	2.2046 cm
First bumper thickness (aluminum plate)	0.25 cm
Second bumper thickness (aluminum plate)	0.25 cm
Wall thickness (aluminum plate)	0.50 cm
Bumper-to-bumper spacing	6.00 cm
Bumper-to-wall spacing	6.00 cm
Impact velocity	11.0 km/sec
Impact obliquity	45 degrees
Equation of state type	SESAME 3719
Number of particles	4,269,067
Total simulation time	150 microseconds
Wall clock time	53.8 hours
Number of processors (SGI Origin)	256

Table 3.3: Multi-plate shield impact, ESA benchmark case #4

only a bulge in the wall plate.

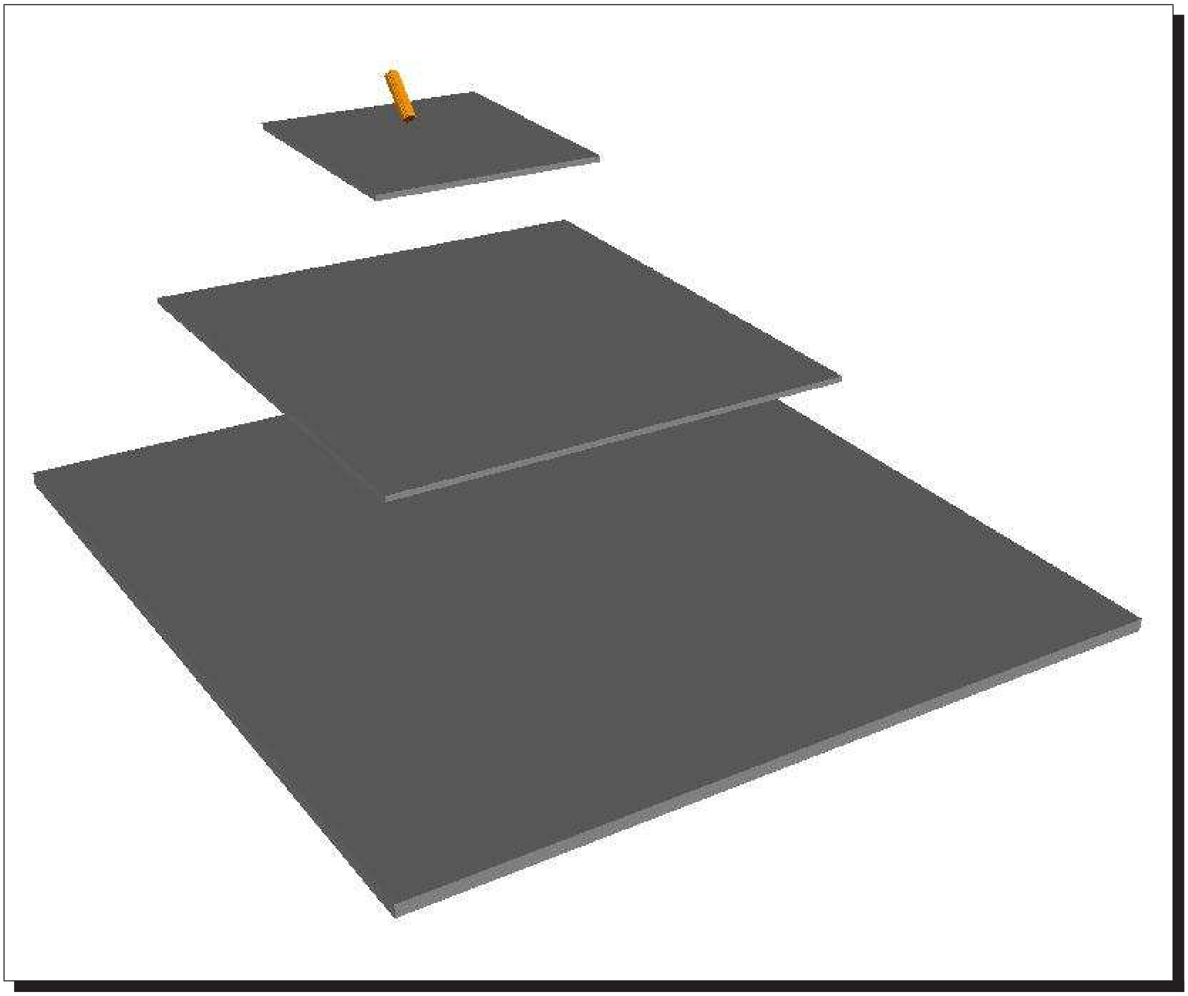

Figure 3.13: ESA4: initial configuration, element plot

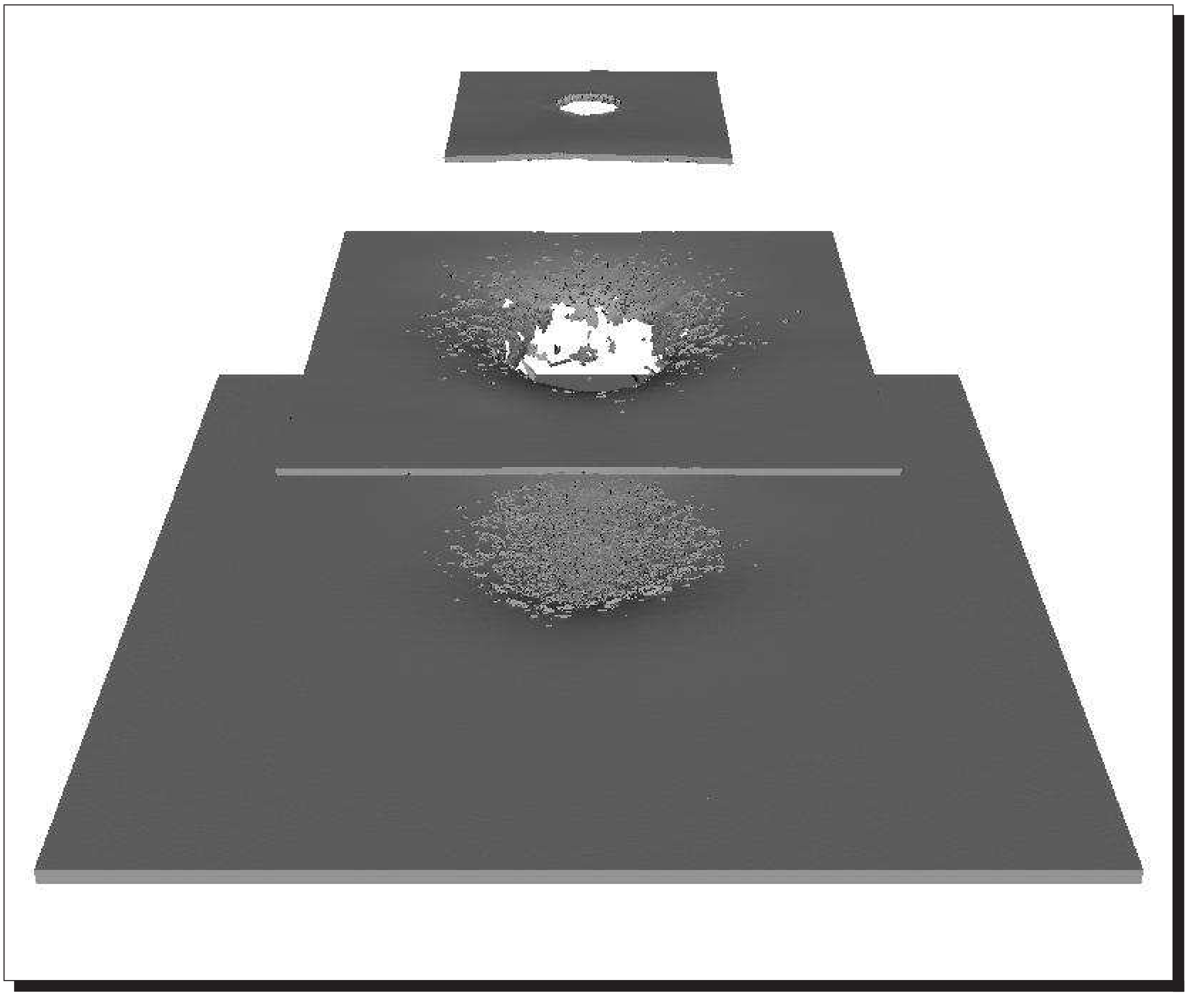

Figure 3.14: ESA4: element plot at $t = 67\,\mu$ secs

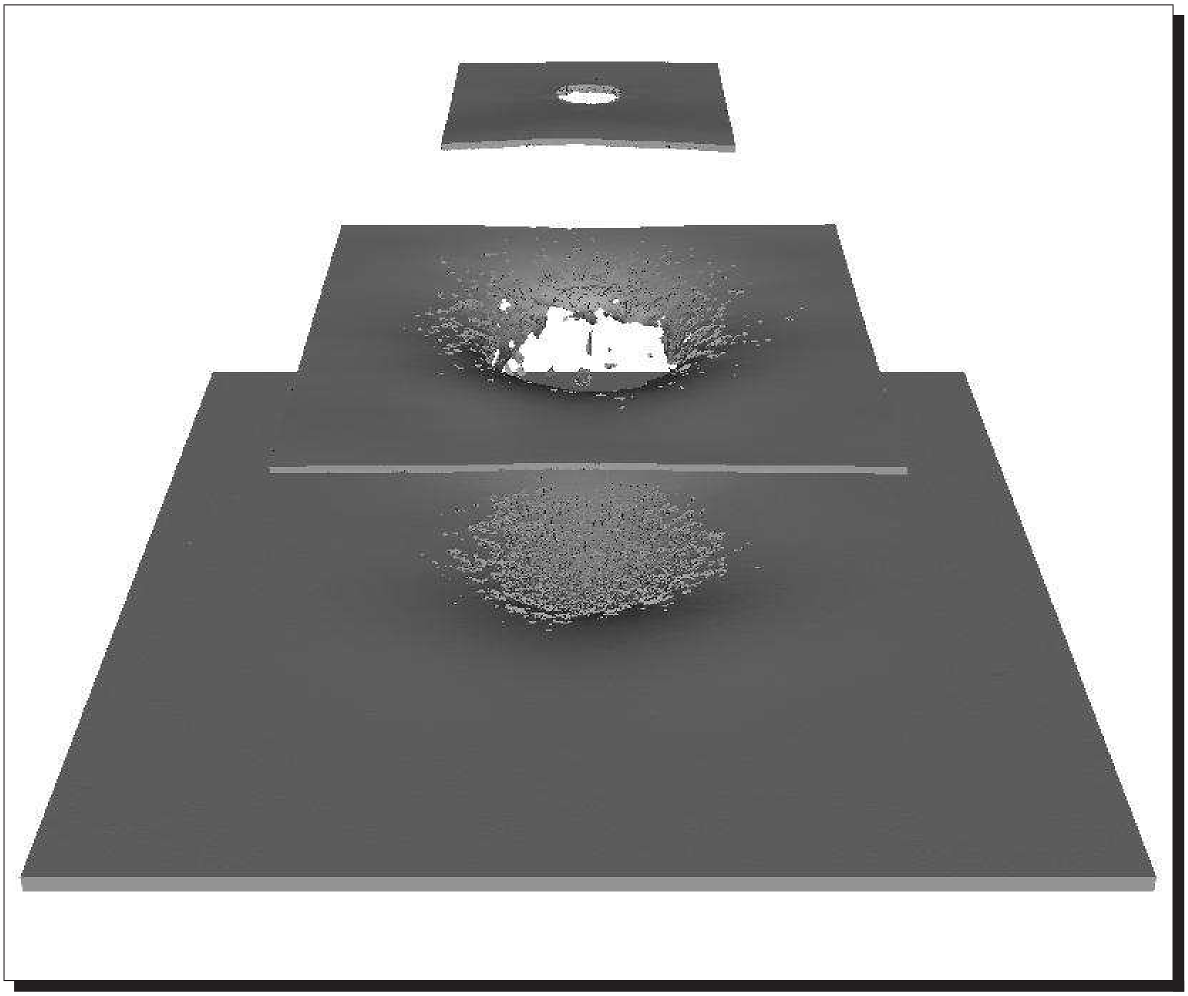

Figure 3.15: ESA4: element plot at $t = 94\,\mu$ secs

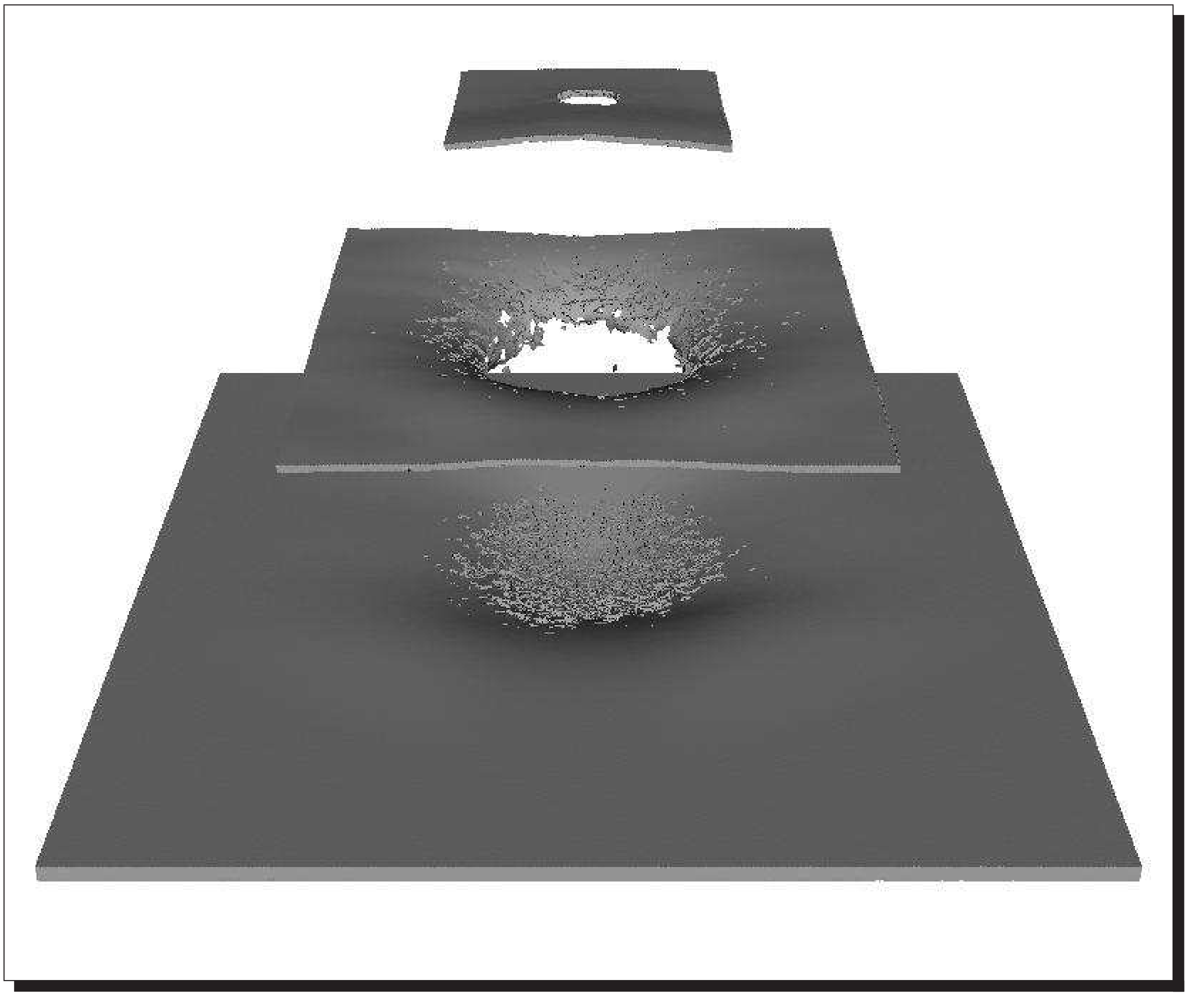

Figure 3.16: ESA4: element plot at $t = 133\,\mu$ secs

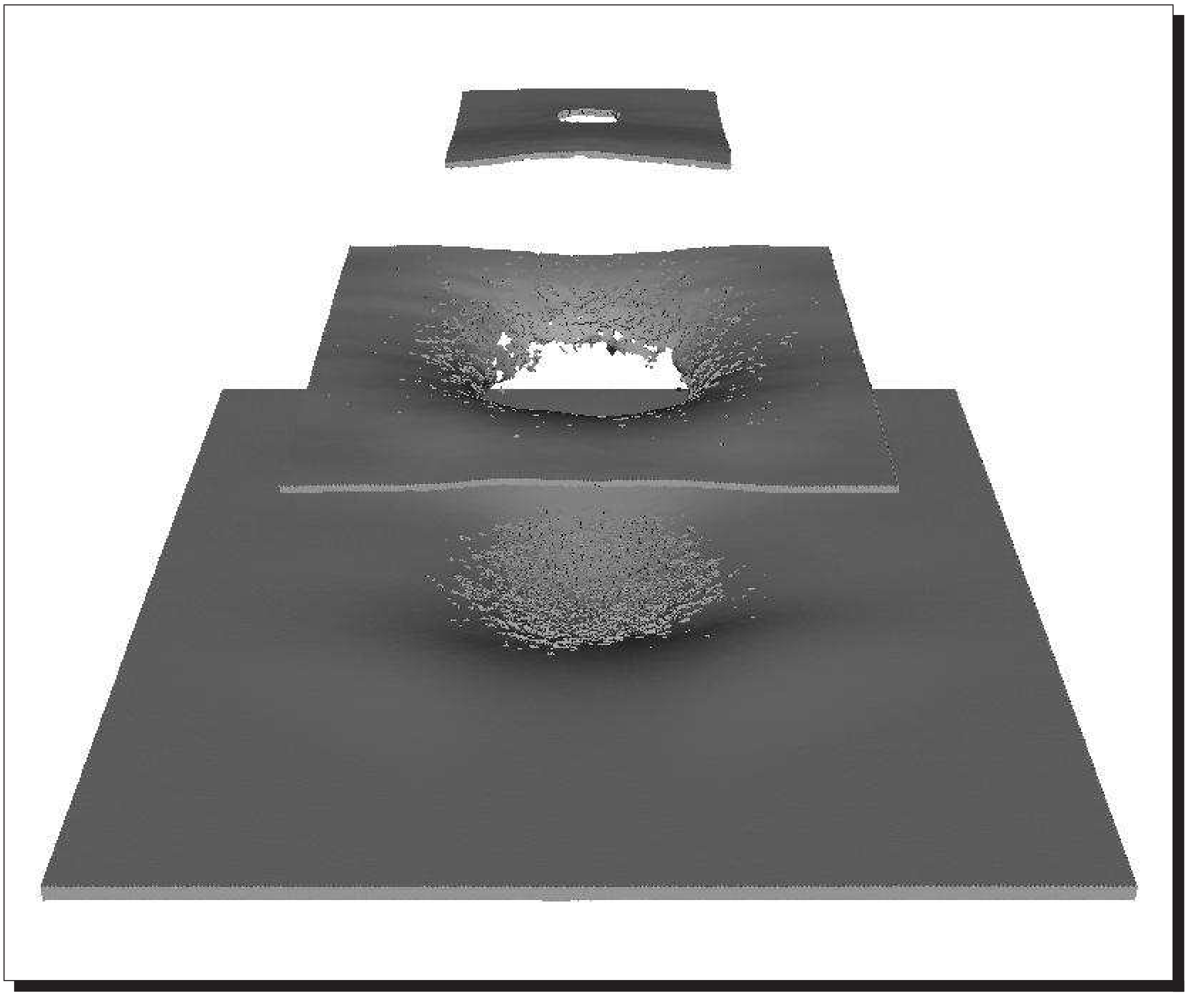

Figure 3.17: ESA4: element plot at $t = 150\,\mu$ secs

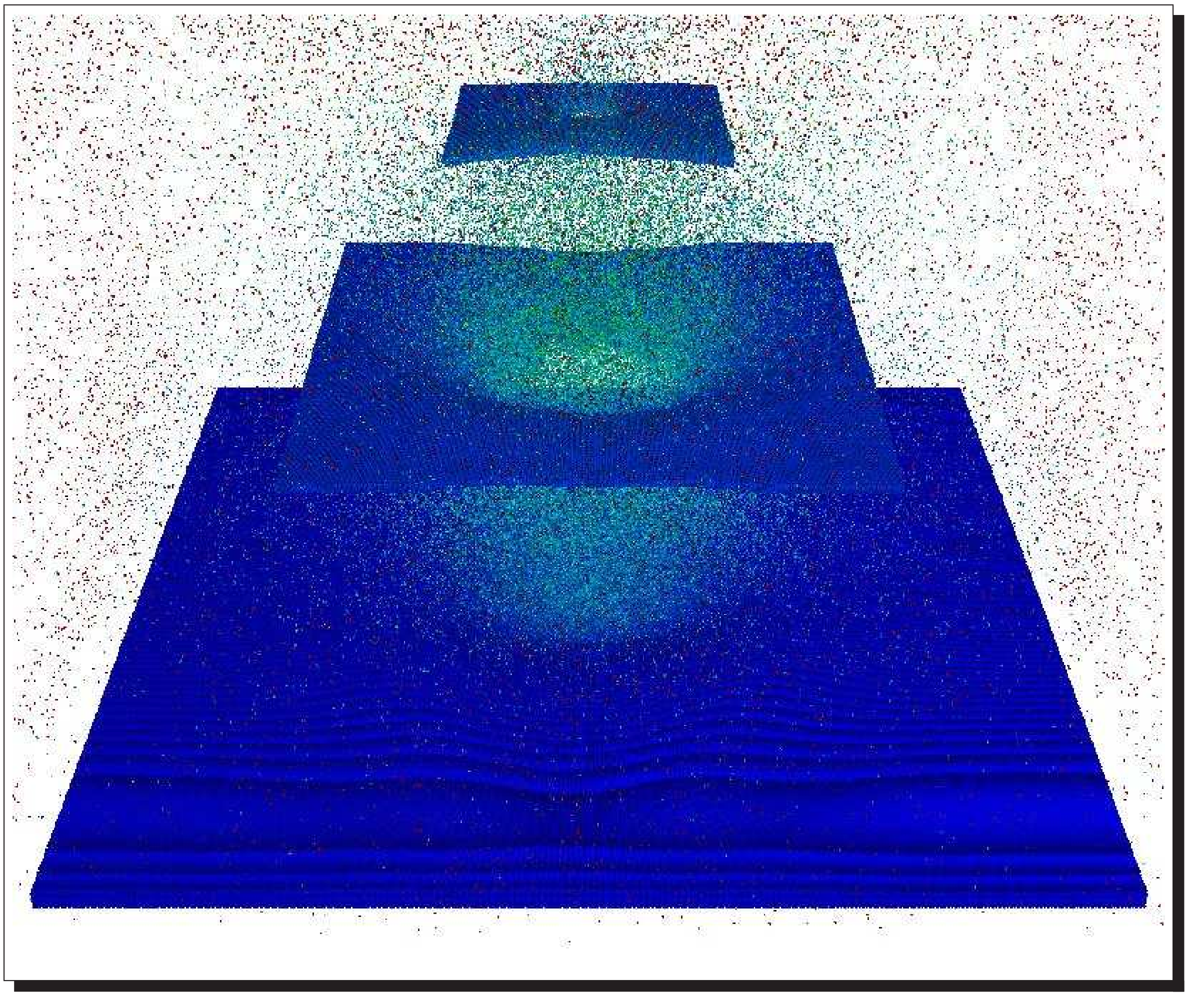

Figure 3.18: ESA4: particle plot at $t = 150\,\mu$ secs

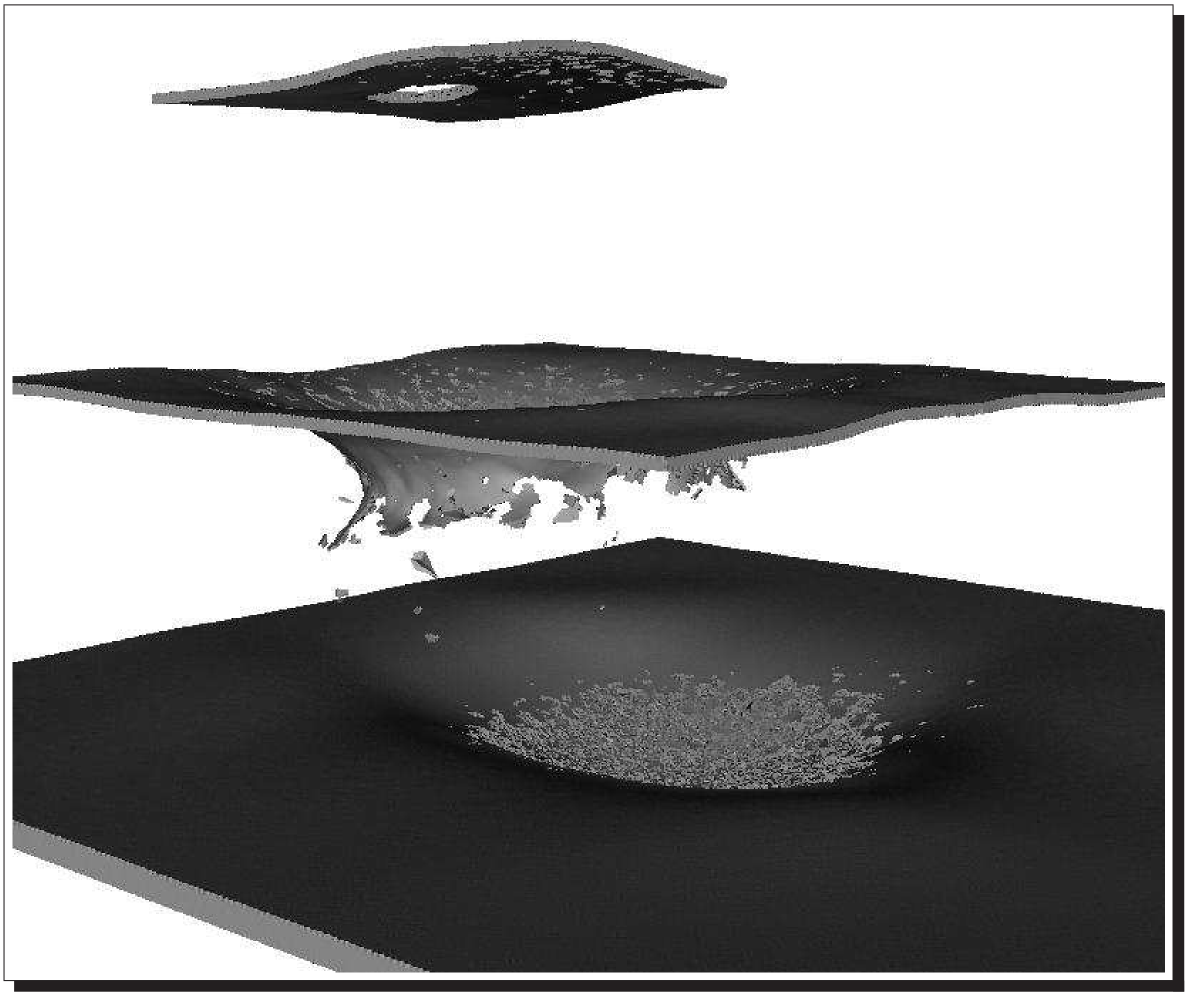

Figure 3.19: ESA4: close up element plot at $t = 150\,\mu$ secs

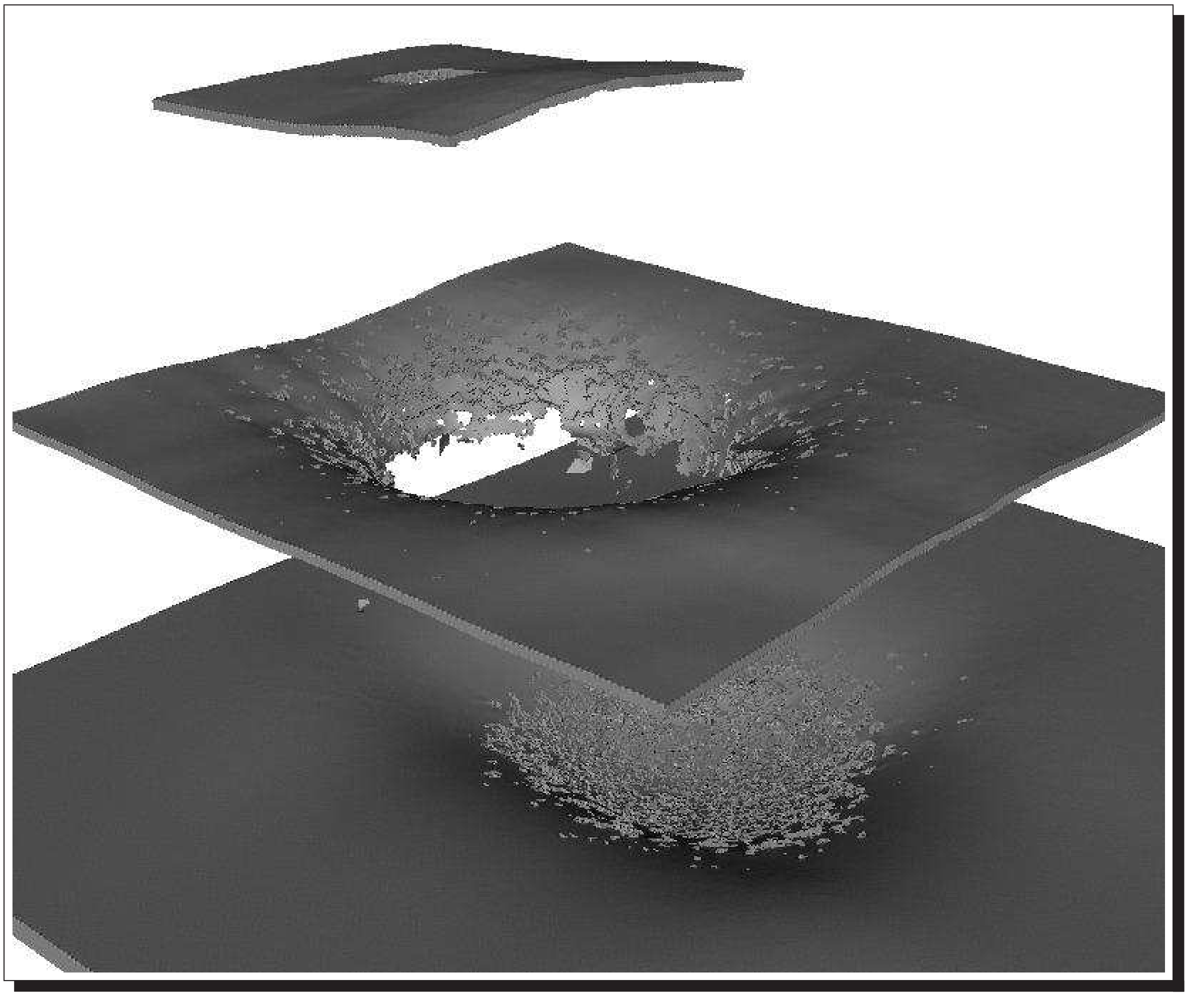

Figure 3.20: ESA4: close up element plot at $t = 150\,\mu$ secs

3. **EXOS simulation: Tungsten long rod impact on a steel plate at 1.833 km/s**

This example simulation involved a long cylindrical tungsten rod, $\frac{L}{D}$ ratio of 20, impacting a steel plate at 1.833 km/sec. The simulation parameters are given in table (3.4). Figure (3.21) and (3.22) show element and particle plots of the initial configuration. The simulation was performed for 150 μ secs. Figures (3.23), (3.24) and (3.26) show different views of the element plot at the end of simulation. Figure (3.25) shows a particle plot at the end of simulation. Figures (3.27) and (3.28) show element plots, with color on plastic strain, at the end of simulation. A comparison of the simulation and experimental results is shown in table (3.5). The simulation results are in good agreement with the experimental results [75].

Simulation parameters	
Projectile diameter (tungsten, L/D=20 cylinder)	0.475cm
Impact velocity	1.833 km/s
Impact obliquity	75 degrees
Plate thickness (steel)	0.95 cm
Equation of state type	Mie-Gruneisen
Number of particles	1,484,294
Number of elements	519,009
Simulation time	150 microseconds

Table 3.4: Tungsten long rod impact on a steel plate at 1.833 km/s

	experimental	simulation
Rod erosion	40%	37.4%
Residual velocity	1.784 km/s	1.60 km/s
Plate hole size	1.23 cm × 3.05 cm	1.67 cm (average) × 3.53 cm

Table 3.5: Comparison between experimental and simulation results

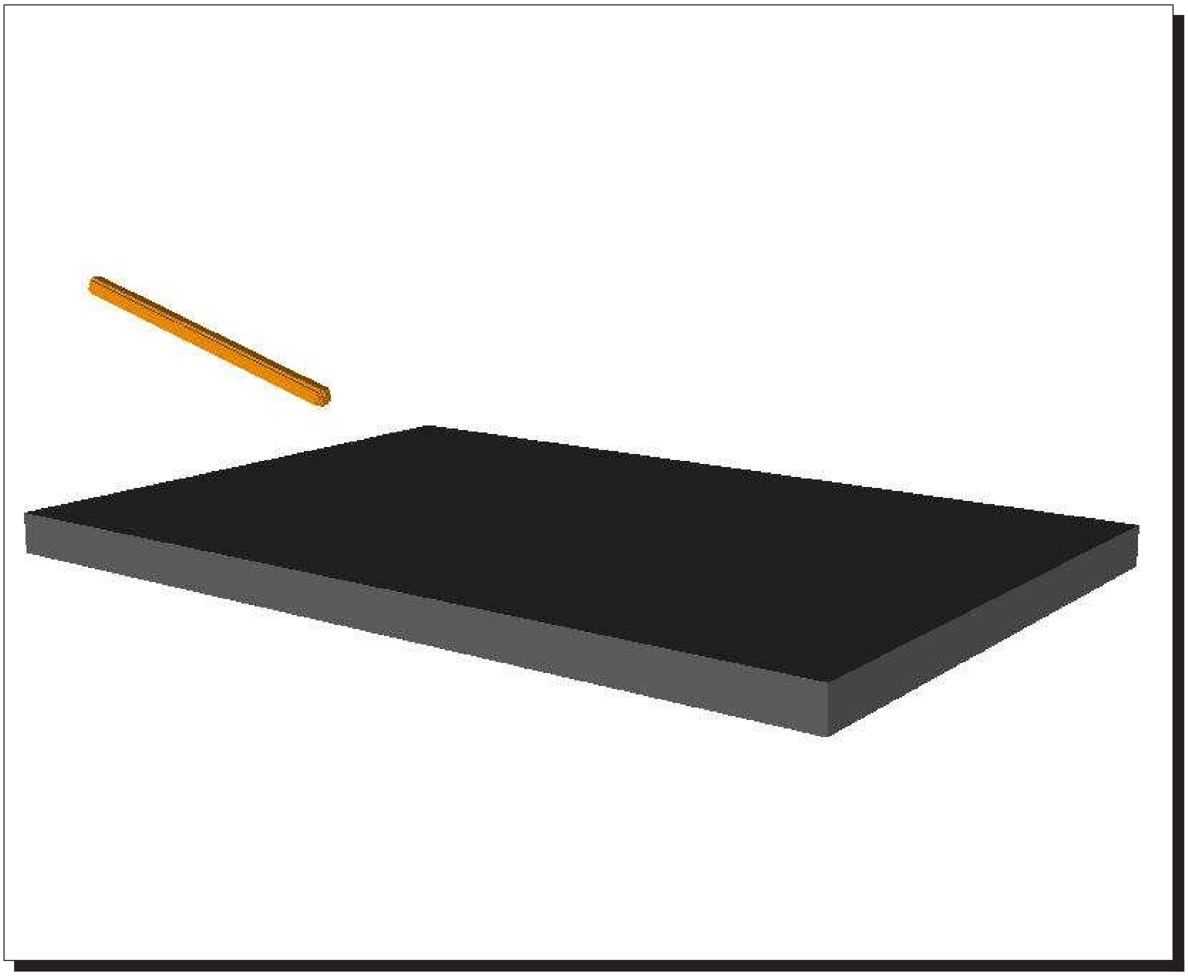

Figure 3.21: Tungsten long rod on a steel plate: initial configuration, element plot

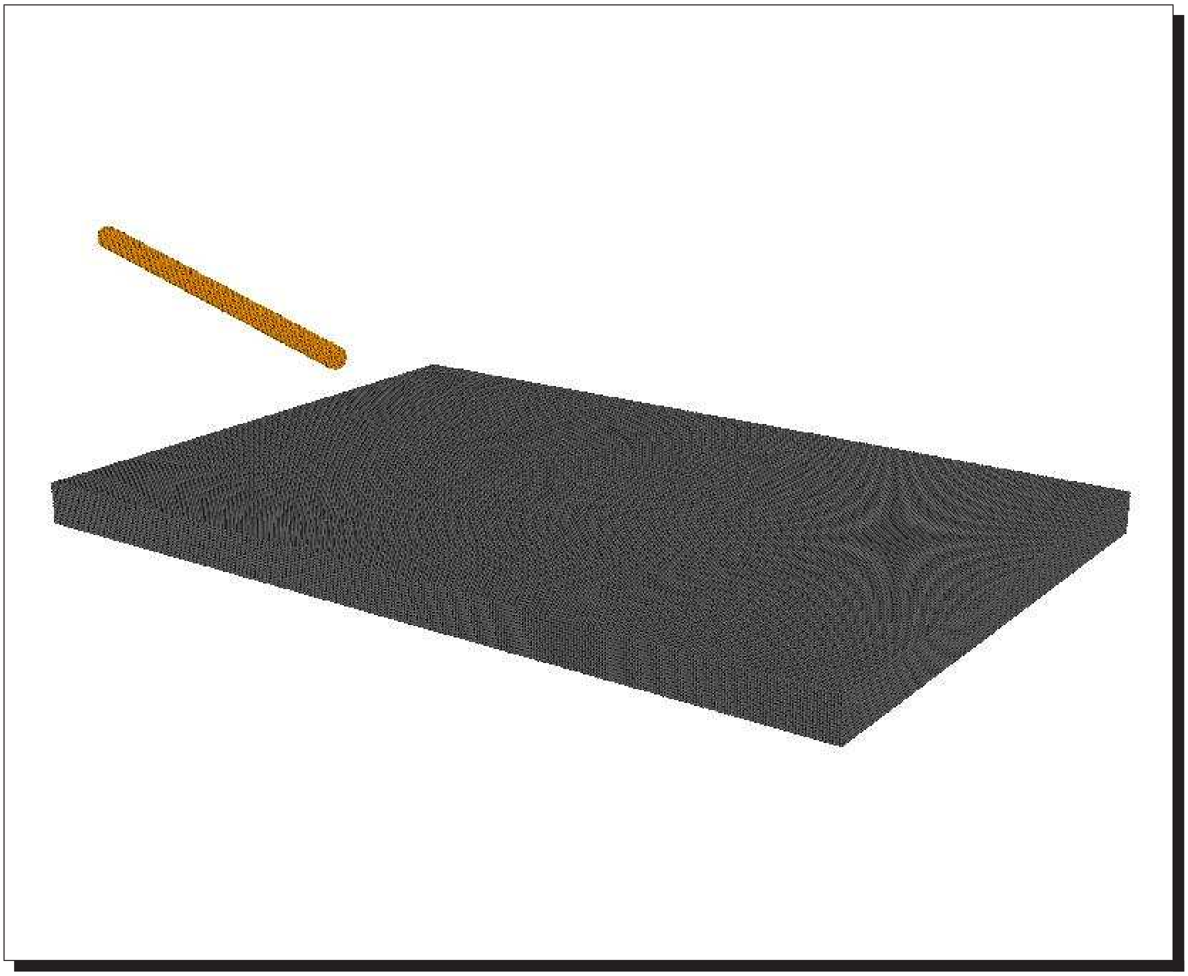

Figure 3.22: Tungsten long rod on a steel plate: initial configuration, particle plot

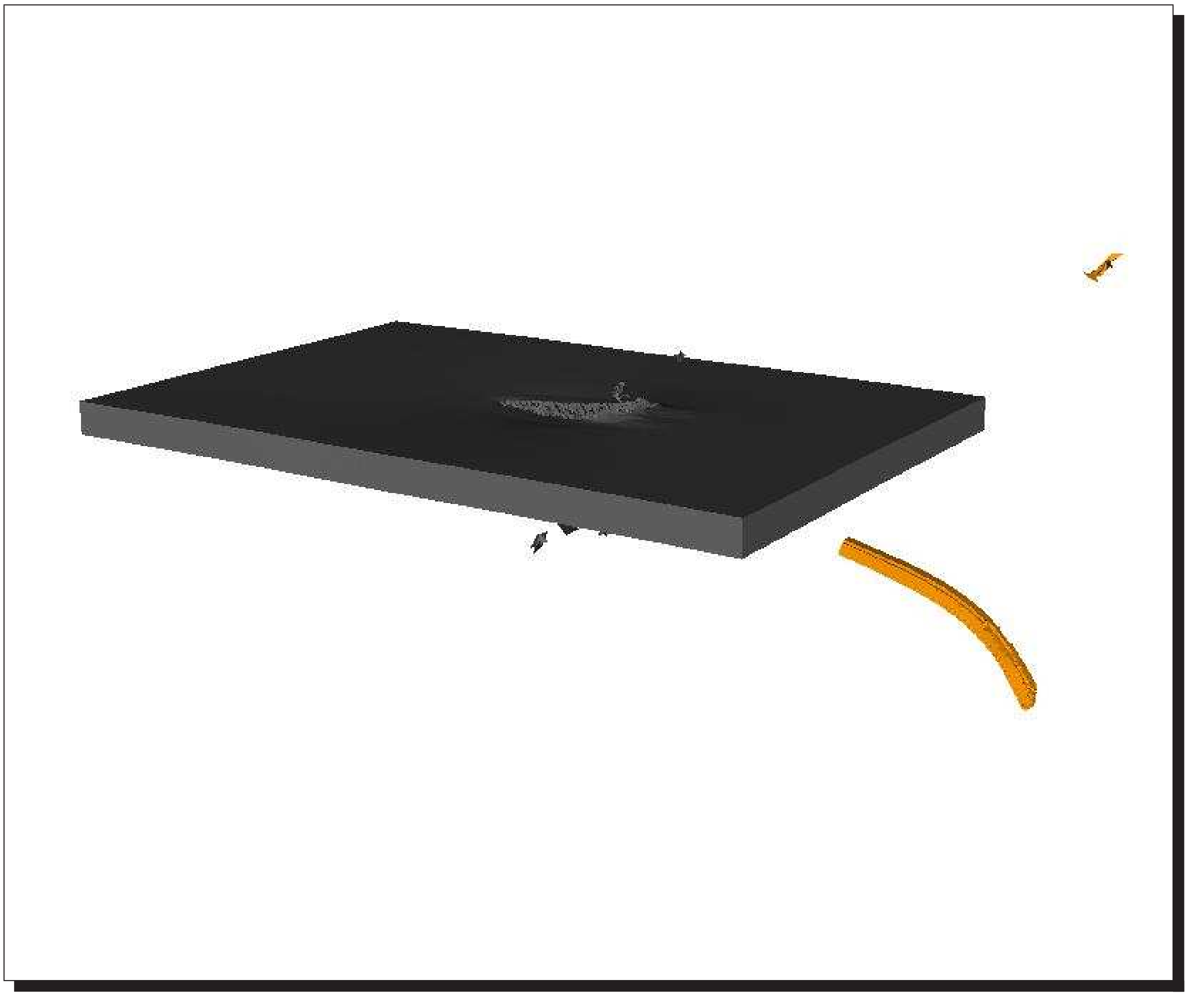

Figure 3.23: Tungsten long rod on a steel plate at $t = 150\,\mu$ secs, element plot, view 1

Figure 3.24: Tungsten long rod on a steel plate at $t = 150\,\mu$ secs, element plot, view 2

Figure 3.25: Tungsten long rod on a steel plate at $t = 150\,\mu$ secs, particle plot

Figure 3.26: Tungsten long rod on a steel plate: target at $t = 150\,\mu$ secs, element plot

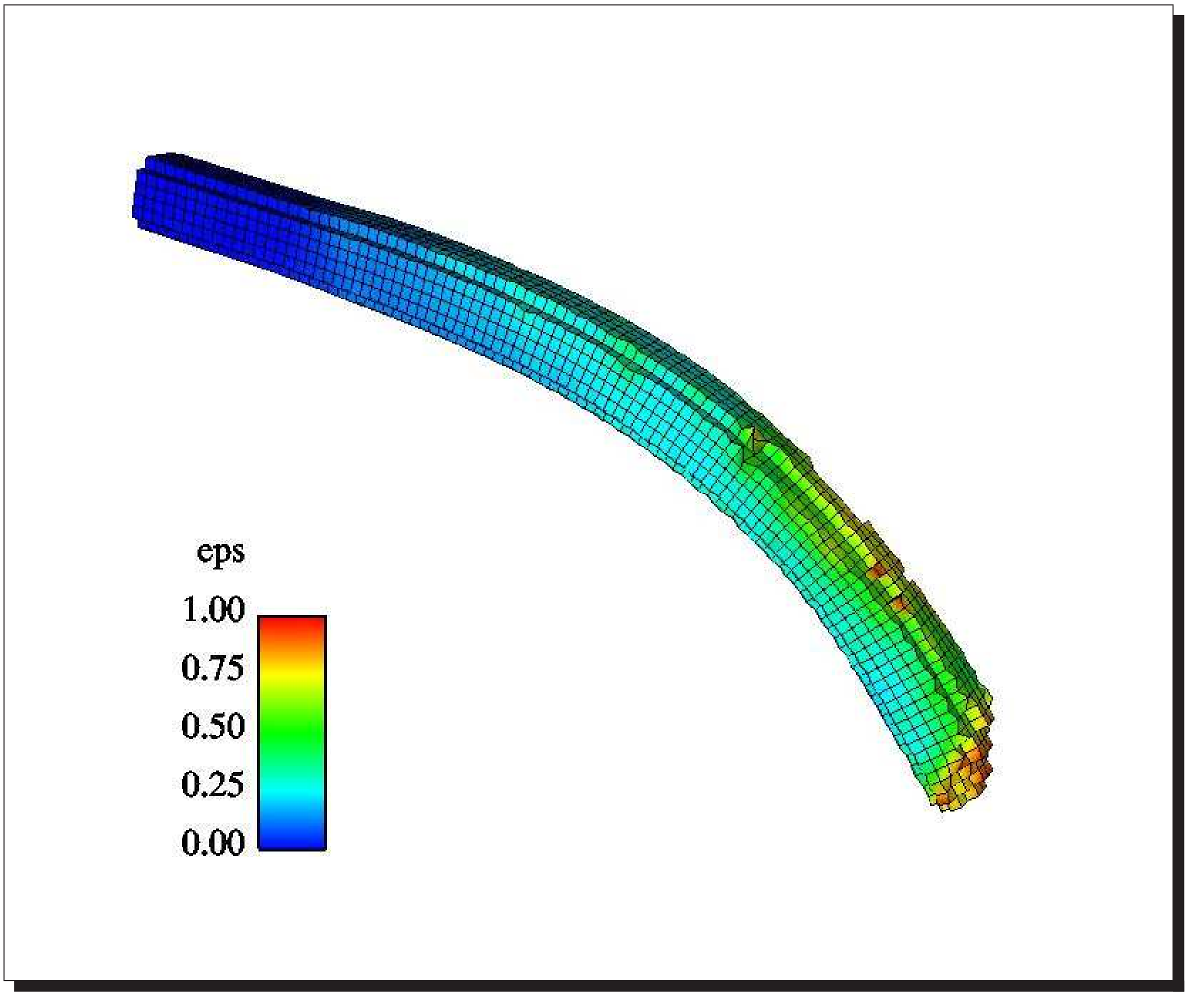

Figure 3.27: Tungsten long rod on a steel plate: projectile at $t = 150\,\mu$ secs

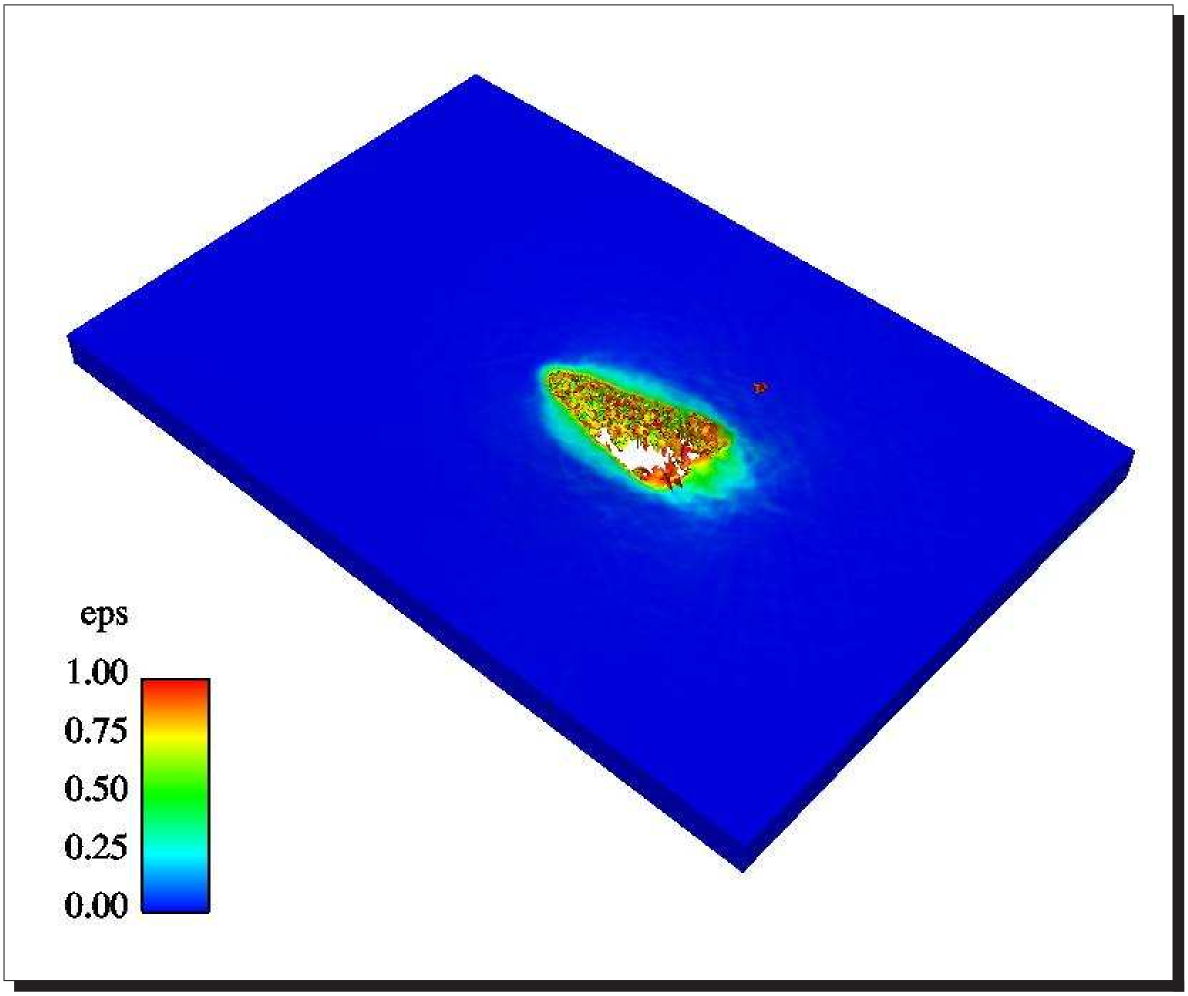

Figure 3.28: Tungsten long rod on a steel plate: target at $t = 150\,\mu$ secs, color on plastic strain

3.14.3 Simulation using ellipsoidal particles

In this section, simulation results performed using ellipsoidal particles are presented. Four simulation examples are presented. The examples of a depleted titanium long rod impact and tungsten long rod impact were described earlier, using spherical particles.

1. **EXOS simulation: Oblique sphere impact**

   The first example simulation using ellipsoidal particles involves an aluminum sphere impacting on an aluminum plate. The parameters for the simulation are shown in table (3.6). Ellipsoidal particles with aspect ratio of (2 : 2 : 1) are used for the plate. Figure (3.29) and (3.30) show the initial and final configuration. The simulation stop time is 6.6 μ secs. The simulation result is in good agreement with the experimental radiograph [59].

Simulation parameters	
Projectile diameter(sphere)	0.953 cm
Projectile velocity	6.56 km/s
Impact obliquity	45 degrees
Plate thickness	0.1143 cm
Equation of state type	Mie-Gruneisen
Number of particles	194,728
Simulation time	6.6 microseconds

Table 3.6: Oblique sphere impact

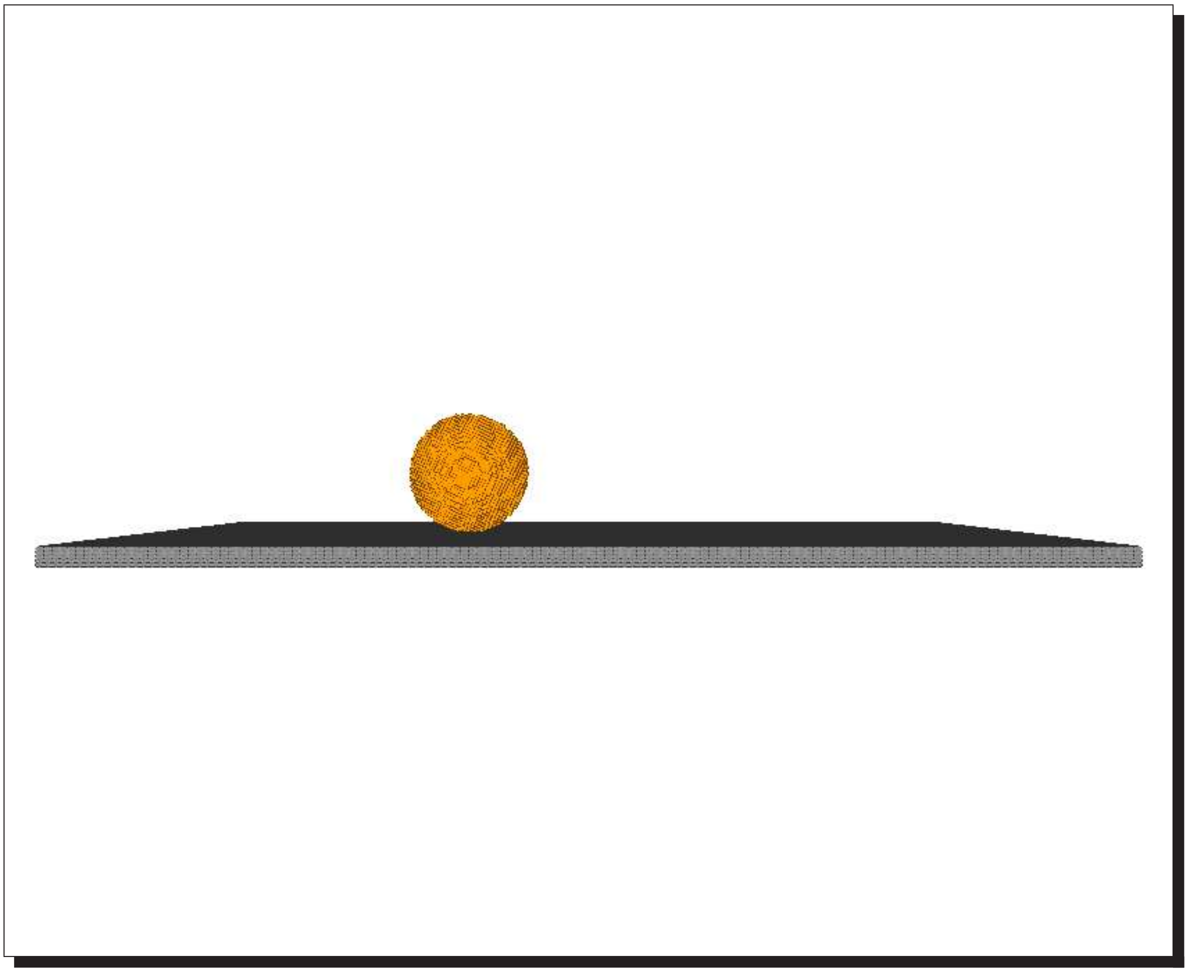

Figure 3.29: DU 0.75% Ti long rod impact on a steel plate: Initial configuration

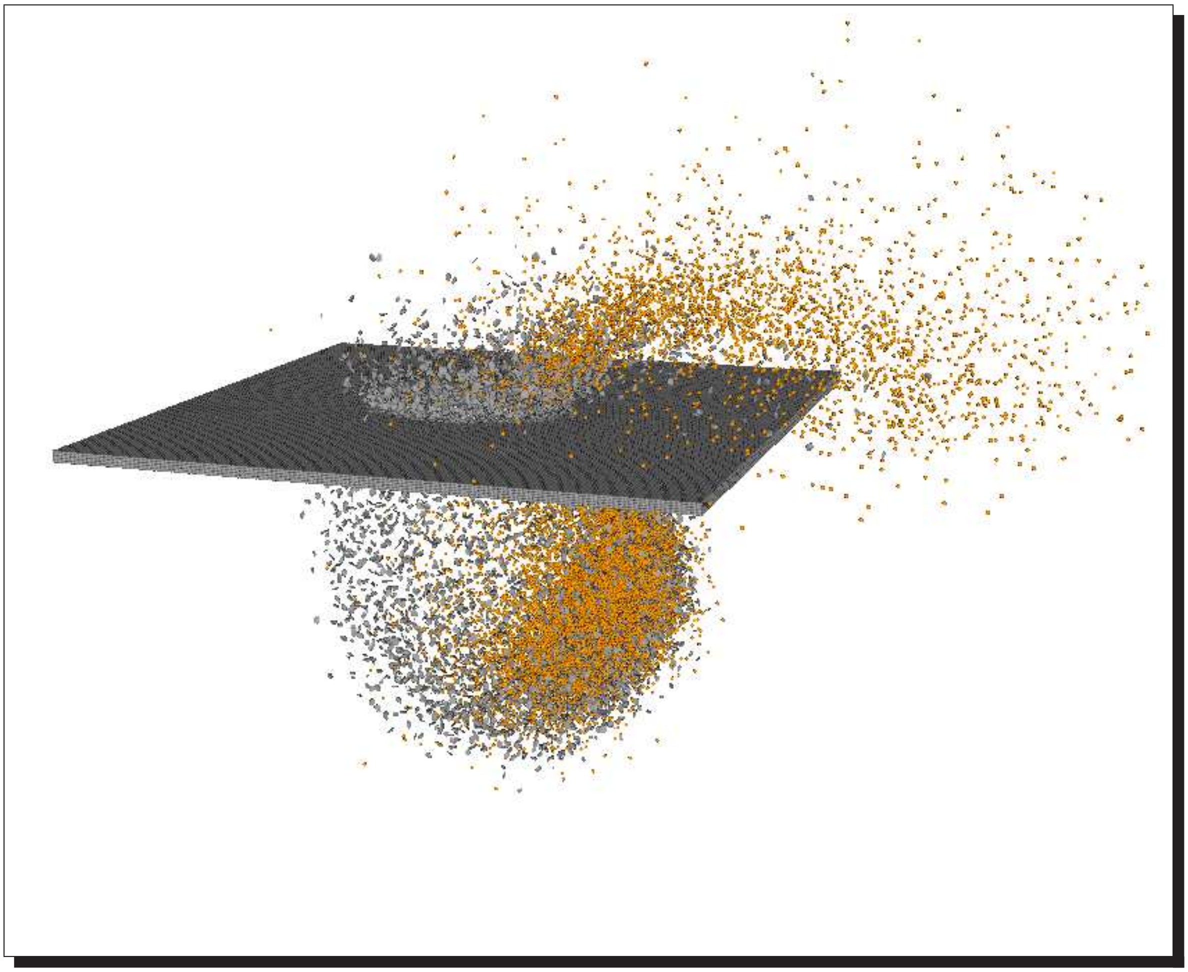

Figure 3.30: DU 0.75% Ti long rod impact on a steel plate: Initial configuration

2. **EXOS simulation: DU 0.75% Ti long rod impact on a steel plate**

In this example, simulation of a depleted uranium long rod impacting a steel plate is performed. The parameters for the simulation are shown in table (3.7). The simulation uses ellipsoidal particles with aspect ratios of (1.5 : 1.5 : 1.0) for the plate. This reduces the number of particles significantly. Note that the simulation using spherical particles required more than twice the number of particles used here. The simulation was performed for a time of 100 μ secs. Figure (3.31) shows an element plot of the initial configuration. Figure (3.32) shows a particle plot at the end of simulation, and figure (3.33) shows the element plot of the target, with color on plastic strain. The simulation results are in good agreement with the corresponding experimental data [30]. Specific comparisons include a residual rod length of 5.56 cm (simulation) versus 5.55 cm experimental. A residual velocity of 1.07 km/s for the projectile was observed in the experiment. Simulation predicted a residual velocity of 1.10 km/s. Note that these simulation results are almost identical with the results obtained using spherical particles. The memory requirements in the ellipsoidal

Simulation parameters	
Projectile diameter (DU 0.75% Ti)	0.767 cm
Projectile length (L/D = 10 cylinder)	7.67 cm
Projectile velocity	1.21 km/s
Plate velocity	0.217 km/s
Impact obliquity	73.5 degrees
Plate thickness (steel)	0.64 cm
Equation of state type	Mie-Gruneisen
Number of particles	712,929
Number of elements	253,296
Simulation time	100 microseconds
Wall clock time (16 cpus, SGI Onyx)	58.3 hours

Table 3.7: DU 0.75% Ti long rod impact on a steel plate

particle case are reduced by a factor of two, as the number of particles and elements used in the simulation were reduced by the same factor. However no significant reduction in wall clock time requirements was achieved for the ellipsoidal particle case. This is probably due to the fact that additional states are required and additional floating point computations had to be performed in the ellipsoidal particle case. These results suggest that the use of ellipsoidal particles in simulations involving flat plate targets can offer advantages on computers where simulation capabilities are memory constrained.

The current simulation used only 16 processors. The effect of ellipsoidal particles in problems run on distributed systems with much larger numbers of processors is yet to be determined.

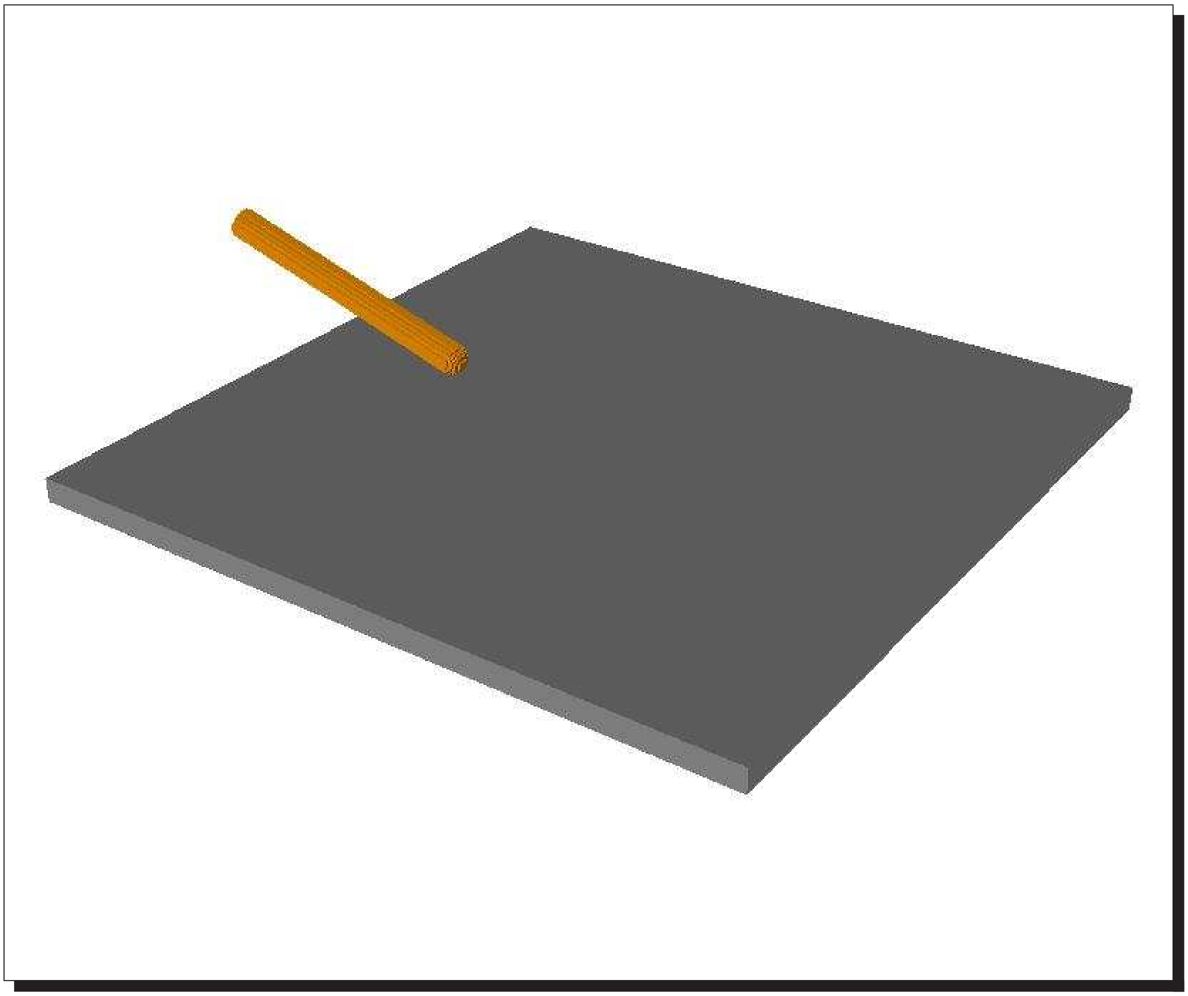

Figure 3.31: DU 0.75% Ti long rod impact on a steel plate: Initial configuration

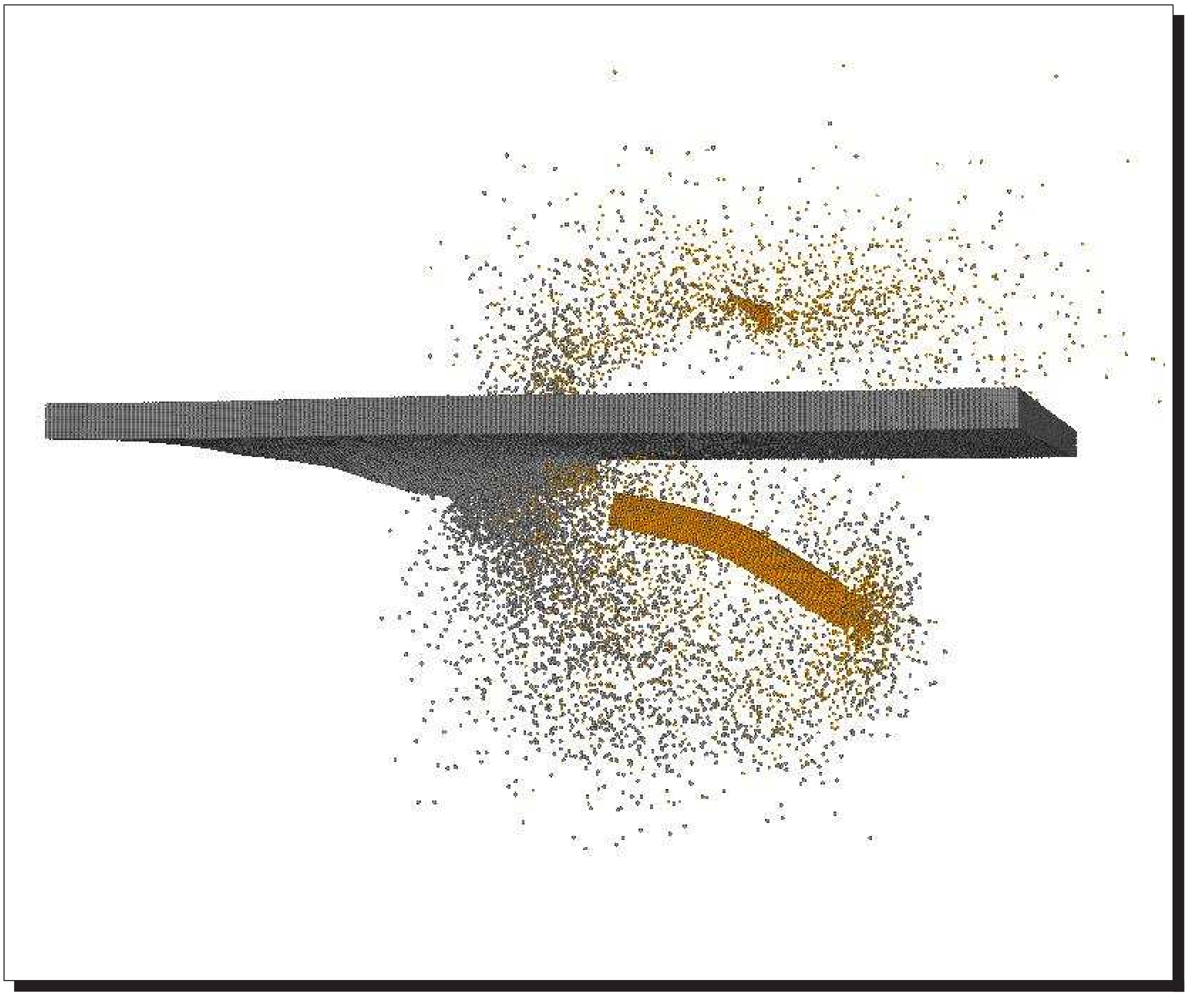

Figure 3.32: DU 0.75% Ti long rod impact on a steel plate at $t = 100\mu$ secs

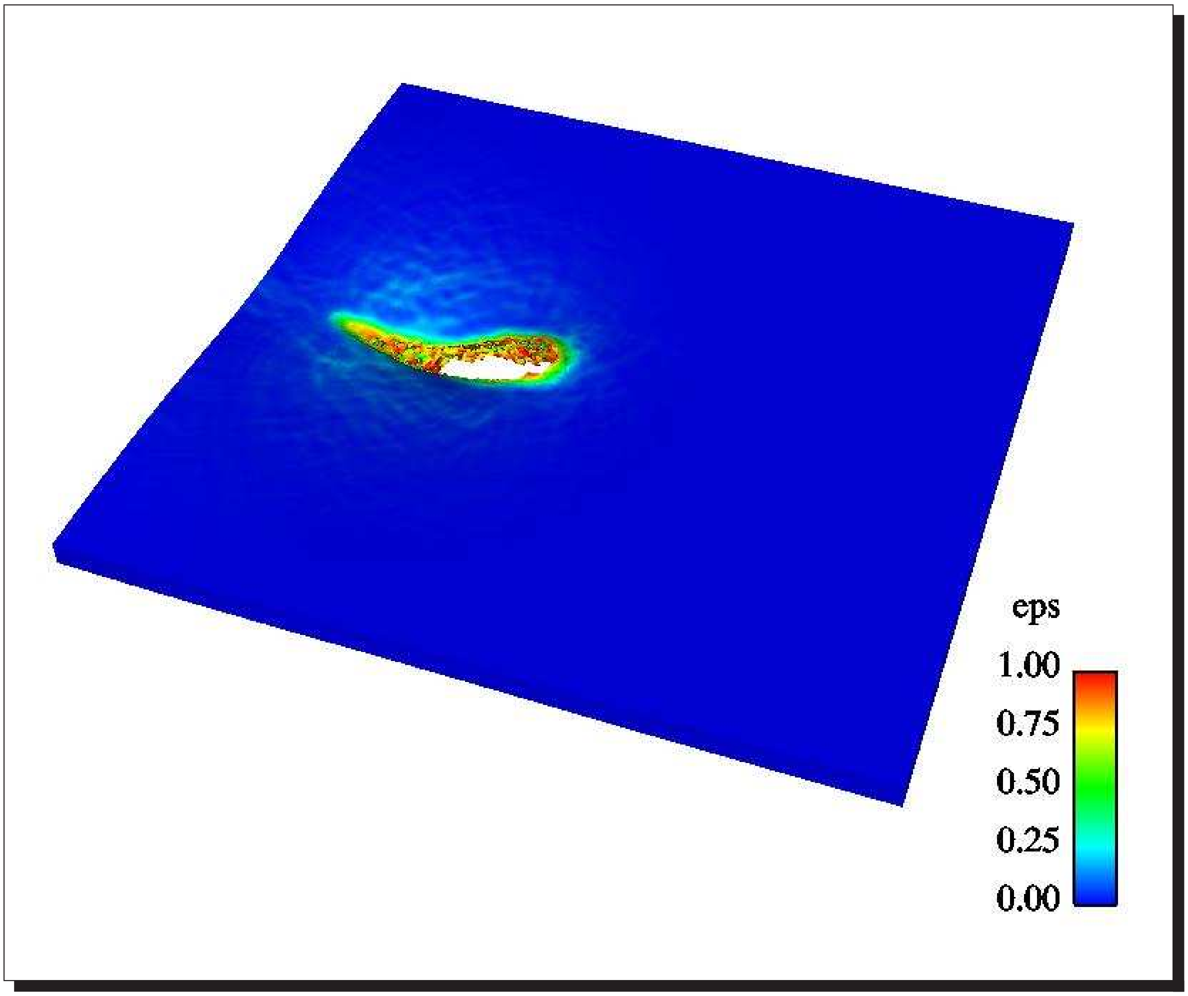

Figure 3.33: DU 0.75% Ti long rod impact on a steel plate: wall plate at $t = 100\mu$ secs, color on plastic strain

3. **EXOS simulation: Tungsten long rod impact on a steel plate at 1.833 km/s**

In this example, simulation of a tungsten long rod impacting a steel plate is performed. Note that simulation results for this problem, using spherical particles were presented earlier as example (3) of subsection (3.14.2). In this section, the simulation is performed using ellipsoidal particles with an aspect ratio of (1.5 : 1.5 : 1.0) in the plate. The simulation parameters are shown in table (3.8). Figure (3.34) shows an element plot of the initial configuration. Figures (3.35) and (3.36) show particle and element plots respectively at the end of simulation. The simulation stop time is 150 μ secs. The simulations results are in good agreement with the experimental radiograph [75]. A comparison of experimental and simulation results are presented in table (3.9)

Projectile diameter (tungsten, L/D=20 cylinder)	0.475cm
Impact velocity	1.833 km/s
Impact obliquity	75 degrees
Plate thickness (steel)	0.95 cm
Equation of state type	Mie-Gruneisen
Number of particles	671,176
Number of elements	235,389
Simulation time	150 microseconds
Number of processors (average)	12.45
Wall clock time (SGI Onyx)	87.06 hours

Table 3.8: Tungsten long rod impact on a steel plate at 1.833 km/s

	experimental	simulation
Rod erosion	40%	37.9%
Residual velocity	1.784 km/s	1.60 km/s
Plate hole size	1.23 cm × 3.05 cm	1.84 cm (average) × 3.36 cm

Table 3.9: Comparison between experimental and simulation results

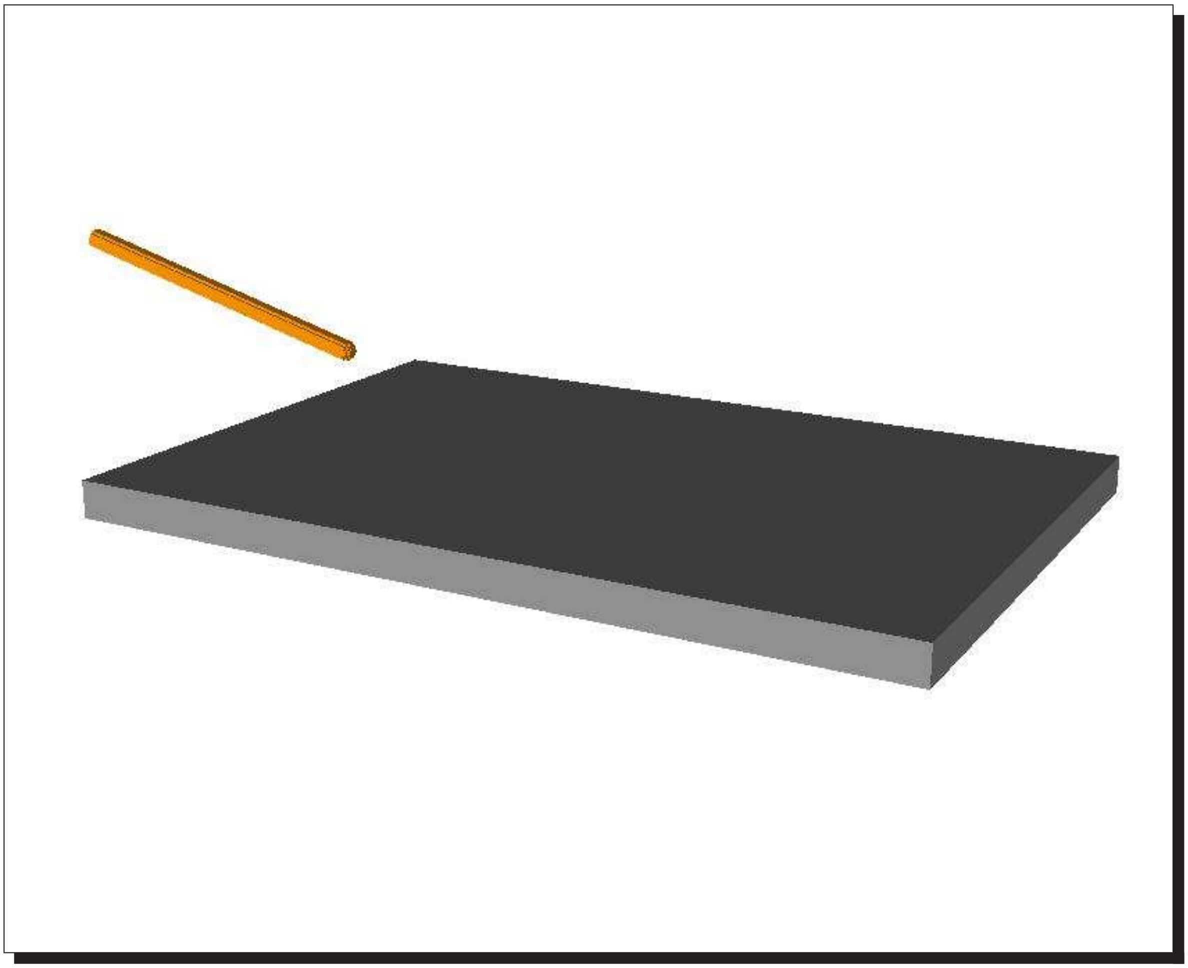

Figure 3.34: Tungsten long rod on a steel plate: initial configuration, element plot

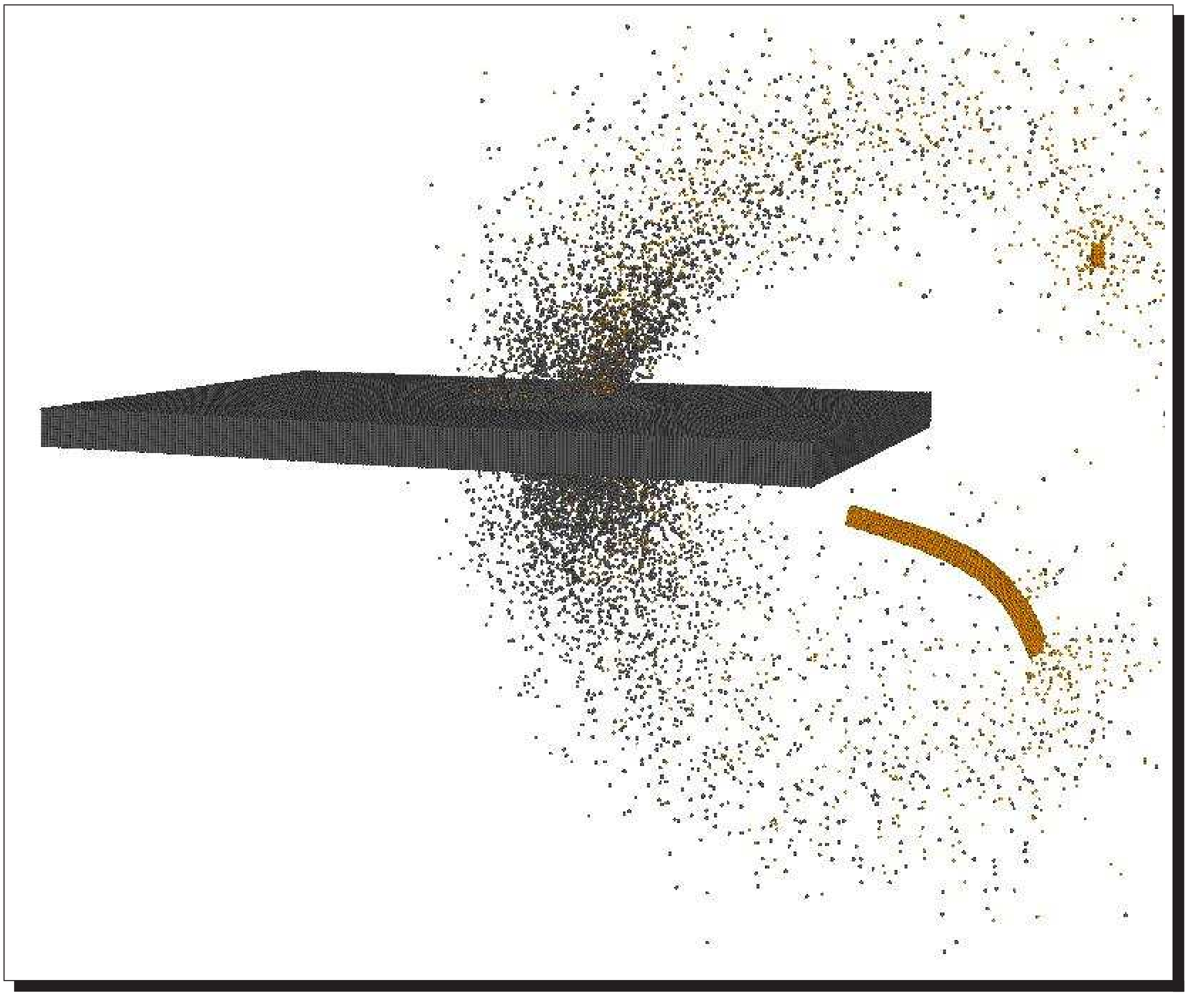

Figure 3.35: Tungsten long rod on a steel plate at $t = 150\mu$ secs, particle plot

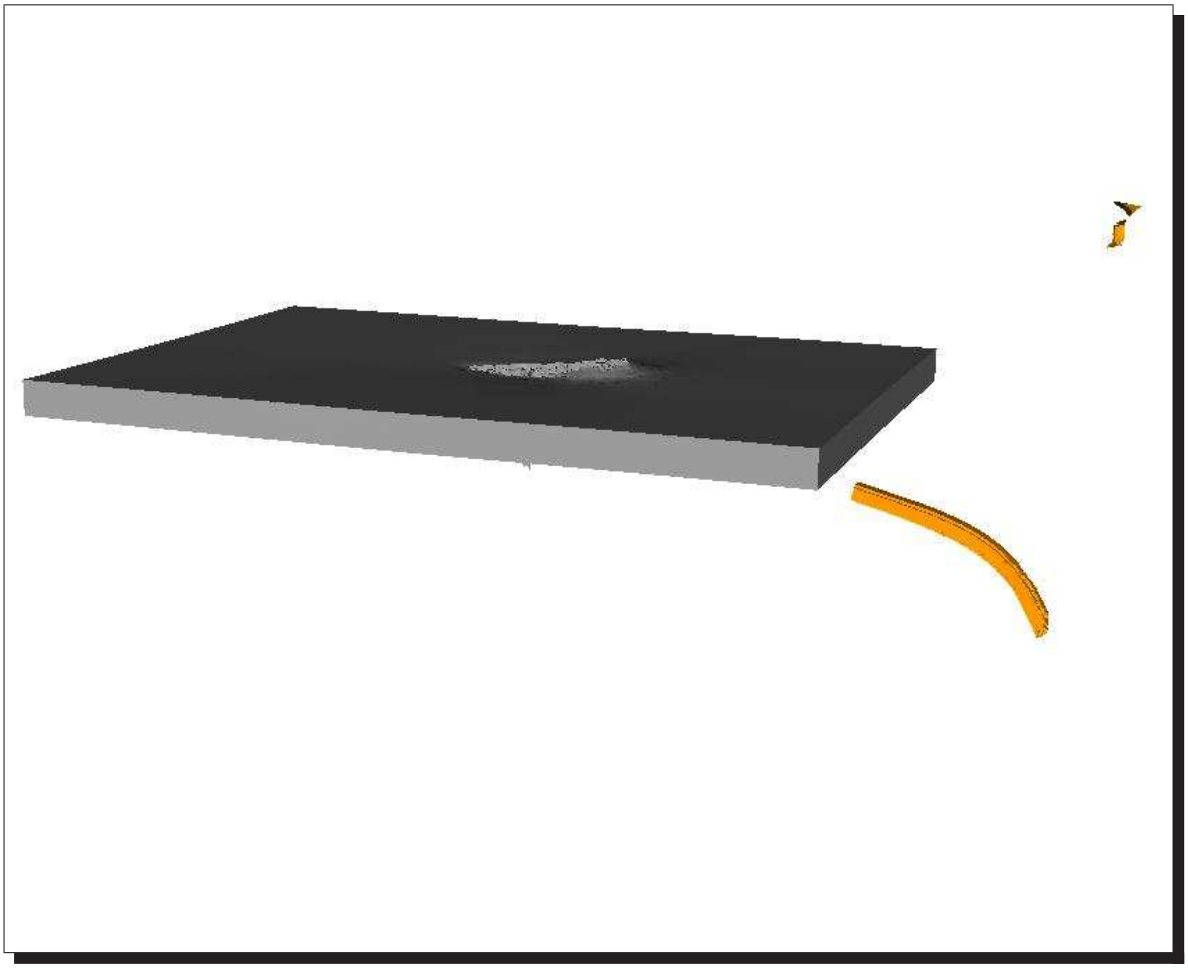

Figure 3.36: Tungsten long rod on a steel plate at $t = 150\mu$ secs, element plot

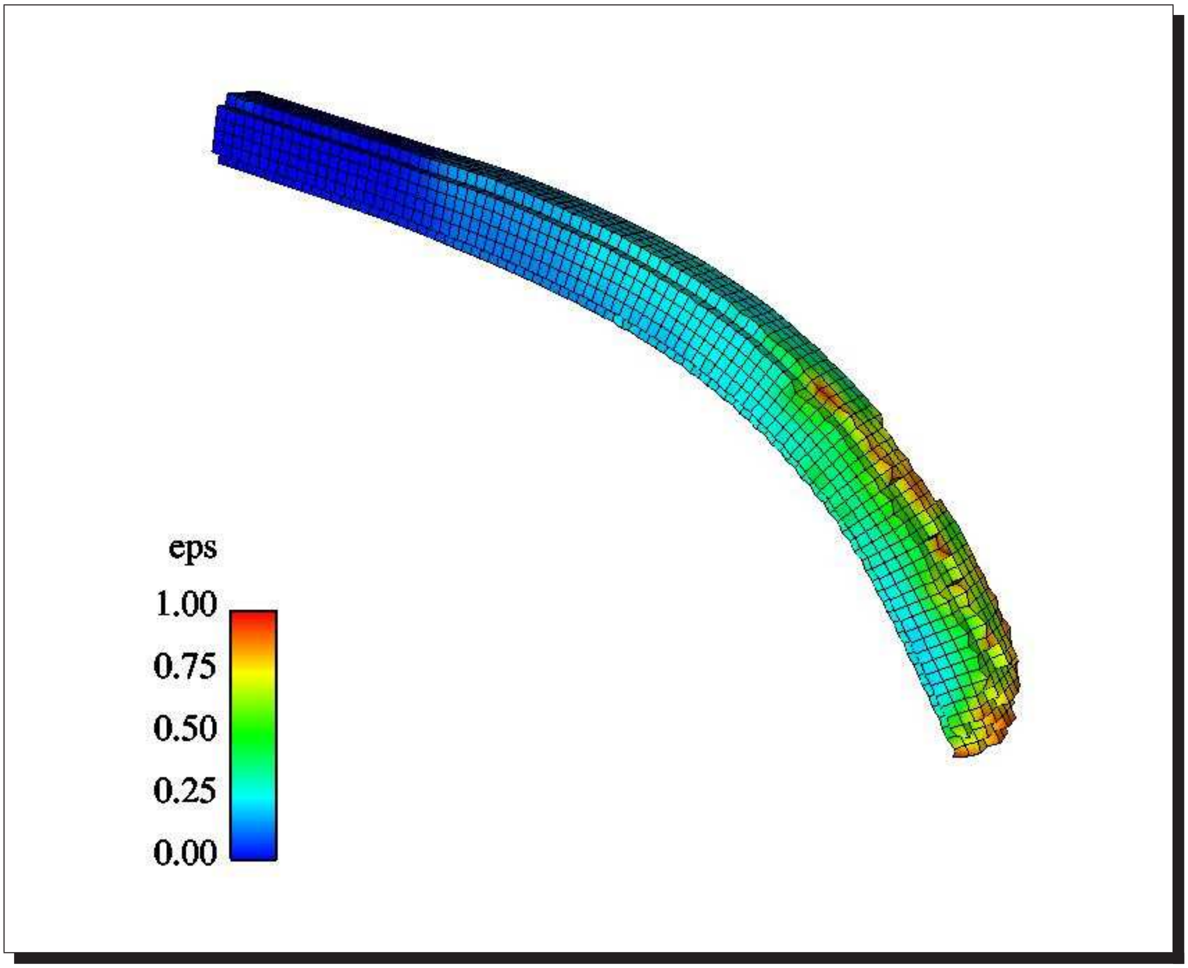

Figure 3.37: Tungsten long rod on a steel plate: projectile at $t = 150\mu$ secs

4. **EXOS simulation: Whipple shield impact, inhibited shaped charge projectile (SWRI test number 7139-19)**

In this example problem, simulation of the impact of an inhibited shape charge projectile on a Whipple shield is performed. This problem was run as a test case for ellipsoidal particles. A (1.5:1.5:1.0) aspect ratio was chosen for the particles. The simulation parameters are shown in table (3.10). Figure (3.38) shows an element plot of the initial configuration, while figures (3.39) and (3.40) show the particle and element plots respectively at the end of simulation. The simulation was run for 30.2 μ secs. The simulation used only one element across the shield plate and 10 elements across the wall plate. The wall plate dimensions are approximately 25×25cm. The simulation predicted a wall plate hole dimension of 72×62mm, versus 60×20mm observed in the experiment [27] [26]. This coarse model seems to overpredict the wall damage. Moreover, the model used a Mie-Gruniesen equation of state, which might not

Simulation Parameters	
Projectile mass (aluminum cylinder)	1.38 g
Projectile length-to-diameter ratio	1.4
Projectile pitch	0.0 degrees
Projectile yaw	9.4 degrees
Bumper thickness (aluminum plate)	0.127 cm
Wall thickness (aluminum plate)	0.4826 cm
Bumper-to-wall spacing	7.62 cm
Impact velocity	11.41 km/sec
Impact obliquity	45 degrees
Equation of state type	Mie-Gruneisen
Number of particles	297,372
Simulation time	30.2 microseconds
Wall clock time	58.8 hours
Number of processors (SGI Onyx)	7

Table 3.10: Whipple shield impact, inhibited shaped charge projectile (SWRI test number 7139-19)

be appropriate at this high velocity.

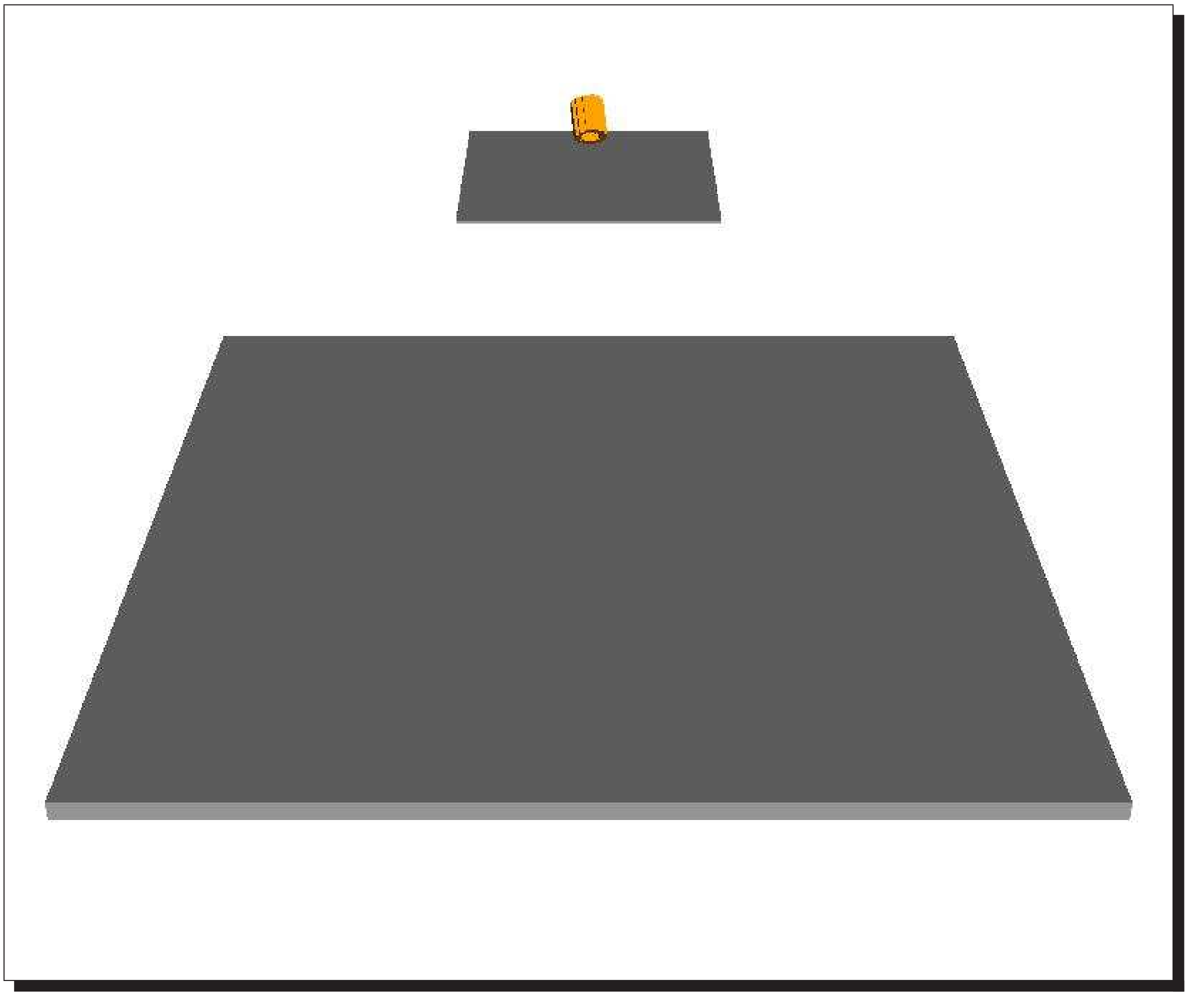

Figure 3.38: Whipple shield impact, inhibited shaped charge projectile (SWRI test number 7139-19) : initial configuration

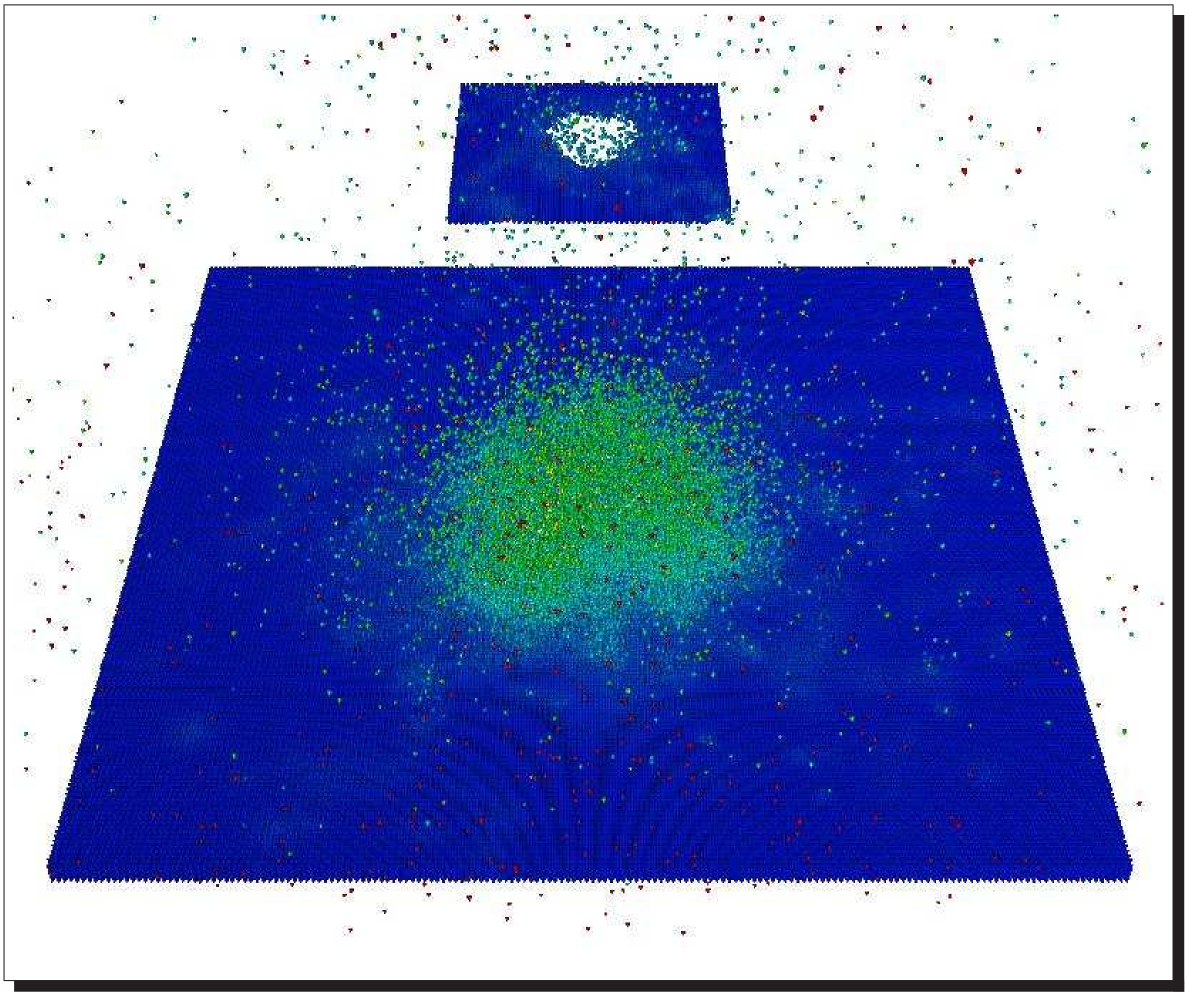

Figure 3.39: Whipple shield impact, inhibited shaped charge projectile (SWRI test number 7139-19) : wall plate at $t = 30.2\mu$ secs, particle plot

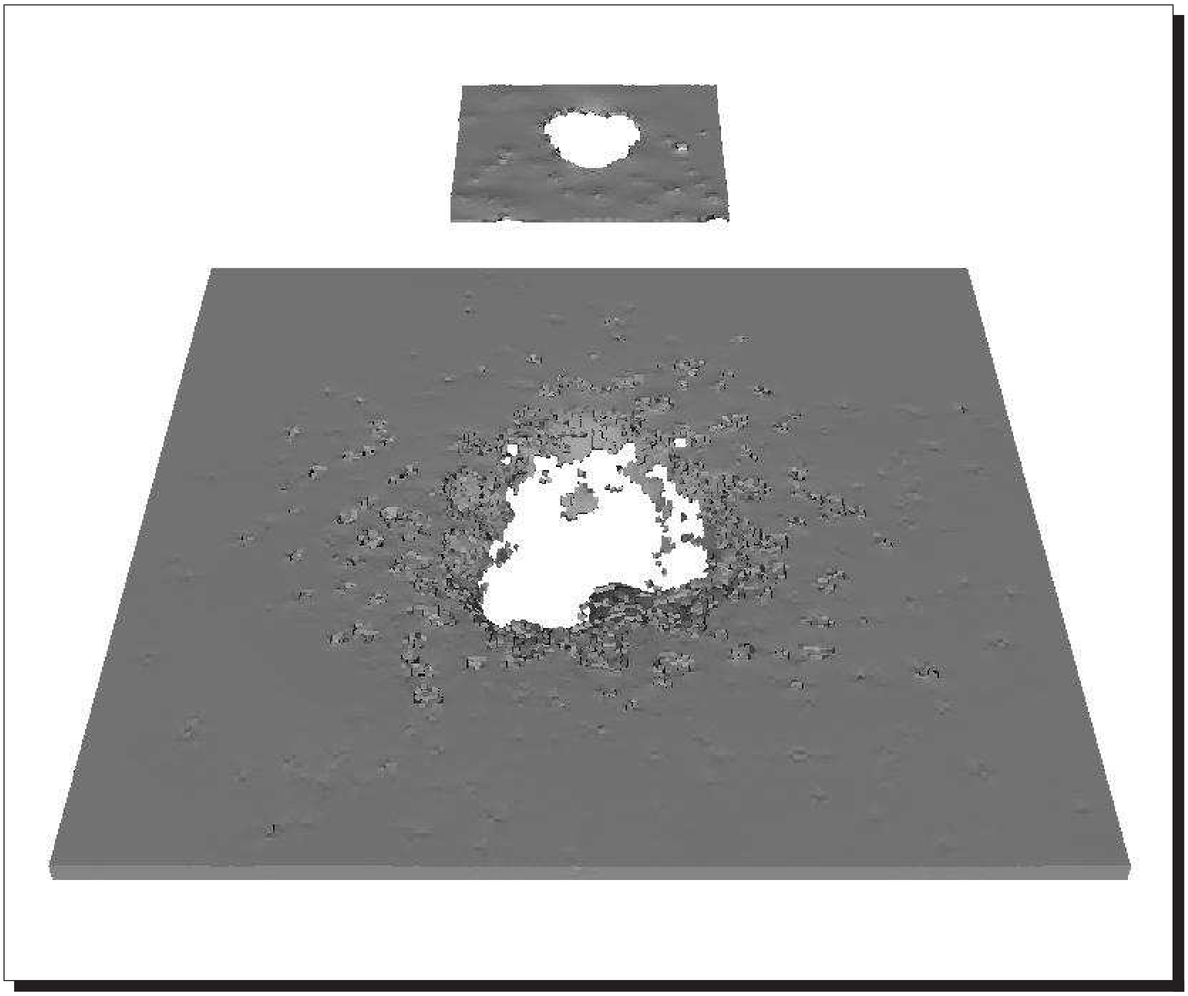

Figure 3.40: Whipple shield impact, inhibited shaped charge projectile (SWRI test number 7139-19) : wall plate at $t = 30.2\mu$ secs, element plot

3.15 Conclusions

In this chapter, a general hybrid particle-finite element method has been developed to simulate high velocity impact dynamics. The following are some of the salient features of the method.

(i) The model developed does not make use of penalty methods, diffusive grid-particle mapping schemes (like the ones used in PIC methods), and slide-line algorithms. Contact-impact is modeled using a non-dimensional kernel function.

(ii) Strength is modeled using Lagrangian finite elements. No particle-element coupling algorithm is necessary, since the finite element is embedded in the continuum, with the centers of mass of the particles serving as nodes of the finite elements.

(iii) A general particle model has been developed. This enables modeling of structures with aspect ratios (such as plates), resulting in significant savings in memory requirements.

(iv) The introduction of entropy as a state variable, in an energy based framework, provides an efficient way to couple thermal and mechanical domains and provides the framework to represent energy conservation relations.

(v) The introduction of damage models ensures a smooth transition from solid material to solid-fluid mixture, without discarding energy or mass, and without resorting to any rezoning.

Chapter 4

Advanced numerical simulations

Most recent work simulating orbital debris impact effects has employed either pure particle or mixed particle-continuum methods [29] [20] since only particle-based kinematic schemes offer both an efficient solution to the debris propagation problem and an entirely general representation of contact-impact. Work based on pure particle methods has encountered difficulties with accurate modelling of material strength effects [21], and other complications [43]. It appears that some mixed or hybrid particle-continuum method will prove most effective in meeting the need for fundamental improvements in simulation-based design of orbital debris shielding.

This chapter describes work performed to evaluate a particular new hybrid particle-continuum method [18], developed to simulate orbital debris impact problems. The numerical method is evaluated here, via simulation of a set of ISC launcher experiments, the latter conducted by Grosch [27] [26] to investigate the performance of International Space Station(ISS) shielding in oblique impacts at a velocity of eleven kilometers per second. The simulations discussed include

- Both Whipple and multi-plate shield designs

- Both aluminum and composite shielding materials and

- Both hollow cylindrical projectiles (produced by the ISC launchers) and mass equivalent spherical projectiles (for comparison to lower velocity LGG tests).

The simulations were performed using a parallel code. In addition to the simulation results, speedup data are presented for test problems run on up to 128 processors, on an Origin 2000 system operated by the Numerical Aerospace Simulation facility at NASA Ames Research Center.

4.1 Numerical method

The model used here is slightly different from the one developed in the previous chapter.

- Inertia is represented by point masses. These particles have no distributed mass moment of inertia. The particles can only translate and interact with each other thermo-mechanically. This is a special case of a more general model developed in chapter (3).

- The mass density of at a particle ' i ' is expressed as

$$\rho^{(i)} = {\rho_0}^{(i)} + \hat{\rho}^{(i)} + \tilde{\rho}^{(i)} \tag{4.1}$$

where ${\rho_0}^{(i)}$ is the constant reference density of particle 'i'.

$$\hat{\rho}^{(i)} = \sum_{\substack{j=1 \\ j \neq i}}^{n_0} {\rho_0}^{(j)} {W_0}^{(i,j)} \tag{4.2}$$

$$\tilde{\rho}^{(i)} = \sum_{\substack{j=1 \\ j \neq i}}^{n_1} {\rho_0}^{(j)} {W_1}^{(i,j)} \tag{4.3}$$

and 'n_0' is the (fixed) number of nearest neighbors of particle 'i' in the reference configuration. The number of nearest neighbors in the reference configuration in general depends on the dimension of the problem and the chosen particle packing scheme. For a body centered cubic packing scheme, it is 2^σ where $\sigma = 1, 2$ or 3, depending on the dimension of the problem. The summation in equation (4.3) is over all other particles. Thus the total number of particles in the system is

$$n = 1 + n_0 + n_1 \tag{4.4}$$

The kernel function $W_0^{(i,j)}$ in equation (4.2) is chosen to reflect exact Lagrangian kinematics under uniform compression with the fixed set of nearest neighbors.

$$W_0{}^{(i,j)} = \frac{1}{n_0}\left\{\left[\frac{\left(h^{(i)} + h^{(j)}\right)}{r_{ij}}\right]^\sigma - 1\right\} H\left[\left(h^{(i)} + h^{(j)}\right) - r_{ij}\right] \tag{4.5}$$

$$\tag{4.6}$$

In the above equation, $r_{ij} = |c^{(i)} - c^{(j)}|$ is the distance between the particle centers of mass and $h^{(i)}$ is the effective particle radius of particle 'i', which may differ from the particle radius at the reference density $h_0^{(i)}$ by a factor $\beta^{(i)}$. This allows for closed packing of particles at the reference density.

To model collisions with non-nearest neighbors, a simple linear kernel $W_1{}^{(i,j)}$ is chosen.

$$W_1^{(i,j)} = \left[\frac{\alpha^{(j)}}{\beta^{(j)\sigma}}\right]\left\{1 - \frac{r_{ij}}{2h^{(j)}}\right\} H\left[2h^{(j)}\left(\frac{\rho_0{}^{(i)}}{\left(\rho_0{}^{(i)} + \hat{\rho}^{(i)}\right)}\right)^{\frac{1}{\sigma}} - r_{ij}\right] \tag{4.7}$$

where α is determined by forcing the kernel $W_1{}^{(i,j)}$ to satisfy the following relation

$$m^{(i)} \quad = \quad \rho_0^{(i)} \int_V W_1{}^{(i)} \left(\mathbf{x} - \mathbf{c}^{(i)}, 2h^{(i)} \right) dV \tag{4.8}$$

For three dimensional calculations, $\alpha^{(j)} = \frac{1}{2}$. Note that the argument in the step function has a dependence on the density calculation from the nearest neighbors. This ensures that a particle that is highly compressed due to the nearest neighbors set is partially screened from other collisions.

4.2 Inhibited Shape charge(ISC) Launcher Simulations

This section describes simulations of four different ISC launcher experiments, the latter performed by Grosch [27] [26] on several different debris shield configurations. All of the simulations involved a projectile velocity of slightly over eleven kilometers per second, and all but one involved a velocity vector obliquity of 45 degrees. The ISC projectiles were hollow aluminum cylinders with a length-to-diameter ratio less than two, and had a mass of approximately one gram. Since the projectile description was obtained from flash radiograph measurements, there is some uncertainty in the projectile mass and geometry data.

In general the ISC projectiles exhibited both pitch and yaw with respect to the velocity vector, hence all of the simulations reported here are fully three dimensional. The models were composed of 100,000-500,000 particles and required as much as four days to simulate 30-50 microseconds in physical time. The models were run in parallel on either 7 processors of an SGI Onyx or 32 processors of an SGI Origin, requiring up to 1GB of RAM. Computer resource constraints of course placed limits on the simulation times and the spatial resolutions of the models. Note that reducing the particle size by a factor of two would require a factor of eight increase in the number of particles and a factor of sixteen increase in the required wall clock time.

4.2.1 Material properties

The simulated experiments are described in detail by Grosch [27] [26]. Material properties were estimated using data from Steinberg [68], [41], and Hiermaier *et al.* [32]. Material models for the composites are the subject of current research. Table (4.1) shows the material properties used in the simulations.

Material properties			
Parameter	Aluminum	Nextel	Kevlar
Equation of state type	Mie-Gruneisen	Linear	Linear
Shear modulus (Mbar)	0.271	0.164	0.100
Reference bulk density (g/cc)	2.7	0.82021	0.741084
Reference bulk modulus (Mbar)	0.7832	0.66633	0.415389
Initial yield stress (Mbar)	0.0029	0.008	0.008
Maximum yield stress (Mbar)	0.0058	0.008	0.008
Strain hardening exponent	0.1	0	0
Strain hardening modulus	125.0	0	0
Thermal softening modulus	0.5	1.0	1.0
Melt temperature (kilodegrees Kelvin)	1.22	1.22	0.70
Specific heat (Mbar-cm^3 per g-kilodegrees Kelvin)	0.00884	0.00884	0.01420
Spall stress (Mbar)	0.012	0.100	0.100
Plastic failure strain	2.0	0.2	0.2
First order numerical viscosity coefficient	0.01	0.01	0.01
Second order numerical viscosity coefficient	1.0	1.0	1.0
Numerical conduction coefficient	0.1	0.1	0.1

Table 4.1: Material properties for the example simulations

4.2.2 Whipple shield with a stand off distance 7.62 cm

The first simulation involved a 45 degree oblique impact on an aluminum Whipple shield at a standoff distance of 7.62 cm. The parameters for simulation are shown in the table (4.2).

Simulation Parameters	
SWRI Test Number	7139-19
Shield type	Al Whipple
First aluminum plate thickness (cm)	0.127
Second aluminum plate thickness (cm)	0.0
Wall plate thickness (aluminum, cm)	0.4826
Maximum standoff (cm)	7.62
Impact velocity (km/sec)	11.41
Impact obliquity (velocity vector, deg)	45
Projectile mass (aluminum, g)	1.38
Projectile length-to-diameter ratio	1.4
Projectile pitch (wrt velocity vector, deg)	0
Projectile yaw (wrt velocity vector, deg)	9.4
Number of particles	142,867
Simulation time (μsec)	46.6
Wall clock time (hours)	28.1
Average number of processors	6.9
System	Onyx

Table 4.2: Simulation parameters for Aluminum Whipple shield, stand off 7.62 cm

Figures (4.1) and (4.2) show particle plots at impact and at 46.6 microseconds after impact, while figure (4.3) shows an element plot of intact material at the simulation stop time. The simulation predicts a wall plate hole size (71 × 44 mm) somewhat greater than that observed in the experiment (60 × 20 mm).

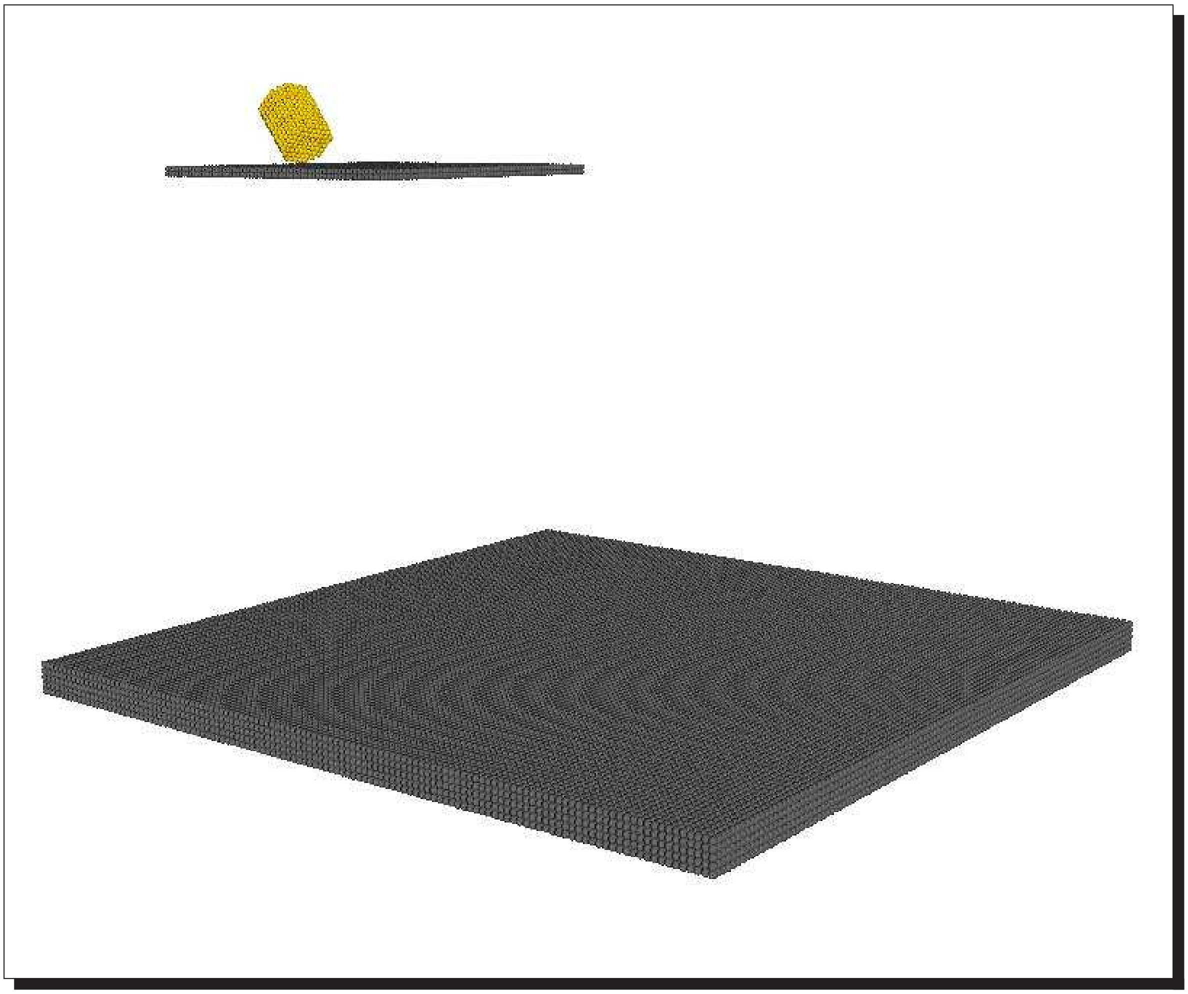

Figure 4.1: Whipple shield impact simulation: 7.62cm stand off distance, initial configuration, particle plot

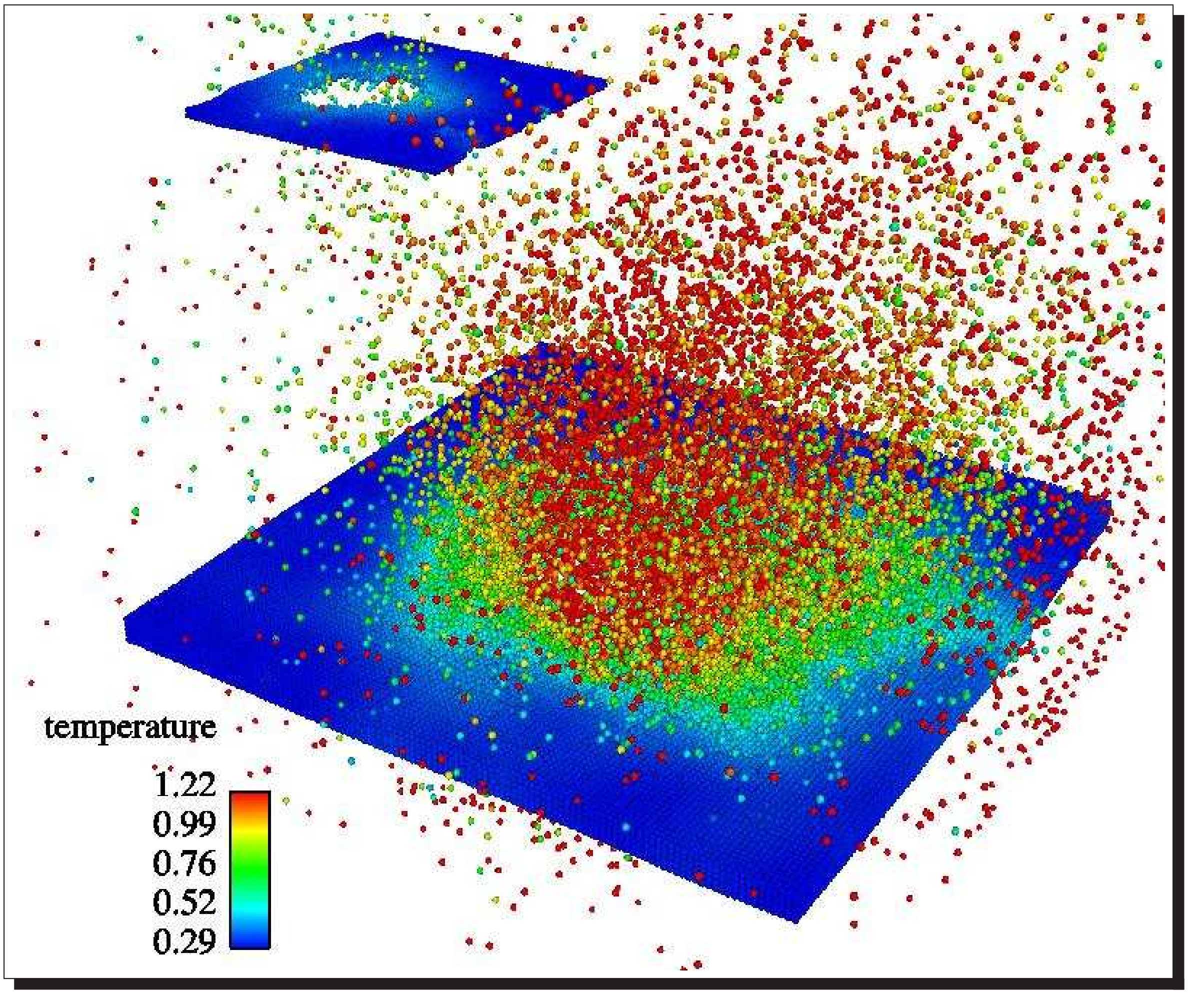

Figure 4.2: Whipple shield impact simulation: 7.62cm stand off distance, particle plot at $t = 46.6\ \mu sec$ with color on temperature

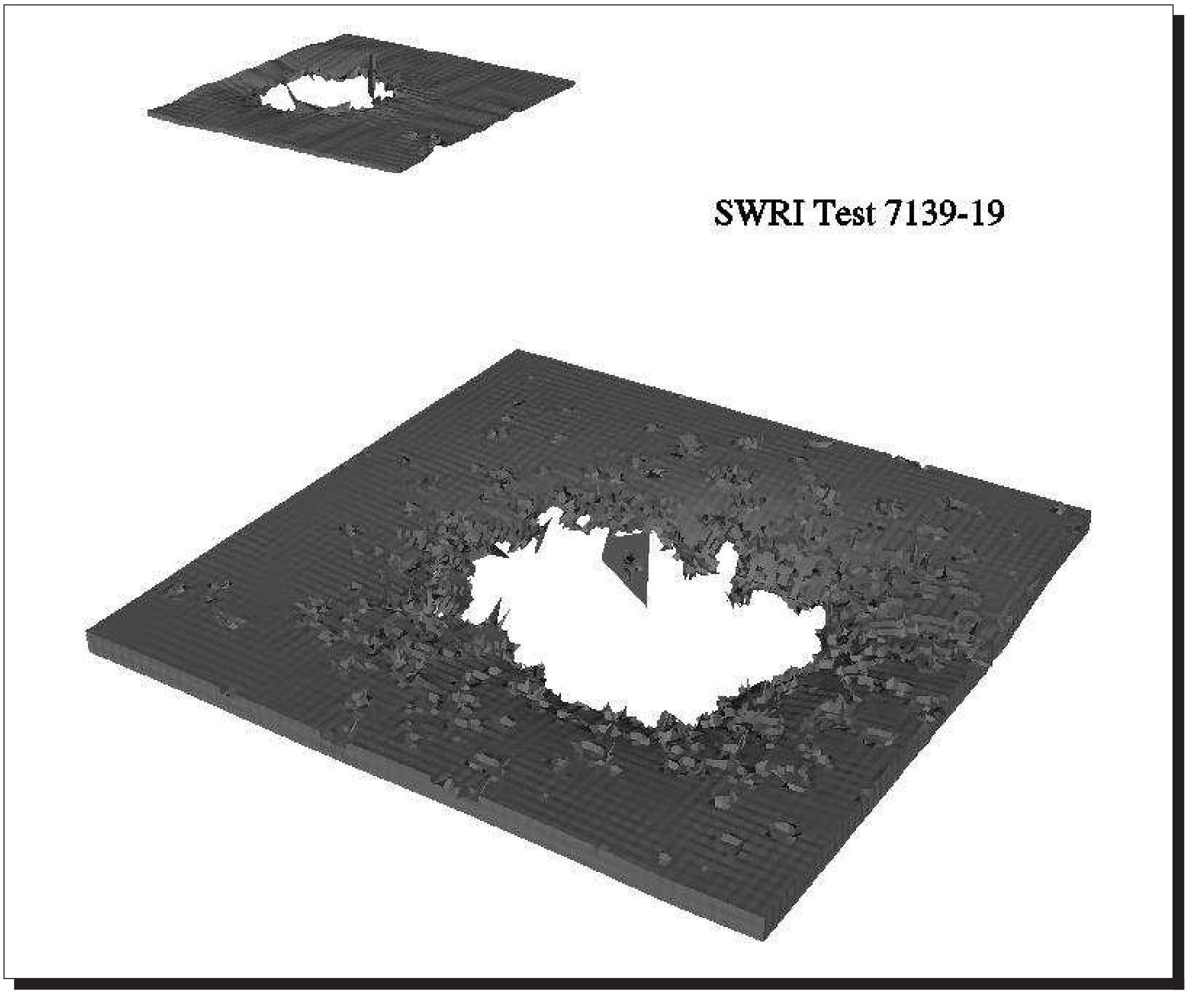

Figure 4.3: Whipple shield impact simulation: 7.62cm stand off distance, element plot at $t = 46.6\ \mu sec$

4.2.3 Whipple shield with stand off distance 11.43 cm

The second simulation involved a 45 degree oblique impact on an aluminum Whipple shield at a standoff distance of 11.43 cm. The simulation parameters are shown in table (4.3)

Simulation parameters	
SWRI Test Number	7139-22
Shield type	Al Whipple
First aluminum plate thickness (cm)	0.127
Second aluminum plate thickness (cm)	0.0
Wall plate thickness (aluminum, cm)	0.4826
Maximum standoff (cm)	11.43
Impact velocity (km/sec)	11.30
Impact obliquity (velocity vector, deg)	45
Projectile mass (aluminum, g)	0.85
Projectile length-to-diameter ratio	1.2
Projectile pitch (wrt velocity vector, deg)	11.6
Projectile yaw (wrt velocity vector, deg)	19.3
Number of particles	305,551
Simulation time (μsec)	45.0
Wall clock time (hours)	15.6
Average number of processors	32
System	Origin

Table 4.3: Simulation parameters for Aluminum Whipple shield, stand off 11.43 cm

Figures (4.4) and (4.5) show particle plots at impact and at 45.0 microseconds after impact, while Figure (4.6) shows an element plot of intact material at the simulation stop time. The simulation predicts a perforated region in the wall plate (25 × 10 mm) similar in size to the hole observed in the experiment (20 × 15 mm).

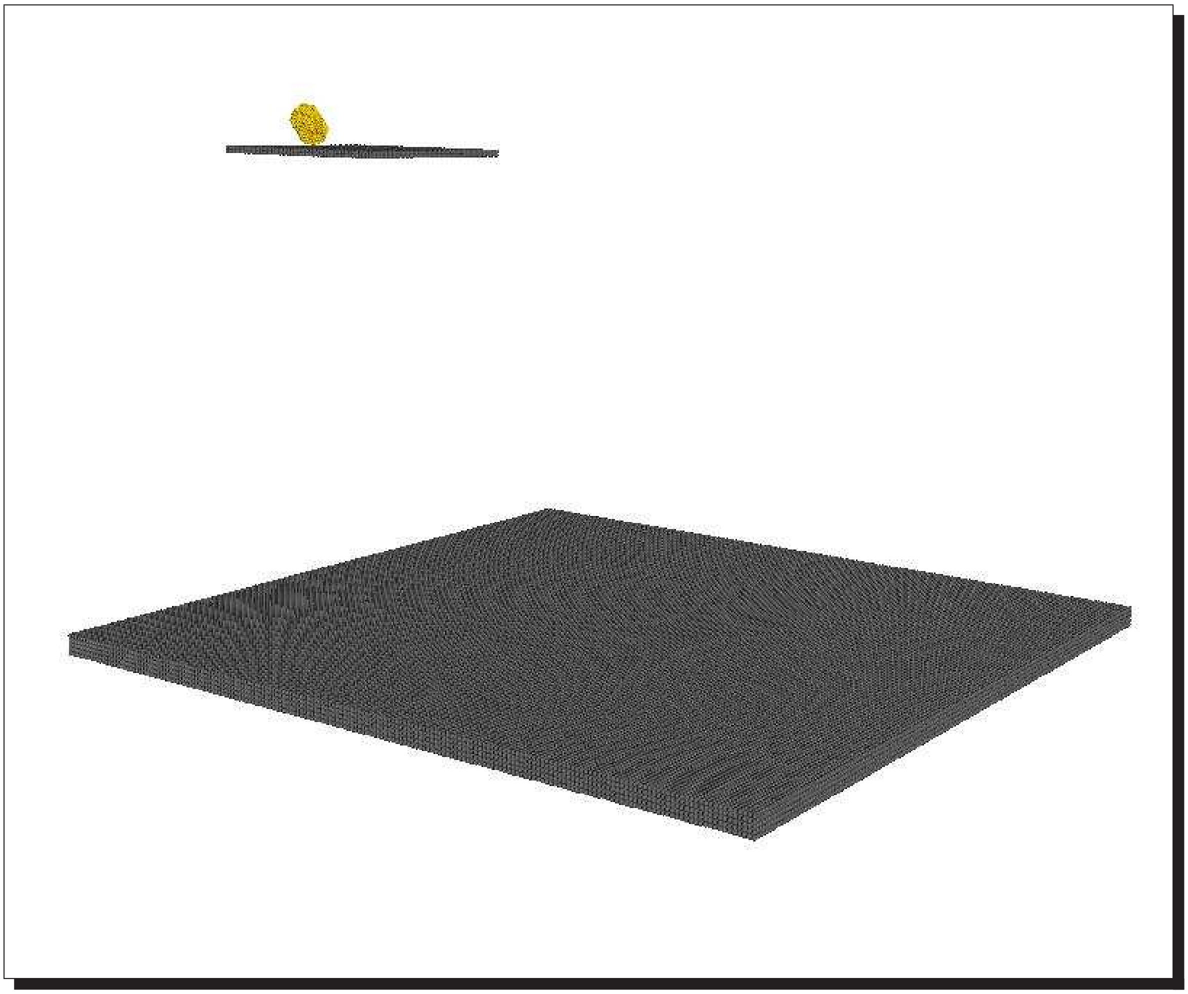

Figure 4.4: Whipple shield impact simulation: 11.43cm stand off distance, initial configuration, particle plot

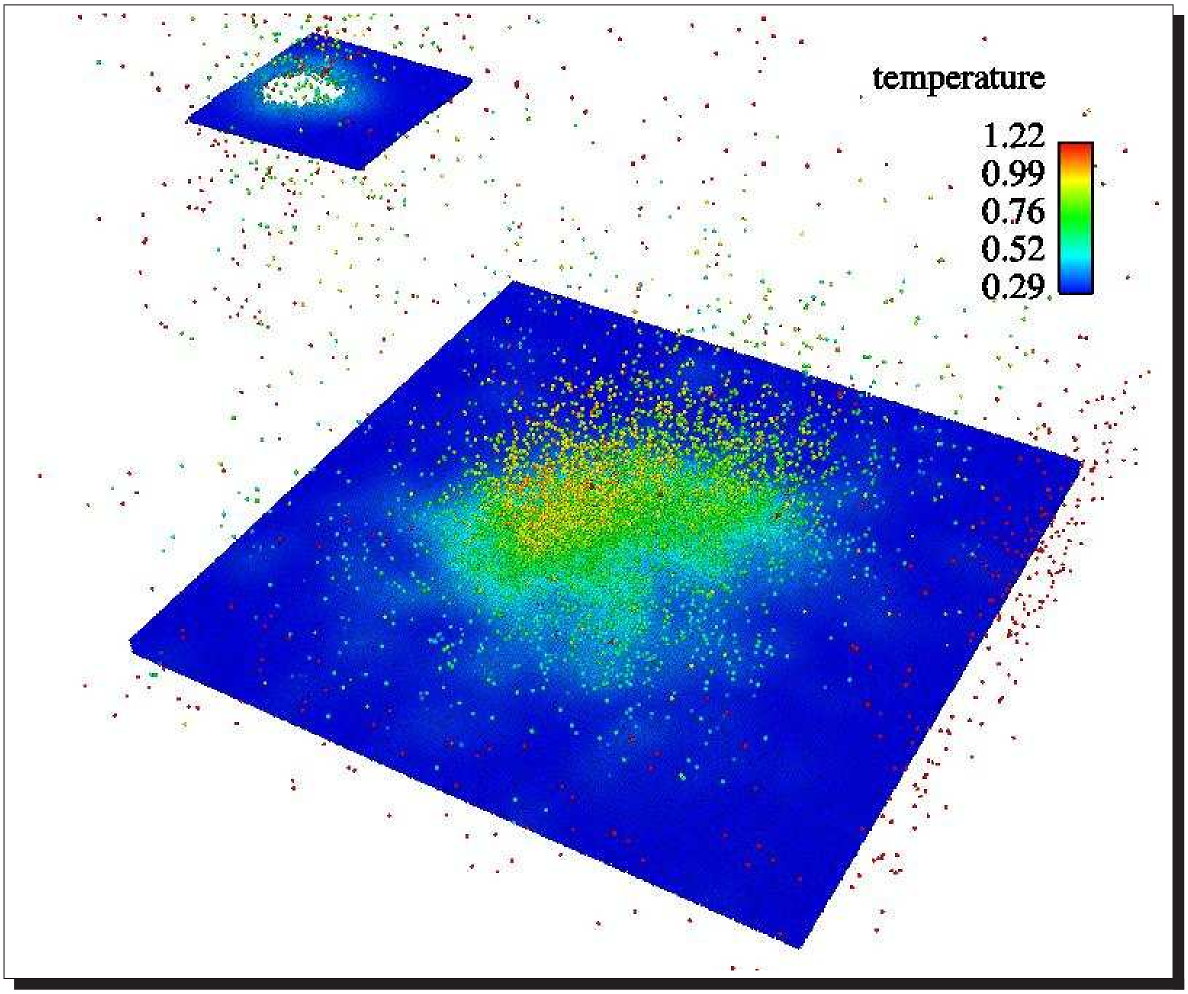

Figure 4.5: Whipple shield impact simulation: 11.43 cm stand off distance, particle plot at 45.0 μsec with color on temperature

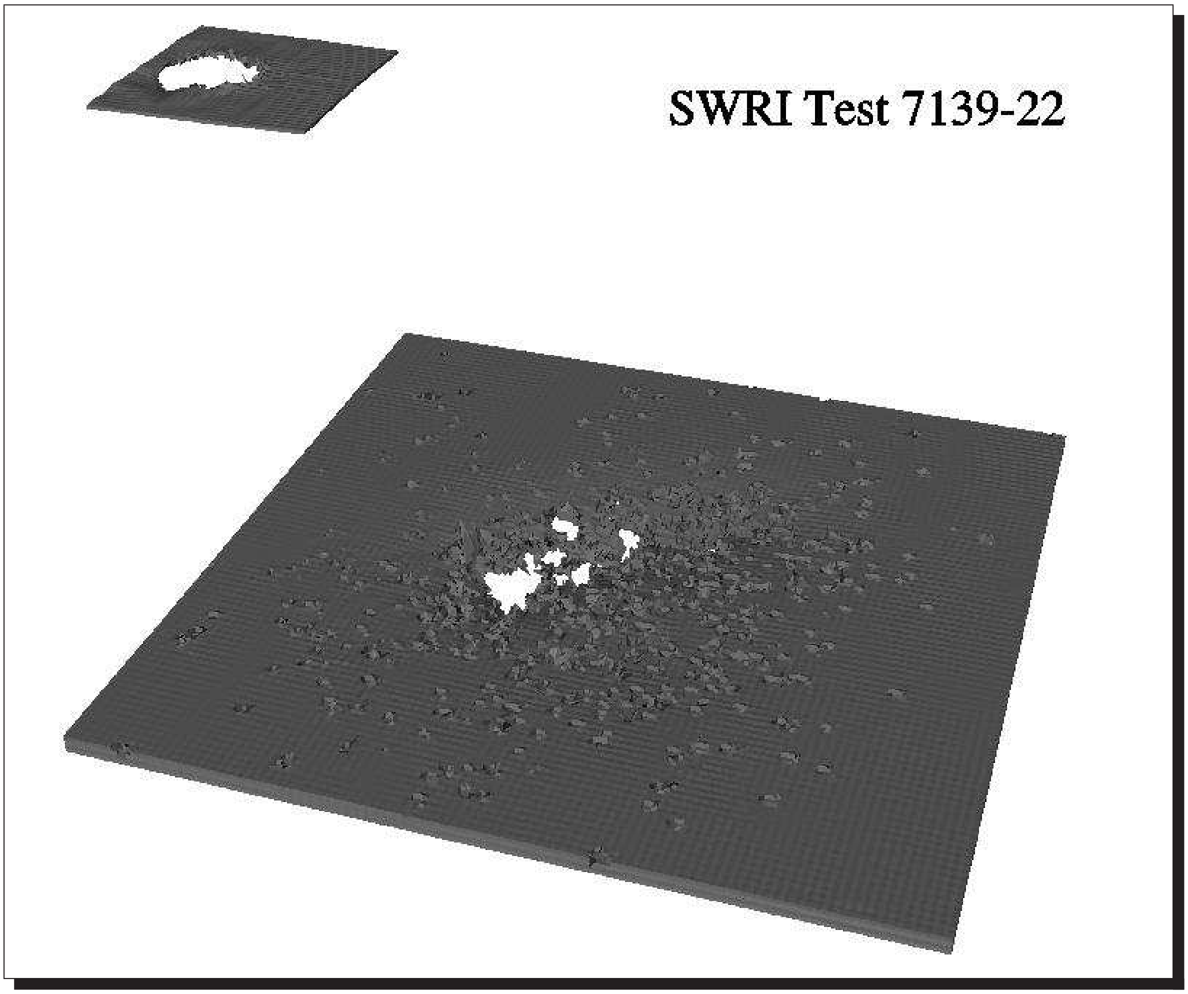

Figure 4.6: Whipple shield impact simulation: 11.43 cm stand off distance, element plot at $t = 45.0\ \mu sec$

4.2.4 Normal impact on dual plate aluminum shield

The third simulation involved a normal impact on a dual plate aluminum shield at a standoff distance of 8.636 cm. In this case the axis of the cylindrical projectile and the velocity vector were significantly misaligned, again calling for a three dimensional simulation. The simulation parameters are shown in table (4.4).

Simulation parameters	
SWRI Test Number	7139-03
Shield type	Al dual plate
First aluminum plate thickness (cm)	0.16002
Second aluminum plate thickness (cm)	0.3175
Nextel areal density (g/cm^2)	0.0
Kevlar areal density (g/cm^2)	0.0
Wall plate thickness (aluminum, cm)	0.2032
Maximum standoff (cm)	8.636
Impact velocity (km/sec)	11.16
Impact obliquity (velocity vector, deg)	0
Projectile mass (aluminum, g)	1.30
Projectile length-to-diameter ratio	1.84
Projectile pitch (wrt velocity vector, deg)	12.6
Projectile yaw (wrt velocity vector, deg)	6.9
Number of particles	265,251
Simulation time (μsec)	30.7
Wall clock time (hours)	15.6
Average number of processors	32
System	Origin

Table 4.4: Parameters for the example simulations

Figures (4.7) and (4.8) show particle plots at impact and at 30.7 microseconds after impact, while Figure (4.9) shows an element plot of intact material at the simulation stop time. The simulation predicts a wall plate hole diameter (55 mm) somewhat greater than that observed in the experiment (44 mm).

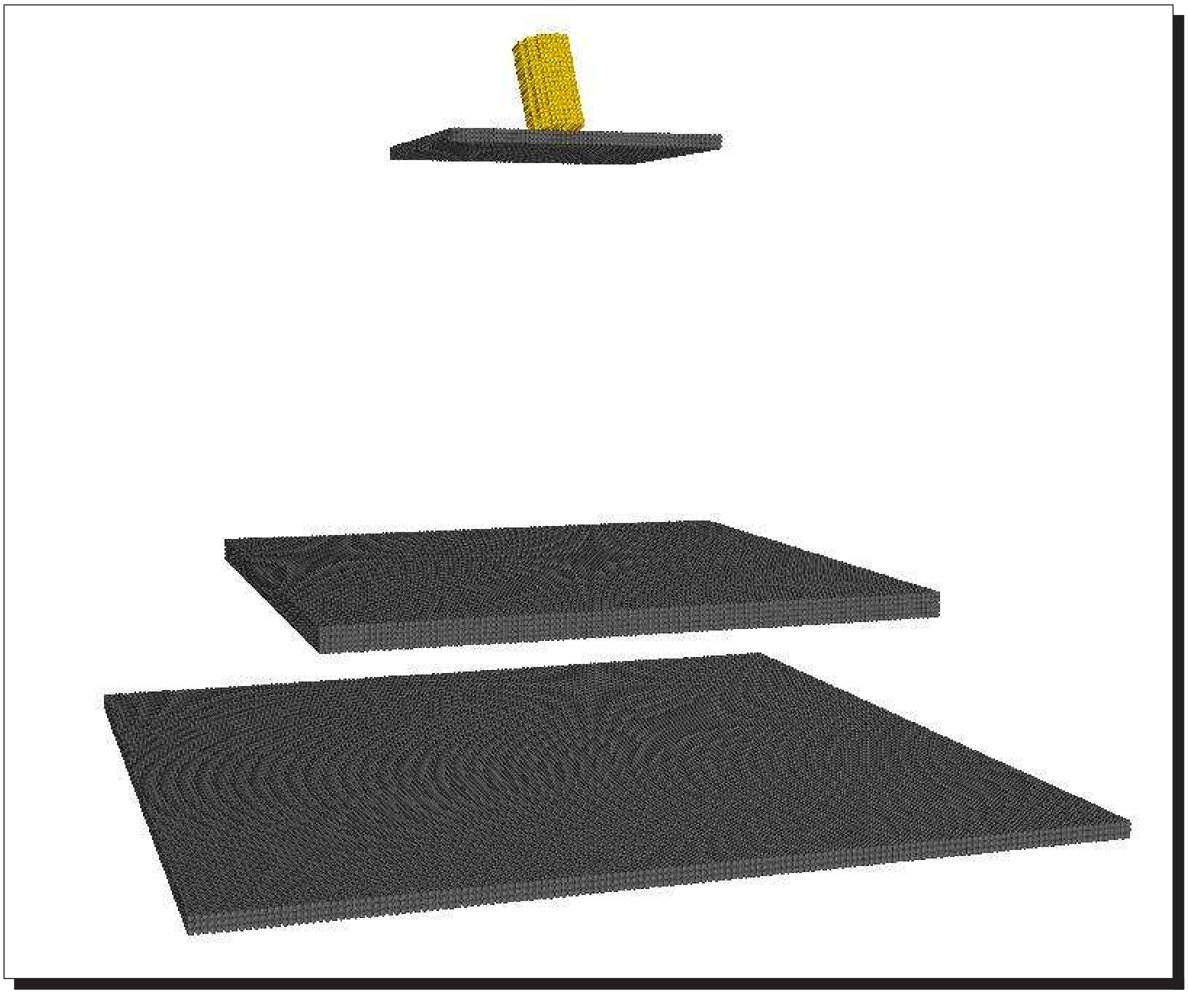

Figure 4.7: Aluminum dual plate shield: 8.636 cm stand off distance, initial configuration, particle plot

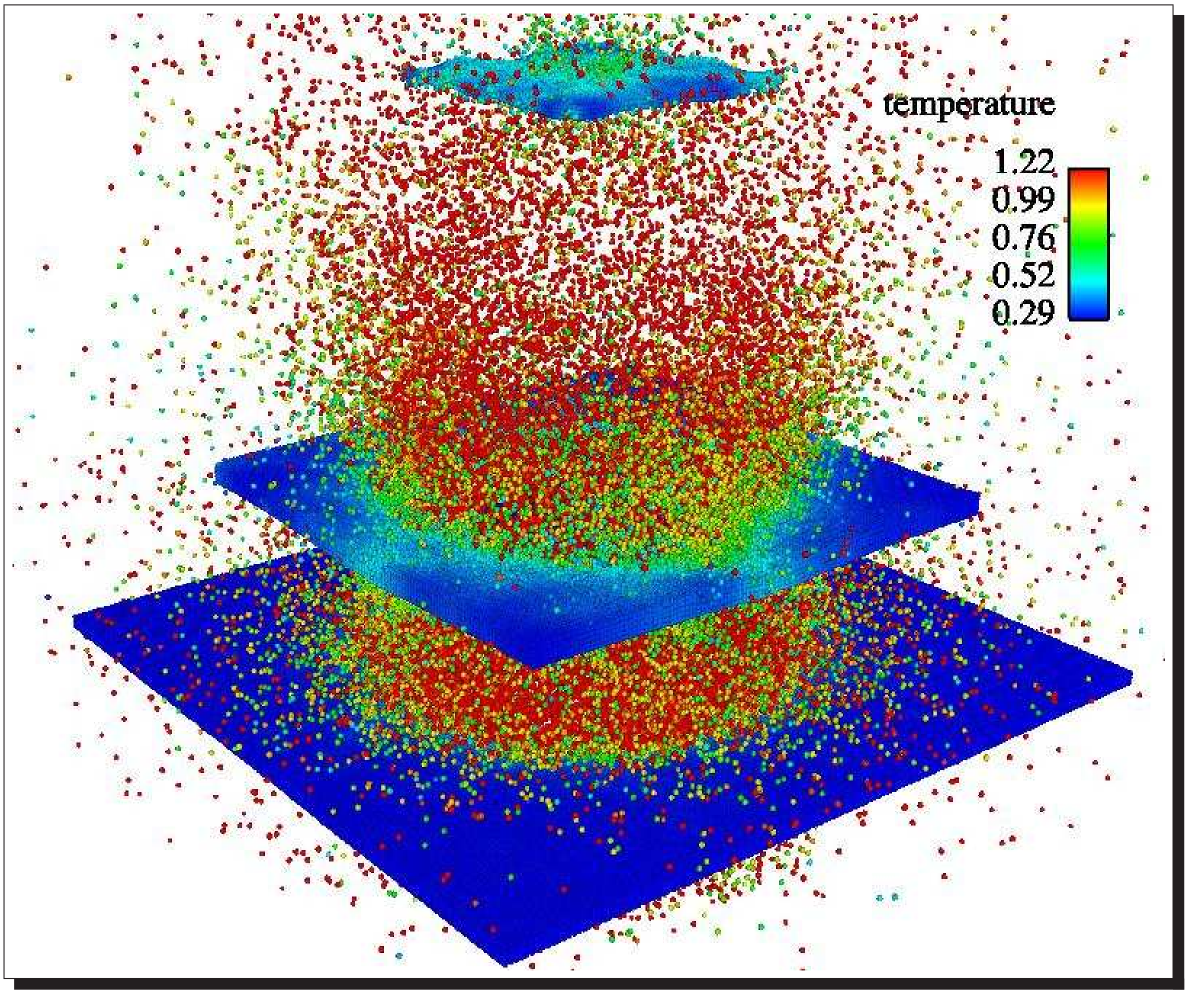

Figure 4.8: Aluminum dual plate shield: 8.636 cm stand off distance,particle plot at 30.7 μsec with color on temperature

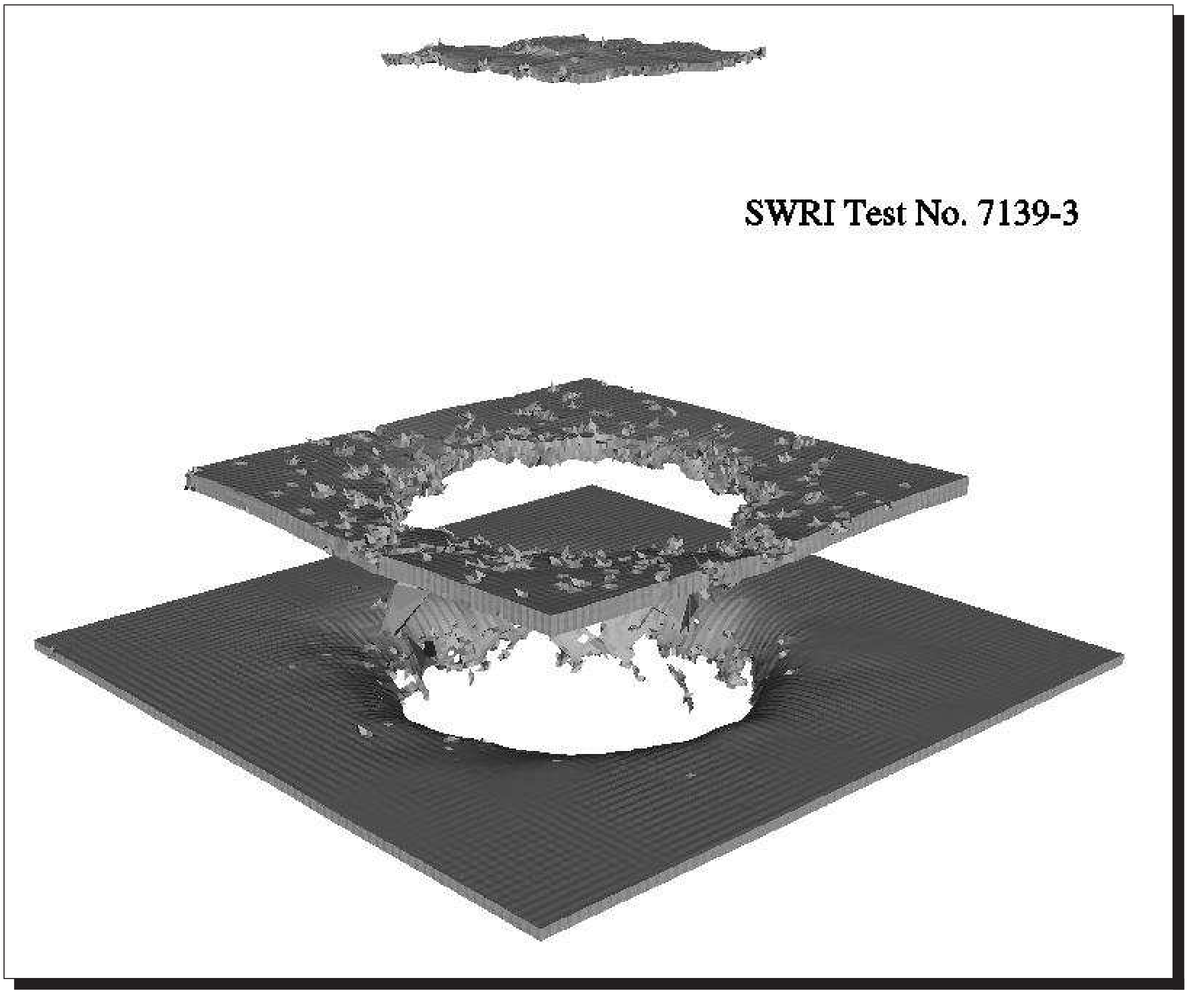

Figure 4.9: Aluminum dual plate shield: 8.636 cm maximum stand off distance, element plot at 30.7 μsec

4.2.5 Multi-layer Aluminum-Nextel-Kevlar shield

The fourth simulation involved a 45 degree oblique impact on a multi-layer aluminum-Nextel-Kevlar shield at a standoff distance of 7.62 cm. The simulation parameters are shown in table (4.5).

Parameters	
SWRI Test Number	7139-24
Shield type	Al-composite
First aluminum plate thickness (cm)	0.127
Second aluminum plate thickness (cm)	0.0
Nextel areal density (g/cm^2)	0.4
Kevlar areal density (g/cm^2)	0.128
Wall plate thickness (aluminum, cm)	0.3175
Maximum standoff (cm)	7.62
Impact velocity (km/sec)	11.25
Impact obliquity (velocity vector, deg)	45
Projectile mass (aluminum, g)	1.07
Projectile length-to-diameter ratio	1.1
Projectile pitch (wrt velocity vector, deg)	0
Projectile yaw (wrt velocity vector, deg)	0
Number of particles	415,413
Simulation time (μsec)	46.2
Wall clock time (hours)	109.3
Average number of processors	7.3
System	Onyx

Table 4.5: Parameters for the example simulations

Figures (4.10) and (4.11) show particle plots at impact and at 46.2 microseconds after impact, while Figure (4.12) shows an element plot of intact material at the simulation stop time. Consistent with the experimental results, the simulation predicts bulging but not perforation of the wall plate. It should be noted that some relevant material properties of Nextel and Kevlar are not well known, and are currently under study [32]. Although the linear elastic response of many composite materials has been well characterized, information on thermomechanical equation of state properties and plasticity properties is limited. Although the latter information is normally of secondary interest in structural design calculations, it is certainly of major interest in hypervelocity impact applications.

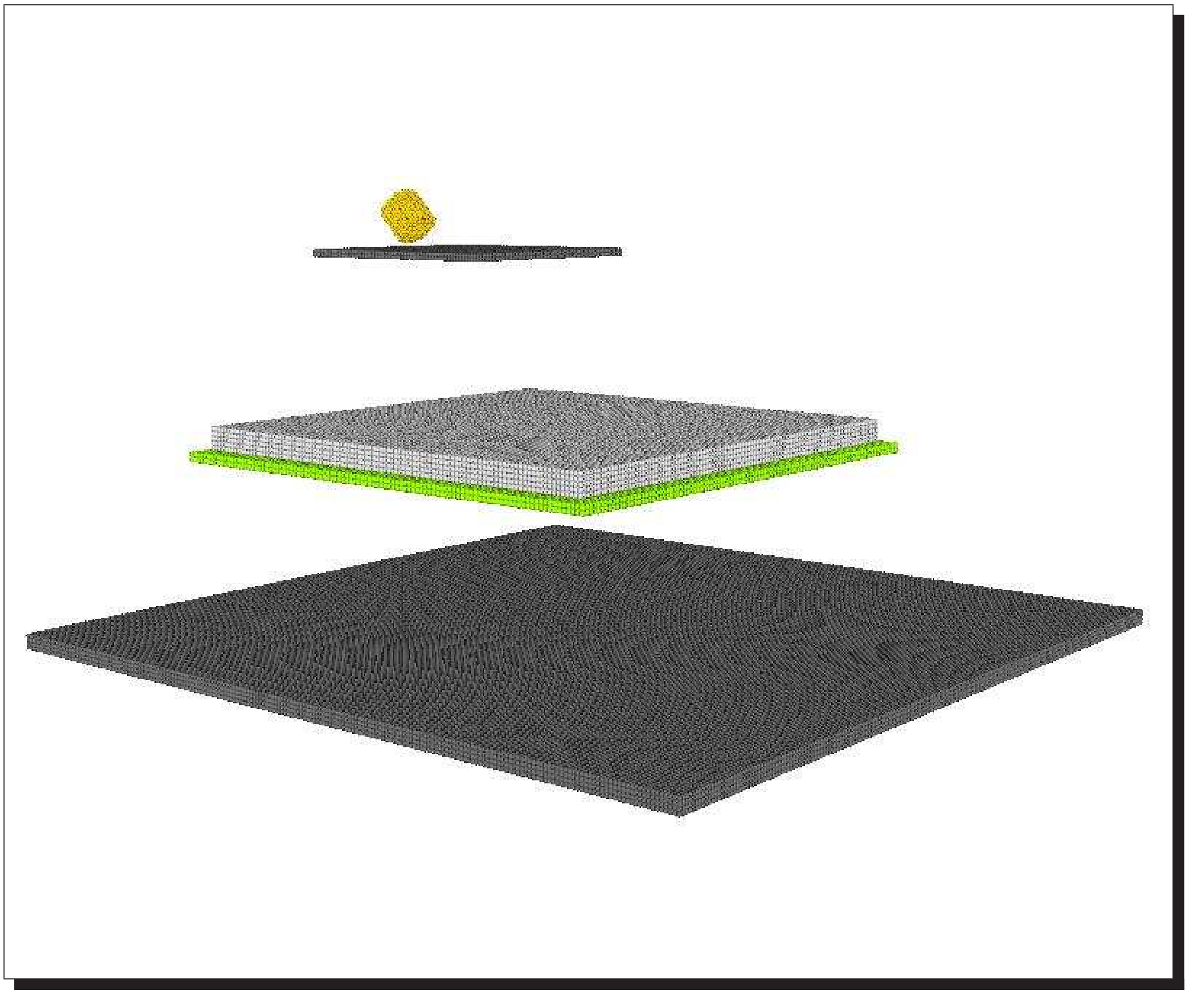

Figure 4.10: Aluminum Nextel Kevlar shield: 7.62 cm maximum stand off distance, initial configuration, particle plot

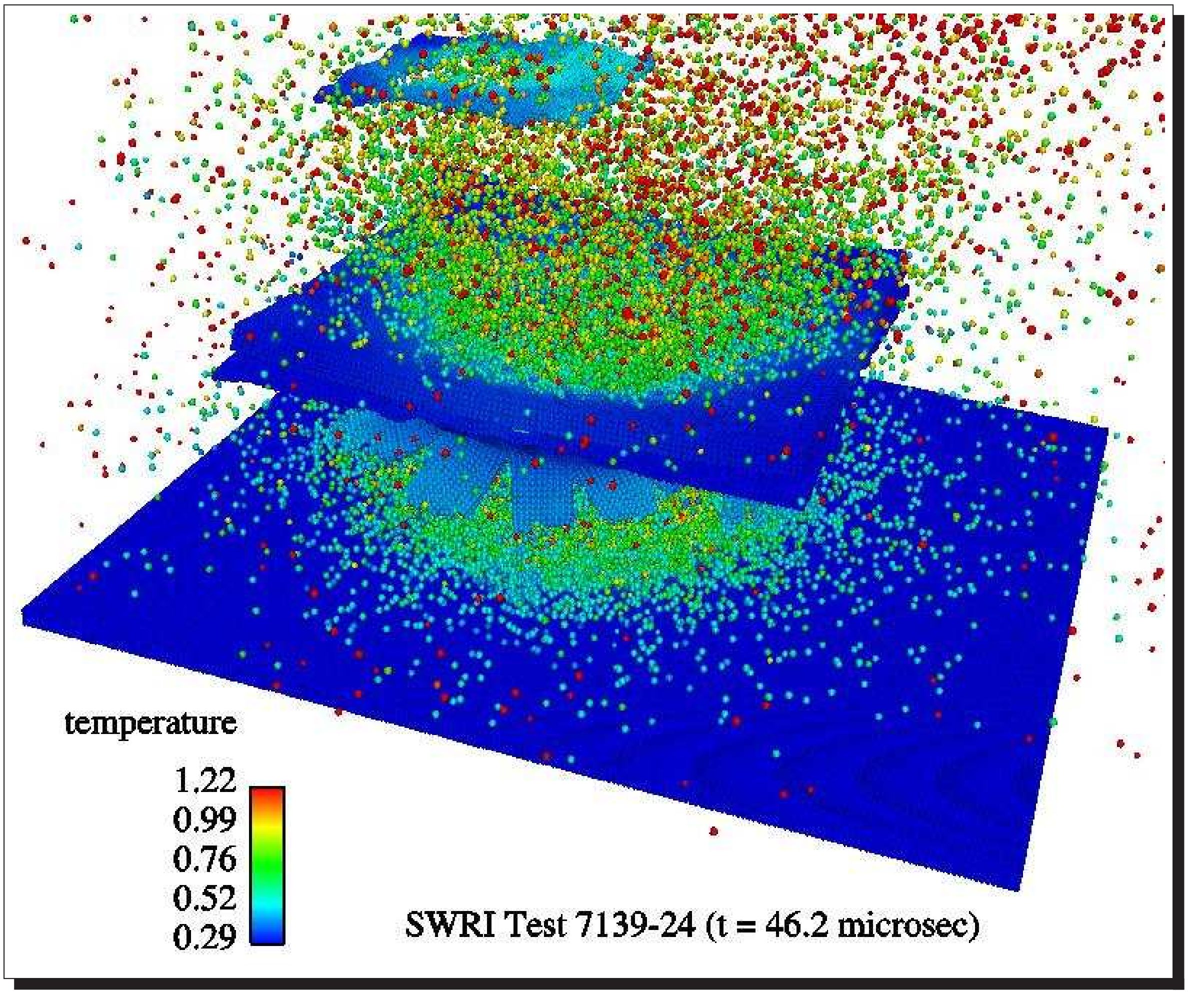

Figure 4.11: Aluminum Nextel Kevlar shield: 7.62 cm maximum stand off distance, particle plot at 46.2 μsec with color on temperature

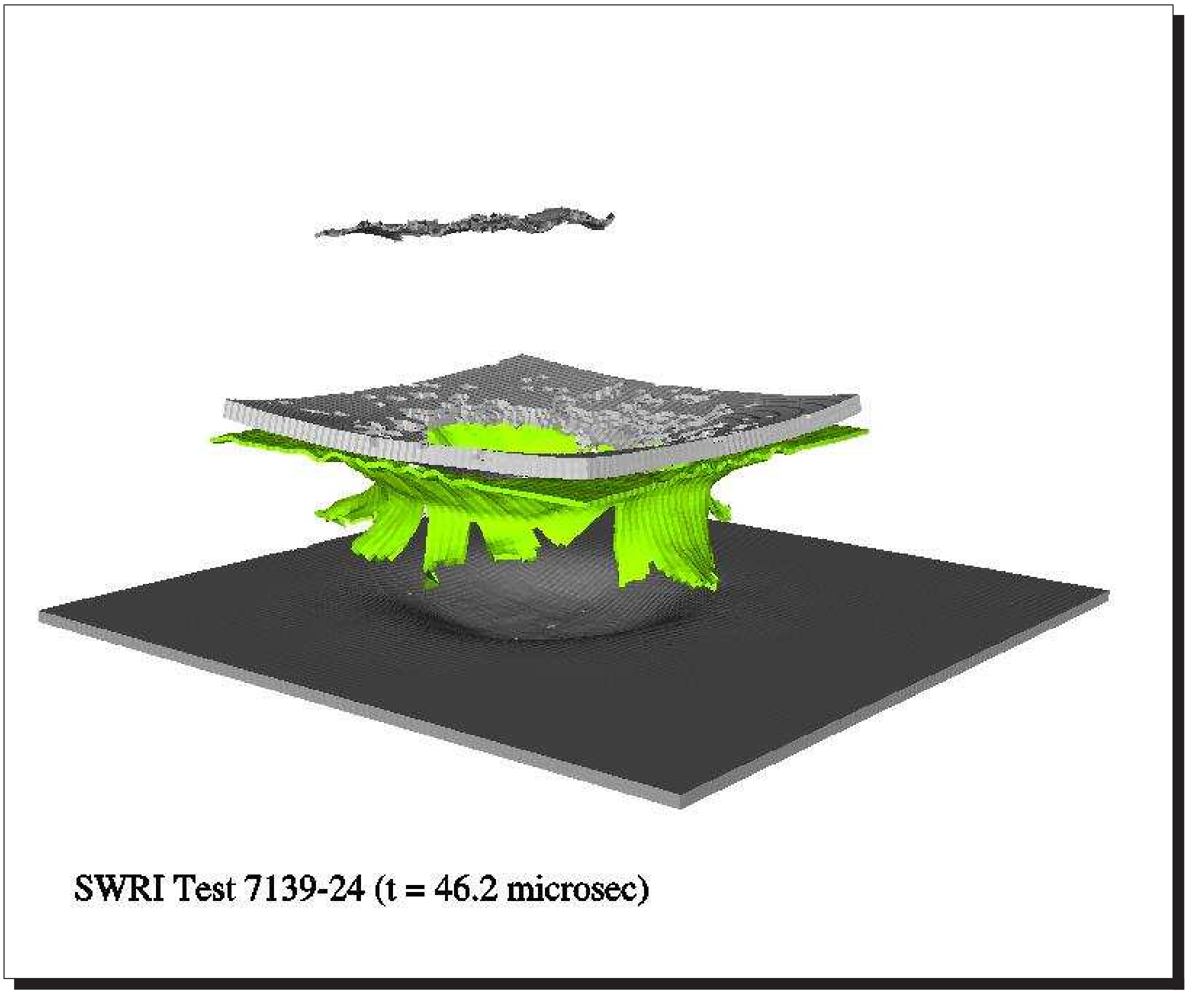

Figure 4.12: Aluminum Nextel Kevlar shield: 7.62 cm maximum stand off distance, element plot at 46.2 μsec

The results just described show in general good agreement of the simulations with the experimental data. They do suggest a need for higher resolution models, longer physical simulation times, and better composite material models in future simulation work.

4.3 Projectile shape effect

As noted in the last section, the geometry of projectiles produced by ISC experiments differs markedly from the solid spherical shape normally used in LGG tests. Since light gas guns operate in a lower velocity regime, correlating the results of ISC launcher and LGG tests is complicated by an unknown projectile shape effect. In an attempt to investigate the significance of this projectile shape effect, the first three ISC simulations described in the last section were repeated, with mass equivalent spherical projectiles replacing the actual hollow cylindrical ISC projectiles. Figures (4.13), (4.15), and (4.17) show element plots of the wall plate damage predictions obtained from simulations using hollow cylindrical ISC projectiles and mass equivalent spherical projectiles, run in each case to the same simulation stop time.

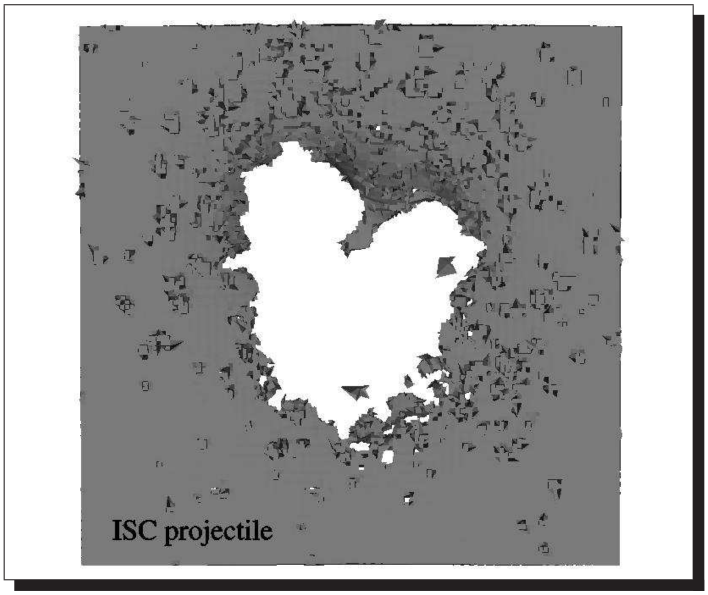

Figure 4.13: Wall damage for ISC projectile, Whipple shield 7.62cm stand off

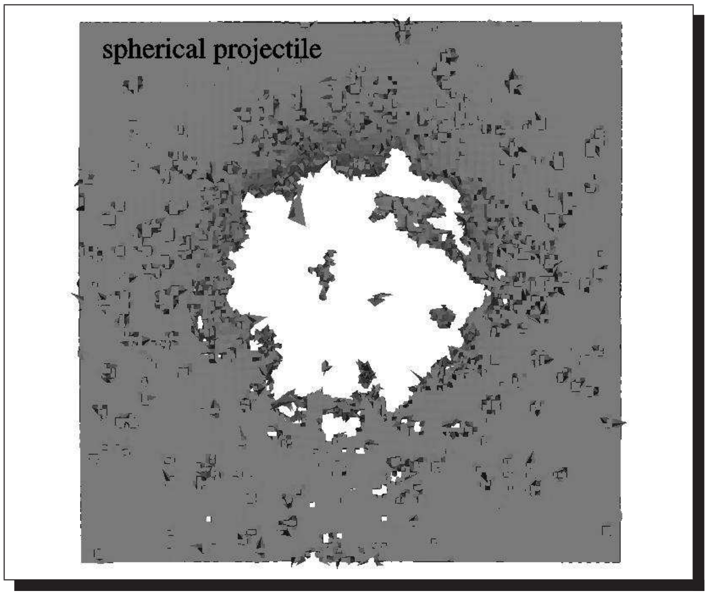

Figure 4.14: Wall damage for spherical projectile, Whipple shield 7.62cm stand off

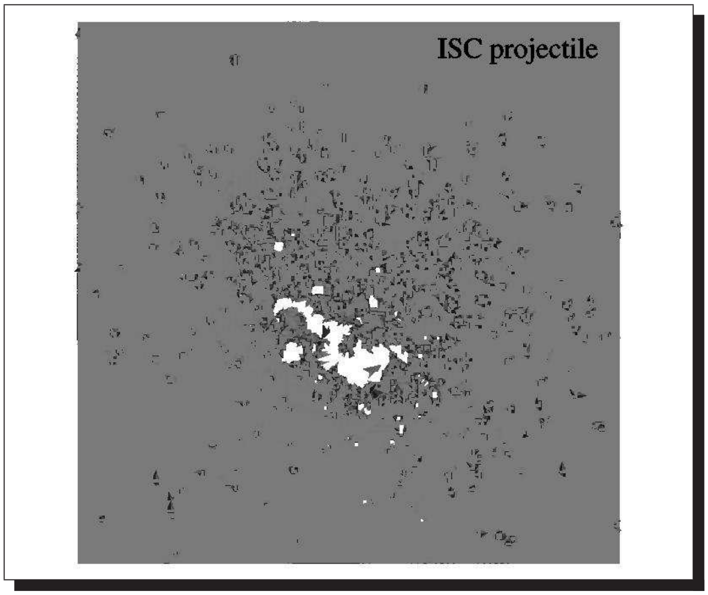

Figure 4.15: Wall damage for ISC projectile, Whipple shield 11.43cm stand off

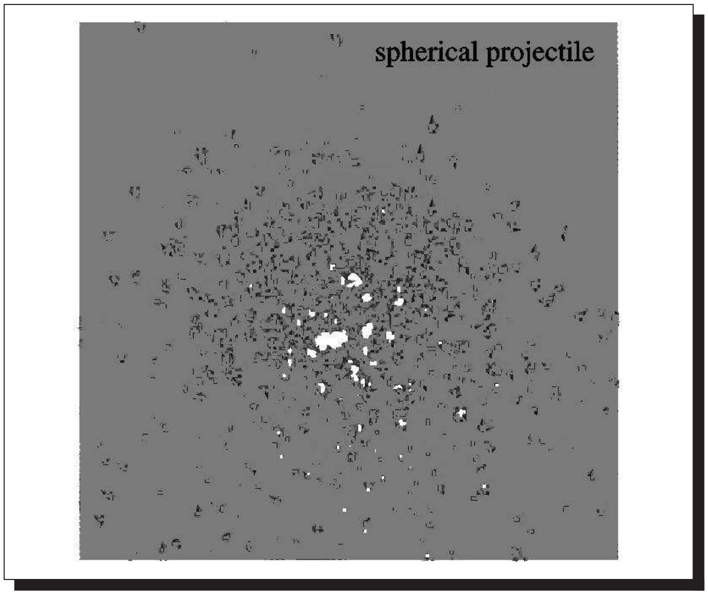

Figure 4.16: Wall damage for spherical projectile, Whipple shield 11.43cm stand off

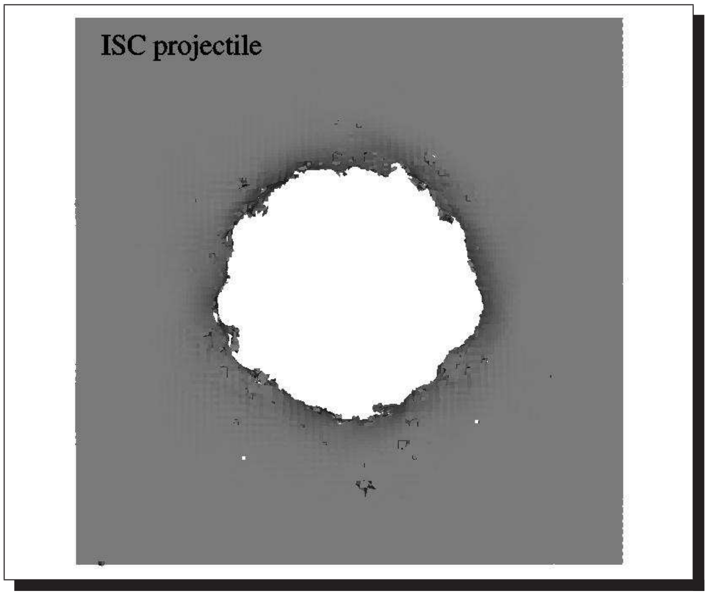

Figure 4.17: Wall damage for ISC projectile, dual plate aluminum shield 8.636cm stand off

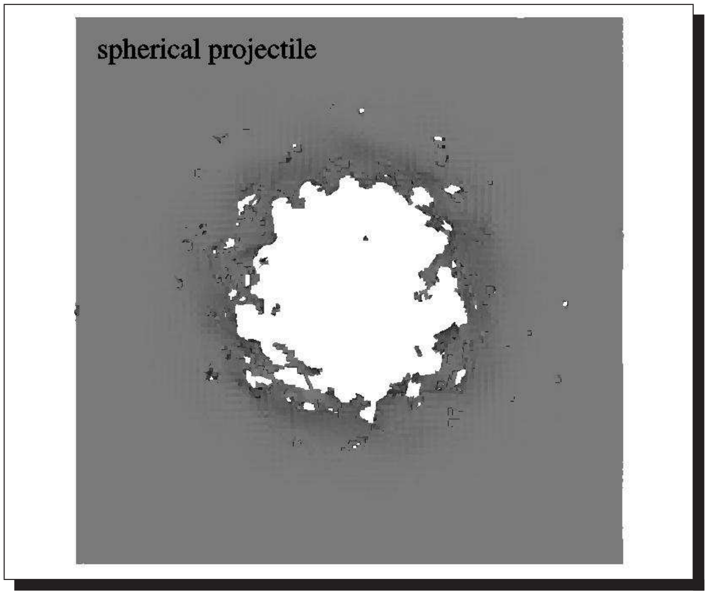

Figure 4.18: Wall damage for spherical projectile, dual plate aluminum shield 8.636cm stand off

The results suggest that ISC projectiles are more damaging than mass equivalent spheres, although the magnitude of the difference is difficult to quantify. In the first and third cases the projectile mass exceeds significantly the ballistic limit mass, and in all cases higher resolution models of the impact problems are needed in order to draw more definitive conclusions. However it should be noted that since the ISC projectiles:

(1) are hollow

(2) exhibit pitch and yaw with respect to their velocity vector, and

(3) involve rather low length-to-diameter ratios,

one might expect to observe a modest projectile shape effect. Considering the complex nature of these highly oblique hypervelocity impact problems, it appears that more experimental and computational work is needed to address the question of projectile shape effects.

4.4 Parallel speedup

Three dimensional impact simulations require large memory and CPU time allocations. Previous work on orbital debris shielding design [21] has reported wall clock times as high as eighteen days for single processor simulations of three dimensional problems. Such turnaround times effectively preclude the use computer simulation in many engineering design projects. Parallel processing offers an opportunity to greatly reduce turnaround time and make three dimensional simulation a more practical design tool.

The code used in the present work [16] was written for parallel execution on Onyx and Origin systems, using loop level compiler directives based on the

OpenMP standard. Alternative parallel implementations based on MPI constructs are in general more portable and presumably more efficient, although more difficult to implement. It should be emphasized that a high degree of parallelism must be present in the basic numerical algorithm in order to achieve good speedup under any coding scheme.

To evaluate parallel performance of the numerical algorithm and the code implementation used here, speedup tests were run on Origin systems with up to 128 processors. The test problems were large (300,000 - 500,000 particles), to insure that a meaningful load was maintained on each CPU as the processor allocation increased. Figure (4.19) shows the absolute speedup measured for a 500,000 particle test problem, based on the wall clock time required for ten time steps at various CPU allocations.

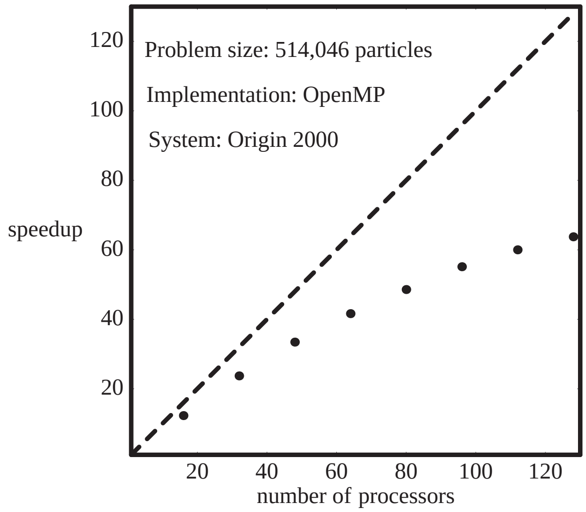

Figure 4.19: Absolute speedup for a 1GB size problem on Origin2000

The dotted line shows the maximum theoretical speedup, while the data points indicate the test results. At a CPU allocation of 64, the measured speedup is approximately two thirds of the theoretical maximum, indicating good parallel performance. At the maximum CPU allocation of 128, the efficiency drops to fifty percent. However the latter data point represents a factor of 64 reduction in wall clock time, indicating that a simulation which runs for over two months on one CPU can be run in one day on 128 processors.

Massively parallel systems are characterized by distributed memory architectures, complicating somewhat the practical interpretation of speedup test data. The Origin system discussed here is composed of a collection of compute *nodes*, each of which consists of two processors and 512 MB of RAM. An individual user is allocated a discrete number of nodes for each particular job, that is allocations consisting of arbitrary combinations of processors and RAM are not permitted. As a result, a particular job which requires 1 GB of RAM will be allocated a minimum of four processors, and the meaningful speedup curve for such a problem is one measured relative to a CPU allocation of four. Figure (4.20) shows the results of a relative speedup test run on an Origin system, for ten time steps of a 300,000 particle test problem, using the code discussed in the present work. The solid line represents the maximum theoretical relative speedup, while the data points show the test results. Again the data show good speedup for processor allocations as high as 64.

High performance parallel computer systems are not yet commonplace in engineering design work. However the preceding results demonstrate that the numerical method used here can effectively exploit such resources, an important consideration as low cost, high performance parallel hardware becomes more widely available.

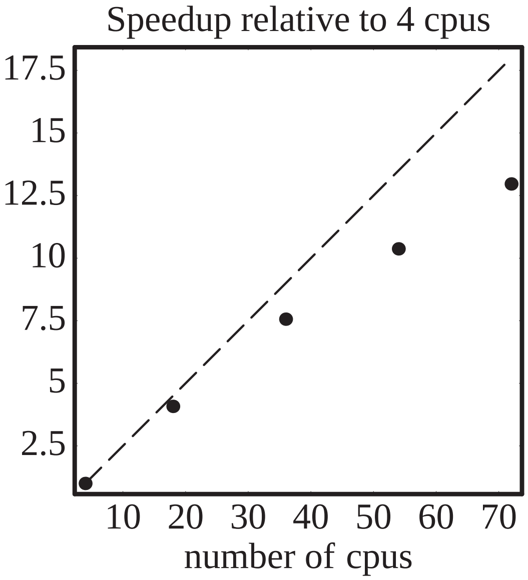

Figure 4.20: Relative speedup for a 1GB size problem on Origin2000

4.5 Conclusion

A systematic test of the use of parallel computation and a hybrid particle-element algorithm to simulate a range of three dimensional orbital debris impact experiments has been performed. The numerical method appears to offer certain advantages in addressing the three dimensional, multi-plate shield design problem. Additional work is needed to investigate model resolution, simulation time, projectile shape, and material property effects (including for example the use of the SESAME equation of state models). However developments to date suggest that massively parallel computation using some type of mixed particle-continuum scheme offers excellent opportunities for significant advances in simulation-based debris shield design.

Chapter 5

Summary and Future work

In this chapter a summary of the work done and a discussion of future work is presented. Note that conclusions were presented at the end of each chapter.

Most of existing particle methods use spherical particles, the use of which to model structures such as thin plates results in an exorbitant number of particles. The present work has developed a general hybrid particle finite element method to model hypervelocity impact. The model development uses thermo-mechanically interacting ellipsoidal particles, resulting in reduced computer resource requirements for hypervelocity impact simulations. Foreseeing the requirement to model the rotational dynamics of ellipsoidal particles, an efficient, singularity free rigid body rotational dynamics model was developed in chapter (2). Rotation was parameterized using four Euler parameters. The use of these parameters simplified the kinematic description, with a moderate increase in complexity of the dynamics. Previous work using Euler parameters for parameterizing rotation uses Lagrange multipliers, an additional momentum variable, or adds the constraint as an auxiliary differential equation. In contrast the model developed in here uses three angular momenta and four Euler parameters to describe the rotational dynamics. The model does not make use of any unknown Lagrange multiplier, to implement the Euler parameter constraint.

Although the use of both particles and finite elements results in increased computational cost, it provides the ability to model the disintegration of a solid into comminuted fluid, with ease. In addition, the use of particles simplifies problems involved in modeling contact-impact with pure finite elements. A classical weighted residual solution technique is rejected in favor of a system dynamics development. The benefits of such an approach are seen in the results of numerical simulations, presented in chapters (3) and (4). It is suggested that future work should introduce more complex material models, such as composites. Future shield design will increasingly rely on the use of such materials, due to their high strength to weight ratio.

Bibliography

[1] S.W. Attaway, M.W. Heinstein, J.W. Swegle. Coupling of smooth particle hydrodynamics with the finite element method. *Nuclear Engineering and Design*, 150:199–205, 1994.

[2] S.G. Bardenhagen, J.U. Brackbill, Deborah Sulsky. The material-point method for granular materials. *Computer methods in applied mechanics and engineering*, 187:529–541, 2000.

[3] Haim Baruh. *Analytical Dynamics.* WCB/McGraw Hill, 1999.

[4] Klaus-Jürgen Bathe. *Finite element Procedures.* Prentice Hall, Englewood Cliffs, New Jersey, 1996.

[5] Eric E. Becker, Graham F. Carey, J.Tinsley Oden. *Finite elements: An introduction.* Prentice Hall, Inc, Englewood Cliffs, New Jersey, 1983.

[6] T. Belytschko, Y. Krongauz, D. Organ, M.Fleming, P.Krysl. Meshless methods: An overview and recent developments. *Computer methods in applied mechanics and engineering*, 139:3–47, 1996.

[7] David J. Benson. Computational methods in Lagrangian and Eulerian hydrocodes. *Computer methods in Applied mechanics and Engineering*, 99:235–394, 1992.

[8] J.U. Brackbill, H.M. Ruppel. FLIP: a method for adaptivley zoned, particle in cell calcualtions of fluid flows in two dimensions. *Journal of Computational Physics*, 65:314–343, 1986.

[9] D. Burgess, D. Sulsky, J.U. Brackbill. Mass matrix formulation of the FLIP particle-in-cell method. *Journal of Computational Physics*, 103:1–15, 1992.

[10] C. O. Chang, C.S. Chou. Design of a viscous ring nutation damper for a freely precessing body. *Journal of Guidance, Control and Dynamics*, 14:1136–1144, 1991.

[11] Eric L. Christiansen. Design and performance equations for advanced meteoroid and debris shields. *International Journal of Impact Engineering*, 14:145–156, 1993.

[12] R.H. Cole. *Underwater Explosions.* Dover Publications, New York, 1948.

[13] Burton G. Cour-Palais. A multi-shock concept for spacecraft shielding. *International Journal of Impact Engineering*, 10:135–146, 1990.

[14] C.T. Dyka, R.P. Ingel. An approach for tension instability in smoothed particle hydrodynamics. *Computers and Structures*, 57:573–580, 1995.

[15] E. P. Fahrenthold, B.A. Horban. Thermodynamics of continuum damage and fragmentation models for hypervelocity impact. *International Journal of Impact Engineering*, 20:241–252, 1997.

[16] E.P. Fahrenthold. User's guide for EXOS. Technical report, University of Texas, Austin, 1999.

[17] E.P. Fahrenthold, J.C. Koo. Hamiltonian particle hydrodynamics. *Computer methods in Applied Mechanics and Engineering*, 146:43–52, 1997.

[18] E.P. Fahrenthold, J.C. Koo. Hybrid particle-element bond graphs for impact dynamics simulation. *Journal of Dynamic Systems, Measurement, and Control*, 122:306–313, 2000.

[19] Eric Fahrenthold, Blaise Horban. An improved particle-element method for hypervelocity impact simulation. *International Journal of Impact Engineering*, 26:169–178, 2001.

[20] Eric P. Fahrenthold, Blaise A. Horban. A hybrid particle-finite element method for hypervelocity impact simulation. *International Journal of Impact Engineering*, 23:237–248, 1999.

[21] Moreno Faraud, Roberto Destefanis, David Palmieri, Mario Marchetti. SPH simulations of debris impacts using two different computer codes. *International Journal of Impact Engineering*, 23:249–260, 1999.

[22] Michael S. Fulbright, Willy Benz, Melvyn B. Davies. A method of smoothed particle hydrodynamics using spheroidal kernels. *The Astrophysical Journal*, 440:254–262, 1995.

[23] J.H Ginsberg. *Advanced Engineering Dynamics.* Harper & Row, 1988.

[24] Herbert Goldstein. *Classical Mechanics.* Addison-Wesley Publishing Company, Inc, 1965.

[25] Donald T. Greenwood. *Principles of Dynamics.* Prentice Hall, Inc., Englewood Cliffs, New Jersey 07632, 1988.

[26] D.J. Grosch. Inhibited shaped charge launcher testing of spacecraft shield designs. Technical report, Southwest Research Institute, San Antonio, TX, April 1997.

[27] D.J. Grosch. Inhibited shaped charge launcher testing of spacecraft shield designs. Technical report, Southwest Research Institute, San Antonio, TX, November 1996.

[28] Francis H. Harlow. The particle-in-cell method for fluid dynamics. *Methods in Computational Physics*, 3:319–343, 1964.

[29] C.J. Hayhurst, I.H. Livingstone, R.A. Clegg, G.E. Fairlie, S.H. Hiermaier,M. Lambert. Numerical simulation of hypervelocity impacts on aluminum and Nextel/Kevlar whipple shields. In *Proceedings of the Hypervelocity Shielding Workshop*, pages 61–72, Galvestion, TX, USA, 1998.

[30] E.S. Hertel. Sandia report sand92-1879. Technical report, Sandia National Labs, Sep 1992.

[31] D.L. Hicks, L.M. Liebrock. SPH hydrocodes can be stablized with shape-lifting. *Computers and Mathematics with Applications*, 38:1–16, 1999.

[32] S. Hiermaier, W. Riedel, C.J. Hayhurst, R.A. Clegg, C.M. Wentzel. Advanced material models for hypervelocity impact simulations. Technical report, EMI-Report Number E 43/99, Freiburg, Germany, 1999.

[33] R.W. Hockney, J.W. Eastwood. *Computer Simulation using particles.* McGraw Hill Inc.,, New York, 1981.

[34] T.J.R. Hughes. *The Finite Element method–Linear Static and Dynamic Finite Element Analysis.* Dover Publishers, New York, 2000.

[35] Gordon Johnson. Linking of Lagrangian particle methods to standard finite element methods for high velocity computations. *Nuclear Engineering and Design*, 150:265–274, 1994.

[36] Gordon R. Johnson. Artificial viscosity effects for SPH impact computations. *International Journal of Impact Engineering*, 18:477–488, 1996.

[37] Gordon R. Johnson, Stephen R. Beissel. Normalized smoothing functions for sph impact computations. *International Journal of Numerical methods in Engineering*, 39:2725–2741, 1996.

[38] Nicholas L. Johnson, Darren S. Mcknight. *Artificial Space debris.* Krieger Publishing Company, Malabar, Florida, 1991.

[39] Charles E. Anderson Jr. An overview of the theory of hydrocodes. In *Hypervelocity Impact, Proceedings of the 1986 Symposium*, 1986.

[40] Harold S. Morton Jr. Hamiltonian and Lagrangian formulations of rigid body rotational dynamics based on euler parameters. *The Journal of Astronautical Sciences*, 41(4):561–591, 1993.

[41] S.L. Lee. *Reference book for composites technology.* Technomic Publishing, Lancaster, Pennsylvania, 1989.

[42] J. Lemaitre. Local approach of fracture. *Engineering Fracture mechanics*, 25:523–537, 1986.

[43] L.D. Libersky, P.W. Randles, T.C. Carney, D.L. Dickinson. Recent improvements in SPH modelling of hypervelocity impact. *International Journal of Impact Engineering*, 20:525–532, 1997.

[44] Wing Kam Liu, Su Hao, Ted Belytschko, Shofan Li, Chin Tang Chang. Multiscale methods. *International Journal of Numerical methods in Engineering*, 47:1343–1361, 2000.

[45] W.K. Liu, Y.Chen, S. Jun, J.S. Chen, T. Belytschko, C. Pan, R.A. Uras, C.T. Chang. Overview and applications of the Reproducing kernel particle methods. *Archives of Computational Methods in Engineering: State of the art reviews*, 3:3–80, 1996.

[46] Leonard Meirovitch. *Elements of Vibration Analysis.* McGraw-Hill Book Company, 1986.

[47] J.J. Monoghan. Particle methods for hydrodynamics. *Computer Physics Reports*, 3:71–124, 1985.

[48] J.J. Monoghan. On the problem of penetration in particle methods. *Journal of Computational Physics*, 82:1–15, 1989.

[49] J.J. Monoghan. SPH without tensile instability. *Journal of Computational Physics*, 159:290–311, 2000.

[50] P.E. Nikravesh, I.S. Chung. Application of Euler parametes to the dynamic analysis of three dimensional constrained mechanical systems. *Journal of Mechanical Design*, 104:785–791, October 1982.

[51] P.E. Nikravesh, O.K. Kwon, R.A. Wehage. Euler parameters in computational kinematics and dynamics. part 2. *Journal of Mechanisms, Transmissions and Automation Design*, 107:366–369, September 1985.

[52] P.E. Nikravesh, R.A. Wehage, O.K. Kwon. Euler parameters in computational kinematics and dynamics. part 1. *Journal of Mechanisms, Transmissions and Automation Design*, 107:358–365, September 1985.

[53] Praviz E. Nikravesh. *Computer aided analysis of Mechanical Systems.* Prentice Hall, 1988.

[54] Martin Nitschke, Ernst Heinrich Knickmeyer. Rotation parameters- a survey of techniques. *Journal of Surveying Engineering*, 126(3):83–105, August 2000.

[55] W.F. Noh. Errors for calculations of strong shocks using an artificial viscosity and an artificial heat flux. *Journal of Computational Physics*, 72:78–120, 1978.

[56] Committee on Space debris, Aeronautics and Space Engineering board, Comission of Engineering, Technical systems, National Research Council. *Orbital debris, A technical assessment.* National Academy Press, Washington, D.C., 1995.

[57] J. Michael Owen, Jens V. Villumsen, Paul R. Shapiro, Hugo Martel. Adaptive smoothed particle hydrodynamics: methodology II. *The Astrophysical Journal Supplement Series*, 116:155–209, June 1998.

[58] Anatoly N. Parshikov, Stanislav A. Medin, Igor I. Laukashenko, Valery A. Milekhin. Improvements of SPH method by means of interparticle contact algorithm and analysis of perforation tests at moderate projectile velocities. *International Journal of Impact Engineering*, 24:779–796, 2000.

[59] Piekutowski, A.J. Formation and description of debris clouds produced by hypervelocity impact. *NASA contractor report 4707*, 1996

[60] P.W. Randles, L.D. Libersky. Smoothed particle hydrodynamics: Some recent improvements and applications. *Computer methods in Applied mechanics and Engineering*, 139:375–408, 1996.

[61] P.W. Randles, L.D. Libersky. Normalized SPH with stress points. *International Journal of Impact Engineering*, 48:1445–1462, 2000.

[62] D. C. Rapaport. Molecular dynamics simulation using quaternions. *Journal of Computational Physics*, 60:306–314, 1985.

[63] Dietrich Rex. Will space run out of space? the orbital debris problem and its mitigation. *Space Policy*, 14:95–105, 1998.

[64] Paul R. Shapiro, Hugo Martel, Jens V. Villumsen,J. Michael Owen. Adaptive smoothed particle hydrodynamics with application to cosmology: methodology I. *The Astrophysical Journal Supplement Series*, 103:269–330, April 1996.

[65] M.D Shuster. A survey of attitude representations. *Journal of Astronautical Sciences*, 41:531–543, 1993.

[66] J.C. Simo, K.K. Wong. Unconditionally stable algorithms for rigid body dynamics that exactly preserve energy and momentum. *International Journal of Numerical methods in Engineering*, 31:19–52, 1991.

[67] Kerry W. Spring. Euler parameters and the use of quaternion algebra in the manipulation of finite rotations: A review. *Mechanism and Machine Theory*, 21(5):365–373, 1991.

[68] D.J. Steinberg. Equation of state and strength properties of selected materials. Technical report, Lawrence Livermore National Laboratory,UCRL-MA-106439, 1996.

[69] William Tyrrell Thompson. *Introduction to Space Dynamics*. John Wiley & Sons, Inc, 1961.

[70] Srinivas R. Vadali. On the Euler parameter constraint. *The Journal of Astronautical Sciences*, 36(3):259–265, 1988.

[71] R. Vignjevic, J. Campbell. A penalty approach for contact in smooth particle hydrodynamics. *ijie*, 23:945–956, 1999.

[72] R. Vignjevic, J. Campbell, L.Libersky. A treatment of zero energy modes in smooth particle hydrodynamics. *Computer methods in Applied mechanics and Engineering*, 184:67–85, 2000.

[73] F.L. Whipple. Meteorites and space travel. *The Astronomical Journal*, 52:131, 1947.

[74] Mark L. Wilkins. *Computer Simulation of Dynamics Phenomena.* Springer, 1999.

[75] Jerome D. Yatteau, Gunnar W. Recht, Karl T. Edquist. Transverse loading and response of long road penetrators during high velocity plate perforation. *International Journal of Impact Engineering*, 23:967–980, 1999.

[76] Jonas A. Zukas. *High velocity impact dynamics*, chapter 9, pages 593–709. John Wiley and Sons, Inc., 1990.

Vita

Ravishankar Ajjanagadde Shivarama is the eldest son of Sarojini and A.V. Shivarama was born on June 22, 1972. He grew up in the city of Bangalore, the capital of the southern state Karnataka, India. After completing his schooling at Vijaya High school and St. Joseph's college, Bangalore, he entered Bangalore University from where he graduated with a Bachelor of Engineering in Mechanical Engineering in 1994. In the same year he joined the Mechanical Engineering Department at the Indian Institute of Science (IISc), Bangalore. At IISc, he was a research scholar and worked in the area of robot dynamics and control. In 1997 he received a Master of Science in Engineering degree for his research on "*Possible chaos in robot control equations* ". From January 1997 to July 1997, he worked as a software engineer at Altair Software India Limited. In the fall of 1997, he joined the doctoral program at the University of Texas at Austin to continue his studies in Mechanical Engineering. He received the Bruton fellowship (2000-2001) and Alfred and Nellie King fellowship (2001-2002) for his scholastic accomplishments. After completing his Ph.D studies, Ravishankar will join the servo-mechanics group at Seagate Technology Inc.

Permanent Address: #256, AECS Layout I stage, 4th main cross,
Geddalahalli, Bangalore-560094

This dissertation was typeset with LaTeX 2_ε[1] by the author.

---

[1] LaTeX 2_ε is an extension of LaTeX. LaTeX is a collection of macros for TeX. TeX is a trademark of the American Mathematical Society.